Spectral Properties of Semiconductor Nanocrystals and their Applications

By

Thomas J. Liptay

Submitted to the Department of Electrical Engineering and Computer Science
in partial fulfillment of the requirements for the degree of

Doctor of Philosophy in Electrical Engineering and Computer Science

at the

MASSACHUSETTS INSTITUTE OF TECHNOLOGY

JUNE 2007

Author_____
Department of Electrical Engineering and Computer Science
May 4, 2007

Certified by_____
Rajeev J. Ram
Associate Professor of Electrical Engineering
Thesis Supervisor

Accepted by_____
Arthur C. Smith
Chairman, Department Committee on Graduate Students

Spectral Properties of Semiconductor Nanocrystals and their Applications

by

Thomas J. Liptay

Submitted to the Department of Electrical Engineering and Computer Science

on May 4, 2007, in partial fulfillment of the

requirements for the degree of

Doctor of Philosophy in Electrical Engineering and Computer Science

Abstract

The ability to engineer the optical properties of the semiconductor nanocrystals by controlling their growth – size, shape, materials, coatings, etc – makes them appealing for many optical applications. Despite the impressive development of nanocrystal manufacturing capabilities, there are still many basic questions about how to model nanocrystals that have yet to be adequately answered. This thesis investigates three important optical properties: 1) the temperature dependence of the bandedge absorption energy $E_{abs}(T)$, 2) the temperature dependence of the Stokes shift, and 3) the homogeneous linewidth. We relate these properties to various nanocrystal applications with particular focus on nanocrystal based microbead barcodes.

We present measurements of the temperature dependence of the absorption and emission spectra from 5 sizes of CdSe/ZnS nanocrystal ensembles. Our measurements show that $dE_{abs}(T)/dT$ is similar to the value for bulk CdSe for all sizes of nanocrystals, in contrast with previous experiments. We develop a model that can explain measured values of $dE_{abs}(T)/dT$ in both epitaxial quantum dots and colloidal nanocrystals of different materials. We interpret our measurements of the temperature dependence of the Stokes shift and linewidth, along with single nanocrystal fluorescence, from the perspective of two models based on different physical processes: 1) the fine structure of the bandedge exciton and 2) exciton-acoustic phonon scattering. We find that neither theory is able to adequately explain our measurements in isolation. We conclude that a comprehensive model that includes both physical mechanisms is required to explain our experimental results.

We present a detailed analysis of nanocrystal based microbead barcodes for high throughput biological screening. We make design decisions for how such a system would operate, develop a Monte Carlo simulation of the expected noise, and investigate different coding architectures. We investigate this system from the perspective of information and coding theory. We develop a Monte Carlo code generation algorithm to evaluate the information capacity of this system.

Thesis Supervisor: Rajeev J. Ram

Title: Associate Professor of Electrical Engineering

Acknowledgments

All research requires financial support, so I would first like to thank the Packard Foundation and the NSF Center for Materials Science and Engineering for providing the funding that made my research possible.

I would like to thank Rajeev Ram who served as my thesis advisor for the last six years. Rajeev gave me both the freedom and the resources to pursue my research the way that I wanted to. He stuck with me through my successes and my failures, and was always there to support me when I needed help. Rajeev is an amazing teacher and I have benefited tremendously from my interactions with him. While I greatly appreciate the opportunity and guidance that Rajeev provided me, I most appreciate the care that he has shown about my personal well being, through his words and his actions.

I greatly appreciate the help that I received from various members of Prof. Moungi Bawendi's lab. Brent Fisher and Sonia Rao both devoted significant time and energy to incorporating nanocrystals into a polymer matrix, an essential step for many of the results in this thesis. Lisa Marshal performed single nanocrystal measurements which provided crucial data for our interpretation of nanocrystal physics. As members of my thesis committee, Prof. Bawendi and Prof. Ippen provided valuable feedback on the direction of my research. I thank Gautham Nair, Yaakov Tischler, Paolo Boccazzi, Jan Kupec, Venkat Chandar, and Prof. Wornell for taking the time to suggest improvements and new directions for my research.

I'd also like to thank all of my past and present labmates in the POE group not only for all of the help that I received with my research, but also for making my everyday life in the lab a fun experience. I enjoyed Xiaoyun Guo's friendly smile, Tauhid Zaman's gangsta lifestyle, Reja Amataya's clear presentations, Kevin Lee's enthusiasm, and Jason Orcutt's ever present good nature. In particular, I'd like to thank Harry Lee and Pete Mayer who are two of best buddies that a guy could ever ask for. Harry has shown me what it means to think deeply about science and

life, and has consistently been there to give me a hand when I need it. Pete's love of life and work hard/play hard personality are truly inspirational to me. Pete has also been incredibly generous with his time and energy since I met him many years ago, and I have benefited from our friendship in many ways.

I'd like to thank Mom, Dad, Steve, and Grandma for always loving me for who I am and instilling the values that make me who I am. And finally, Kathy, your love supports me in all areas of my life and makes me a happier person.

Table of Contents

Chapter 1

Introduction

Over the last decade scientists have developed the ability to grow semiconductor nanocrystals with unprecedented control over size, shape, composition, and surface chemistry. Figure 1-1 shows what a nanocrystal (NC) with a capping layer looks like schematically. A nanocrystal is typically composed of 100s to 1000s of atoms, has a diameter of 1-10 nm, and is considered to be a type of quantum dot. Since NCs are much larger than atoms, yet much smaller than bulk materials, their electronic, optical, and mechanical properties are somewhere between the two regimes. The ability to engineer the optical properties of the NCs by controlling their growth – size, shape, materials, coatings, etc – differentiates them from organic dyes, making NCs appealing for many optical applications.

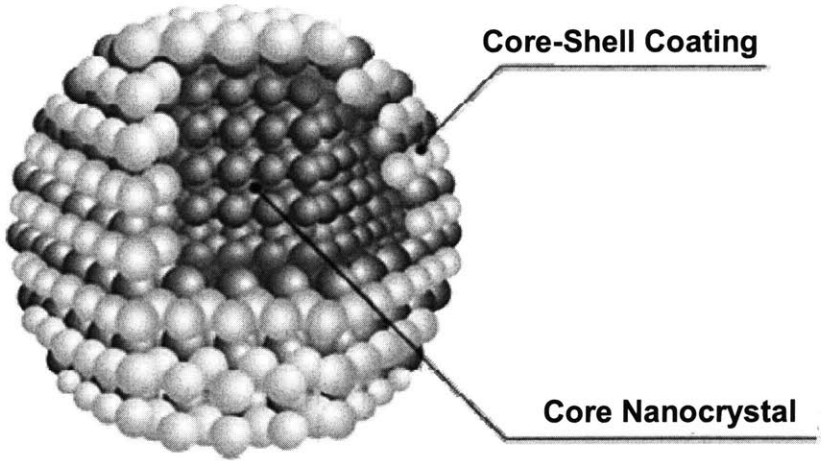

Figure 1-1: Schematic of a nanocrystal made of two types of semiconductor, a core material and a shell material. (from [1]) The colored spheres represent different types of atoms. Nanocrystals are also called colloidal quantum dots.

When a direct bandgap semiconductor bulk material is illuminated with UV light, electrons are excited from the valence band to the conduction band. The positively charged hole that remains in the valence band is attracted to the negatively charged electron in the conduction band via the Coulomb interaction. The electron and the hole bind together to form a quasi-

particle called an exciton which eventually recombines and emits a photon. In bulk CdSe, an exciton has a Bohr radius of R~5.6nm [2] and emits red light (λ~680nm). However, a NC often has a radius that is smaller than the bulk exciton radius, and this changes its optical properties through quantum confinement.

In a NC, the quantum mechanical wavefunctions of the electron and hole are compressed by the confining walls of the core. Because of this compression, extra energy (quantum confinement energy) is required to generate an exciton in a NC versus in bulk. This situation is analogous to the familiar quantum mechanical analysis of a particle in an infinite square well; As the radius of a NC decreases, the photon energy $E=2\pi\hbar c/\lambda$ required to create an exciton increases. CdSe NCs can be engineered to emit light across the entire visible spectrum. Figure 1-2 shows both the absorption and emission spectra for different sizes of CdSe NC ensembles.

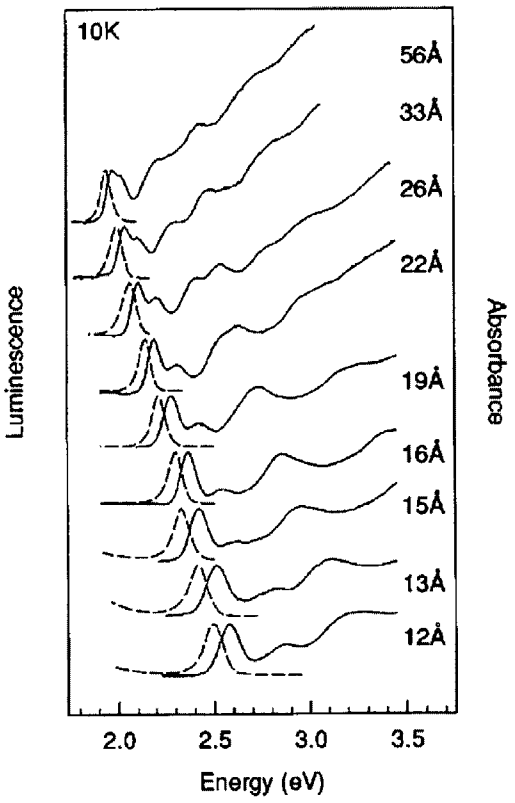

Figure 1-2: Absorption (solid) and emission (dashed) spectra for CdSe NCs with different radii at T=10K. (from [3]) The Stokes shift is the peak absorption minus the peak emission energy.

Despite the impressive development of NC manufacturing capabilities, there are still many basic questions about how to model NC optical properties that have yet to be adequately answered. This is because the physical mechanisms that determine NC optical properties are not

well understood. It is difficult to predict *a priori* the optical properties of a semiconductor NC made of a particular material and size. What is the temperature dependence of the exciton absorption energy? What causes the Stokes shift? What is homogeneous linewidth of a single NC? Developing a physical model to explain these NC properties will hopefully allow for a more intelligent NC design – in terms of core/shell material, NC size, NC shape, surrounding matrix, etc - for specific applications. Even for CdSe NCs, the most studied of all NC technologies, the answers to these questions have not been well established.

For example, in many current and potential NC applications - including biological imaging, optical barcodes, and laser gain media - the spectral linewidth of the NC ensemble emission is a critical parameter. Understanding what fraction of the ensemble linewidth at room temperature is due to inhomogeneous and homogeneous broadening is important. Inhomogeneous broadening refers to broadening due to differences in size, shape, impurities, and local environment, that cause different NCs to have different energy levels and hence broaden the linewidth of an ensemble of NCs. Homogeneous broadening refers to broadening that is caused by processes that are intrinsic to an individual NC like electron-phonon scattering or thermal fluctuations. Broadening due to inhomogeneities can be reduced by better manufacturing and control of the NC's environment, but the other types of homogeneous broadening are "fundamental" and can not easily be eliminated through superior engineering.

Chapters 2 and 3 focus on developing a physical model to explain NC optical properties based on our experiments with CdSe/ZnS NCs (CdSe core with a ZnS capping layer). We specifically focus on characterizing and analyzing three NC properties: 1) the temperature dependence of the bandedge absorption energy $E_{abs}(T)$, 2) the temperature dependence of the Stokes shift, and 3) the homogeneous linewidth of a single NC. These optical properties are important design parameters and place "fundamental" constraints on many potential NC applications. In chapter 4 we present a detailed analysis of one potential application, NC based microbead barcodes for high throughput biological screening.

Before continuing, we first motivate our research in section 1.1 by reviewing some current and potential NC applications and how they relate to the physical properties of NCs. Section 1.2 reviews the physics and the current state of understanding with respect to $E_{abs}(T)$, the Stokes shift, and the linewidth of NCs. Finally, section 1.3 reviews the need for biological screening, what technologies are currently available commercially, and how replacing traditional dyes with NCs in microbead barcodes might improve current technology.

1.1 Applications of Semiconductor Nanocrystals

This section discusses some of the applications of NCs for which $E_{abs}(T)$, the Stokes shift, and the spectral linewidth are critical parameters – lighting, display, temperature sensor applications, laser gain media, and biological imaging. Additional applications that have received attention in the literature, but are not discussed in this section include using the emission from a single NC as a source of single photons [4], combining NCs with organic materials to make solar cells [5], and using the spins of singly charged NCs as qubits for quantum information processing [6].

1.1.1 Display, Lighting, and Temperature Sensor Applications

Researchers have successfully demonstrated that NCs can be used as light emitters in organic devices [5], thus opening the door for displays based on NC emission. The benefit of a display that uses NCs as fluorophores is that a wider range of colors can be potentially be displayed than is possible using traditional CRT displays. The CIE diagram in Figure 1-3 shows the range of colors that are visible to the human eye. The range of colors that can be covered by a CRT display is shown in the black triangle, while the dots show the range of colors that could be covered by using currently available NC ensembles as fluorophores. In a CIE diagram, pure colors are closer to the edge of the diagram and mixtures are near the center. The homogeneous linewidth of NCs puts a "fundamental" limit on how much the ensemble linewidth can be narrowed by minimizing inhomogeneous broadening, and therefore places a "fundamental" constraint on the range of colors that can potentially be displayed with improved engineering.

A related application is to simply use hybrid NC/organics as a single color illuminant rather than a display. The range of colors produced by traditional semiconductor LEDs is limited by the ability to produce materials that emit at desired wavelengths. Hybrid NC/organic devices on the other hand can emit across the visible spectrum. In particular, using NCs as a yellow illuminant in traffic signals might be an ideal application. For this application, an important specification is the amount that the wavelength changes with temperature. Since the range of colors that humans perceive as yellow is extremely narrow, even a small wavelength drift could cause a person to misinterpret a yellow light. UK rail specifications released in 1999 allows no more than a $\Delta\lambda$=2.5nm chromaticity drift from -20°C to +40°C [7], a difficult specification to satisfy with traditional LED technology. Developing a model for $dE_{emi}(T)/dT$ in NCs might allow the intelligent design of a NC technology that minimizes $dE_{emi}(T)/dT$ and satisfied these

specifications.

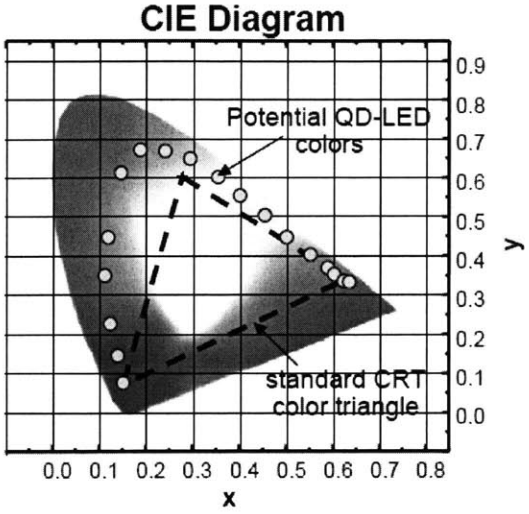

Figure 1-3: The CIE diagram shows the range of colors that are visible to the human eye. Black triangle – range of colors covered by CRT displays. Circles – range of colors covered by current NC ensembles. (from [8])

Finally, the emission wavelength of NCs could be used to measure temperature on the nanometer length scale. For instance, if a monolayer of NCs were deposited in an organic electronic device, then the temperature of the NC layer could be inferred by exciting the NCs with UV and measuring the spectrum. We believe that measuring temperature to within $\Delta T=2K$ is reasonable. This would allow a direct measurement of how heat is transported in an organic electronic device on a nanometer length scale, something that it is difficult to imagine using standard techniques. Unlike the previous application, here it is desirable to design NCs with a large $dE_{emi}(T)/dT$ in order to increase temperature sensitivity.

In our analysis of Chapters 2 and 3 we separately consider the temperature dependence of both the absorption $E_{abs}(T)$ and the Stokes shift $E_{abs}(T)$-$E_{emi}(T)$, which together imply $E_{emi}(T)$. In conclusion, all three of the optical properties that we will analyze - $E_{abs}(T)$, the Stokes shift, and linewidth – have important implications for NC based display, lighting, and temperature sensor applications.

1.1.2 Laser Gain Medium

Theoretically, using NCs as a laser gain medium, in place of a bulk semiconductor, will result in

more thermal stablility (higher T_0), a lower threshold current, and will allow for a wider range of wavelengths [9]. The first two advantages stem from the fact that confinement of electron and holes leads to a sharper density of states at the band edge compared to bulk. Quantum well lasers confine electrons and holes to a 2D slab in order to achieve these advantages, and are widely used today. NCs, which confine the carriers in all 3 dimensions, theoretically have an even greater advantage. NC lasers have been demonstrated experimentally [10-12], but to date they have yet to show many of the advantages that were hoped for.

Both the Stokes shift and the emission linewidth are important parameters for modeling the NC gain spectrum. Understanding the origin of the Stokes shift has important implications for how intense the pumping needs to be in order to achieve gain. As the Stokes shift decreases, the overlap of the absorption and emission spectra increases, and therefore the gain spectrum (which is the sum of the absorption spectrum and an appropriately weighted emission spectrum) decreases. On the other hand, the maximum gain is inversely proportional to the homogeneous linewidth [13]. Developing a model for both the Stokes shift and homogeneous linewidth may allow for a better design and a more realistic assessment of the potential of NC based lasers.

1.1.3 Biological Imaging

Perhaps the most common application of NCs currently is as a replacement for traditional dyes in biological imaging applications. NCs have many advantages over traditional dyes for imaging applications. 1) They don't bleach as quickly. So, the same piece of tissue can be imaged for longer periods of time. 2) They are brighter, so you can image on a shorter time scale. 3) NCs can be excited with one UV light source. With traditional dyes, each dye needs its own excitation source which makes imaging more difficult and expensive. 4) The emission spectra of traditional dyes tend to overlap with one another causing cross-talk between the different colors. NC emission linewidths are very symmetric, slightly narrower, and can be chosen so that cross-talk is minimal. Researchers have demonstrated the ability to label 4 types of tissue with different colors of NCs [14] which is difficult to achieve with traditional dyes. Figure 1-4 shows a multicolor image using NCs and a traditional dye.

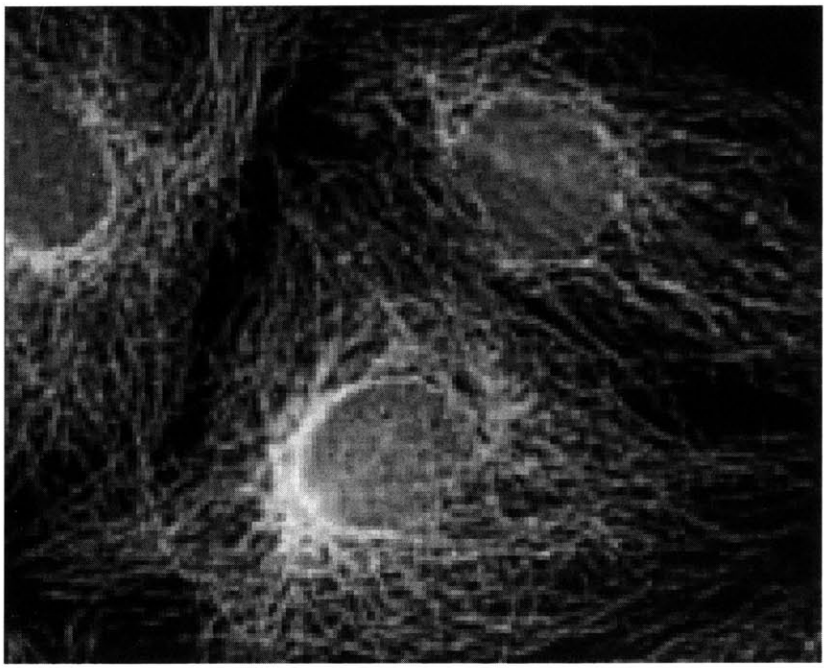

Figure 1-4: (from [14]) – Double-labeling of mitochondria and microtubules in NIH 3T3 cells. The mitocondria are in red and microtubules are in green. (Nuclei are counterstained with a traditional dye).

The emission linewidth of NCs is an important parameter to consider for biological imaging. As the linewidth is reduced, it is possible to image more types tissue without having significant cross-talk between different colors. Again, understanding the origin of the emission linewidth is important. If the linewidth is primarily due to size inhomogeneities, then it may be worth investing in methods to improve size selection and reduce the linewidth. If the linewidth is primarily due to the homogeneous linewidth, then improved size selection will have a minimal impact and effort should be directed elsewhere. Developing a better understanding of NC physics may help to focus research in more productive areas. The next section reviews the current literature models of NC physics.

1.2 Nanocrystal Physics

The applications discussed in the previous section indicate that the temperature dependence of the emission wavelength, the Stokes shift, and the spectral linewidth are all important design parameters. This section reviews the current state of the literature with respect to these three parameters, although we break the temperature dependence of the emission energy $E_{emi}(T)$ into

two parts – the temperature dependence of the bandedge absorption $E_{abs}(T)$ and the Stokes shift $E_{abs}(T) - E_{emi}(T)$.

1.2.1 Bandedge Absorption Energy $E_{abs}(T)$

In bulk semiconductors, it is well known that the temperature dependence of the bandgap is primarily a result of thermal expansion of the lattice and electron-phonon interactions, the later effect being the most important for most semiconductors [15]. Since confinement in a quantum dot (QD) changes the electronic energy levels and phonon modes, it has been argued that the electron-phonon interaction strength may change, and as a result the temperature dependence of the excitonic energy may change. References [16-22] all suggest that the $E_{abs}(T)$ in QDs should be or is modified from the bulk temperature dependence due to modified phonon coupling. This reasoning was used to explain the experimentally observed size dependence of dE/dT in CdS [21], CdSe [16], and PbS and PbSe NCs [17]. (See Figure 1-5) (Most papers do not differentiate between $E_{abs}(T)$ and $E_{emi}(T)$ and seem to implicitly assume that they are the same E(T).) Ref [18] makes the interesting observation that for epitaxial QDs (InAs, $In_{0.6}Ga_{0.4}As$, GaAs), the temperature dependence dE/dT is well described by the bulk value, in contrast to colloidal nanocrystals. (see Figure 1-6) This difference is unexpected because the physical mechanisms that are invoked to explain the size dependence of dE/dT in NCs should also be applicable to epitaxial QDs. Ref [18] concludes that "No detailed theory, either first principles or semiempirical, that would allow for an accurate description of E(T), seems to be available for QDs."

In Chapter 2, we present our own measurements of the temperature dependence of the bandedge absorption of different sized high quality CdSe/ZnS NCs. In contrast to the literature we find that the bulk temperature dependence accurately describes our measured dE_{abs}/dT for all sizes. Additionally, by considering how the temperature dependence of the effective mass affects the confinement energy we are able to adequately explain the strong size dependence of dE_{abs}/dT in PbS and PbSe NCs [23].

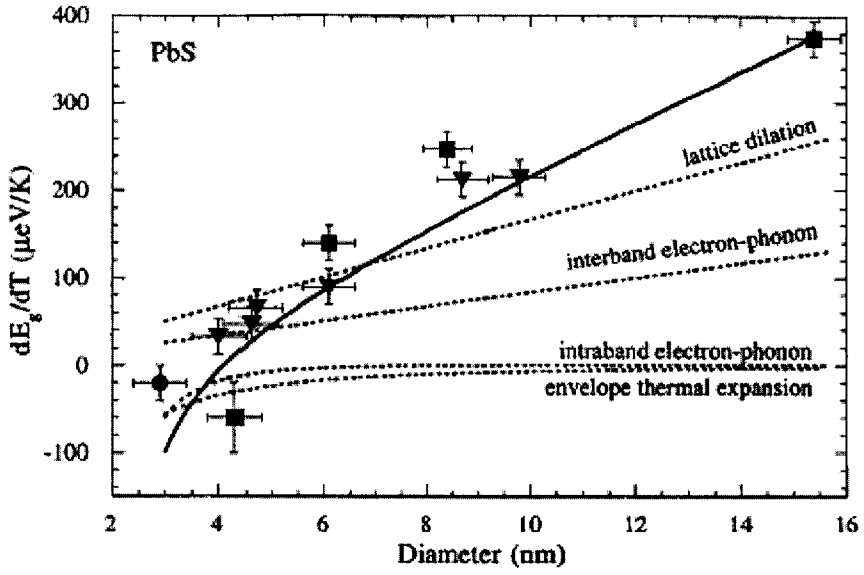

Figure 1-5: The temperature dependence of the bandedge absorption feature in PbS NCs experimentally has a strong size dependence. The proposed explanation involves electron-phonon scattering. (from [17])

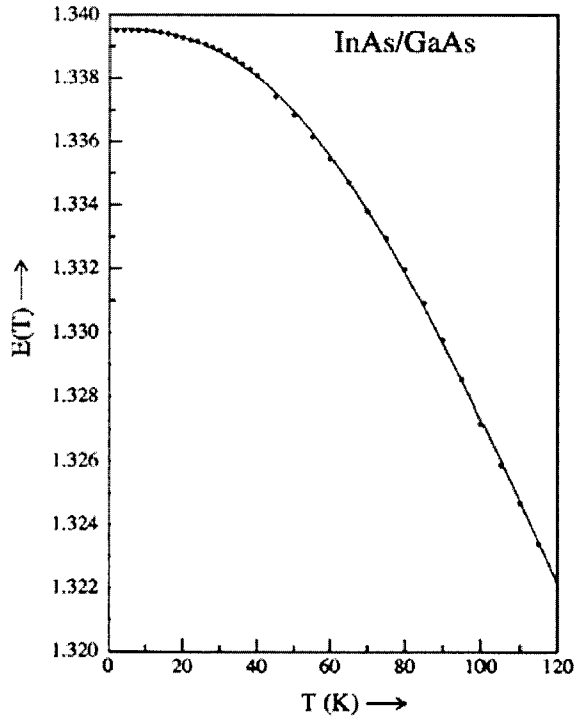

Figure 1-6: The temperature dependence of the emission in epitaxial InAs/GaAs quantum dots is primarily determined by the bulk temperature dependence. (from [18])

1.2.2 Stokes Shift

Existing theory attributes the large non-resonant Stokes shift in CdSe NCs primarily to the exciton fine structure [3]. The fine structure is a set of discrete energy levels that is derived by considering confinement effects within a multiband effective mass framework [3]. PLE (photoluminescence excitation) experiments show sharp features in the absorption spectrum of the bandedge exciton that compare reasonably well with fine structure theoretical predictions [24]. Figure 1-7 shows the inferred single NC bandedge absorption spectrum from PLE experiments [24]. Figure 1-8 shows how the theoretically derived fine structure compares to experiment [24].

The fine structure model predicts a strong temperature dependence for the Stokes shift of small CdSe NCs. In Chapter 3 we present our measurements of the temperature dependence of the Stokes shift for five sizes of CdSe/ZnS NCs. Surprisingly, we find that the Stokes shift has a weak temperature dependence for all sizes. We speculate that the temperature independent Stokes shift that is implicit in exciton-acoustic phonon scattering models may offer a partial explanation. This implication of exciton-acoustic phonon scattering has not been widely appreciated by the research community, which instead has focused on the homogeneous linewidth implied by exciton-acoustic phonon scattering.

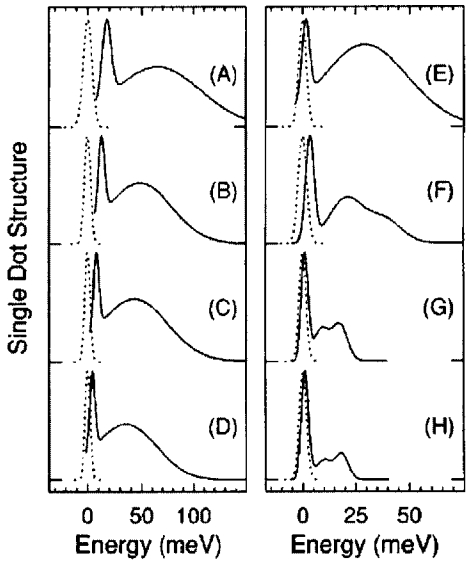

Figure 1-7: The inferred single NC bandedge absorption (excluding optical phonon replicas) from PLE experiments for different sizes of CdSe NCs. A-H correspond to NC radii of 15, 19, 21, 24, 27, 33, 44, and 50Å. (from [24])

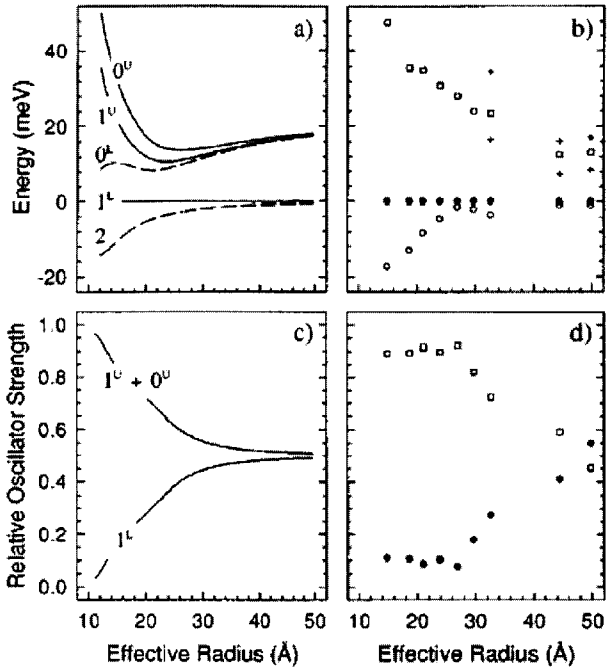

Figure 1-8: Theoretical fine structure for CdSe NCs (a and c) and experimentally inferred fine structure (b and d). (from [24])

1.2.3 Spectral Linewidth

For many of the applications discussed in section 1.1, it is desirable to make the NC ensemble emission linewidth as narrow as possible. However, the contributions of different broadening mechanisms to the ensemble spectrum at room temperature (the temperature regime for most applications) have not been well established. Figure 1-9 shows that single NC emission spectra are much narrower than ensemble linewidths at low temperature. This inhomogeneous broadening is primarily due to the size distribution of NCs within the ensemble, although spectral diffusion also contributes to the ensemble linewidth. Spectral diffusion refers to the experimental observation that the spectrum of a single NC changes with time. Spectral diffusion is believed to be the result of Stark shifts that are due to fluctuating local electric fields which result from charges moving in the environment surrounding the NC. A direct result of spectral diffusion is that the single NC spectrum broadens as the integration time of the spectrometer increases, as is shown in figure 1-10. Additionally, the rate of spectral diffusion increases with temperature, complicating the interpretation of single NC spectra at room temperature.

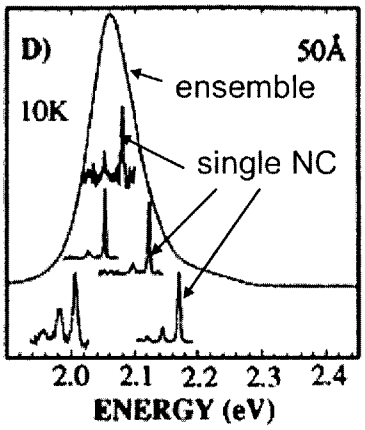

Figure 1-9: Single CdSe NC emission spectra along with the NC ensemble spectra. (from [25])

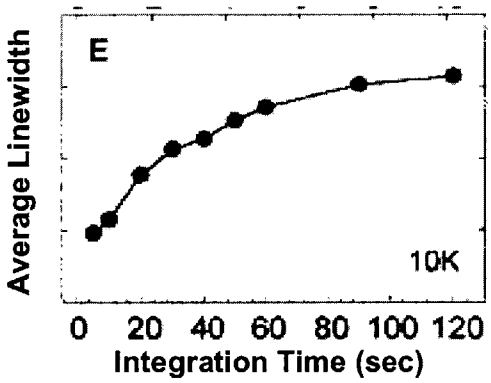

Figure 1-10: Single CdSe NC linewidth at T=10K as a function of spectrometer integration time. (from [26])

The homogeneous linewidth has been inferred from femtosecond photon echo experiments [27] on different sizes of CdSe NCs as a function of temperature in [28]. Exciton-acoustic phonon scattering has been invoked to explain both the inverse size and linear temperature dependence of the echo decay rate [27]. However, the broad linewidth (~10 meV) implied by photon echo experiments at low temperatures seems to be at odds with the narrow (~100μeV) linewidths that are measured for single NC emission [25]. This apparent conflict is not discussed in the literature. However, we speculate that it may be partially resolved by considering the results of spectral hole burning experiments which show a narrow line on top of a broad pedestal [29]. This spectrum, shown in figure 1-11, has been described as a "Prussian helmet" and has been attributed to exciton-acoustic phonon scattering. Within this interpretation, the broad pedestal corresponds to acoustic phonon assisted optical transitions, while the narrow peak corresponds to a purely optical transition, and is called the zero phonon line (ZPL) [30]. In

conclusion, there is no concensus in the literature regarding how to model the spectrum of a single NC, nor is it clear what the experimental homogeneous linewidth is at room temperature.

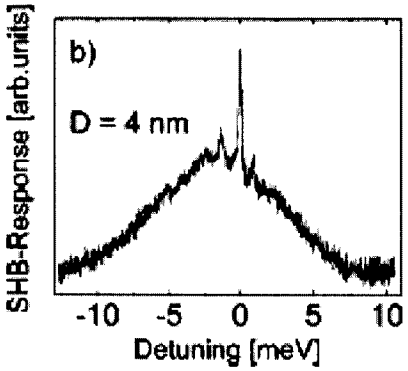

Figure 1-11: Measured spectral hole burning spectrum for R=2nm CdSe/ZnS NCs. (from [29])

In Chapter 3 we use the temperature dependence of ensemble emission spectrum to infer the room temperature homogeneous linewidth as a function of NC size. We compare our experimentally measured temperature and size dependence of the Stokes shift and ensemble linewidth to the predictions of an exciton-acoustic phonon scattering model and find adequate agreement. However, we also present a single NC emission spectrum for a small NC which is inconsistent with this model. We conclude that a more complete model that treats both the fine structure and exciton-acoustic phonon scattering in the same physical framework is required to explain our experimental data. Hopefully, this model will assist in NC design for applications such as NC based microbead barcodes for biological assays.

1.3 Review of Biological Assay Technology

A recurring desire in many areas of biological research is to screen for the presence of many predefined target biomolecules in large numbers of test samples in a rapid and economic manner. Currently, the two dominant biological assay technologies are DNA planar arrays and microbead based assays. Figure 1-12 shows schematically how microbead biological assays work. First, different types of microbeads are created by varying the ratio of different colors of dyes that are incorporated into the polymer microbeads. Then, a different type of molecular probe is attached to the surface of each type of microbead. Different types of microbeads are then mixed together

with the biological sample of interest. If a target molecule is present, then it will bind to the exterior of the corresponding microbead. Finally, the microbeads are individually separated, illuminated with UV light, and their individual emission spectra are recorded. The fluorescence from the internal dye provides the optical code to differentiate between types of microbeads, while the presence of the target analyte is indicated by its fluorescent tag. Currently 100 types of microbeads are distinguishable using organic dyes, but the literature suggests that using nanocrystals (NCs) instead of organic dyes could dramatically increase the number of distinguishable microbead types, and hence increase the multiplex capability of this system.

Although the benefits of replacing organic dyes with NCs has been anticipated, there are still very basic questions regarding how a NC based microbead barcode system should be designed that have not yet been addressed. In chapter 4 we first develop a specific proposal for how a NC based system might work, along with a noise model based on what is currently achievable experimentally. A Monte Carlo simulation is used to evaluate the number of distinguishable barcodes given an error rate for different microbead coding architectures. We find that the best results are obtained by using a Monte Carlo code generation algorithm. Our analysis indicates that 1000s of types of microbead barcodes could be distinguishable using a NC based system, a dramatic improvement over the 100 codes that are currently available commercially, but much less than the 40,000 to 1 million that was been speculated in the literature.

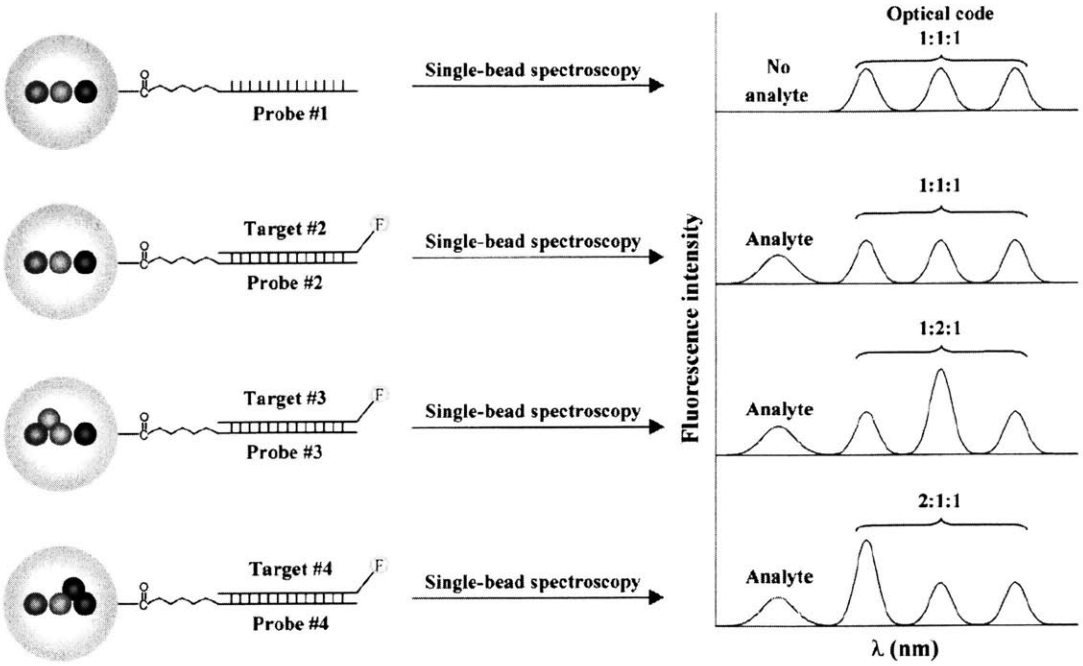

Figure 1-12: Schematic of microbead barcode technology for biological assays. Polymer microbeads are differentiated by the ratios of internal dyes. Each type of microbead is coated with a different type of probe. Target molecules bind to their probes. The individual spectrum of each microbead is measured. The fluorescence from internal dyes provides an optical code that is used to determine the type of microbead, while fluorescence from the tagged target molecules indicate their presence. (from [31])

Chapter 2

Temperature Dependence of the Exciton Transition in Semiconductor Quantum Dots

As the manufacture of colloidal and epitaxial quantum dots (QDs) has matured over the last decade, the usefulness of a physical model to predict the optical behavior of QDs has increased. In particular, modeling the measured temperature dependence of the excitonic energy levels E(T) has attracted attention [16-18, 20]. This is relevant for many quantum dot applications: Changing the exciton energy moves the gain profile in laser applications, introduces chromaticity drift in lighting applications (UK rail specifications allow only 2.5nm chromaticity drift throughout the -20°C to +40°C temperature range for yellow railway signal illuminants. This is difficult to achieve with current yellow LED technology.), and can be used to measure the temperature on the nanoscale (If a monolayer of NCs can be deposited in an optically accessible area of a device such as an organic LED, then the temperature at that layer can be inferred from the color of the photoluminescence.). It is useful to not only characterize the temperature dependence of the exciton energy, but to understand the physics in order to potentially design nanostructures (or choose materials) that have the desired temperature dependence for a particular application.

In bulk semiconductors, it is well known that the temperature dependence of the bandgap is primarily a result of thermal expansion of the lattice and electron-phonon interactions, the later effect being the most important for most semiconductors [15]. Since confinement in a QD changes the electronic energy levels and phonon modes, it has been argued that the electron-phonon interaction strength may change, and as a result the temperature dependence of the excitonic energy may change. References [16-22] all suggest that the E(T) in QDs should be or is modified from the bulk temperature dependence due to modified phonon coupling. Ref [18] notes that "No detailed theory, either first principles or semiempirical, that would allow for an accurate description of E(T), seems to be available for QDs." Ref [18] also notes that for epitaxial QDs (InAs, $In_{0.6}Ga_{0.4}As$, GaAs), the temperature dependence is well described by the bulk value, in contrast to colloidal nanocrystals (CdS, CdSe, PbS, PbSe).

In this chapter we argue that there is no fundamental physical difference between

epitaxial QDs and colloidal nanocrystals (NCs) with respect to E(T) and show that a first order model that only considers changes in the confinement energy with temperature can reasonably explain the behavior of both epitaxial QDs and colloidal NCs. In particular, we show that the size dependence of dE/dT in PbS and PbSe NCs [17] can be attributed to the strong temperature dependence of the effective mass, and hence the confinement energy $E_{conf}(T) \sim m^{-1}(T)$. However, we first present our measurements of E(T) in high quality CdSe/ZnS NCs, for which the temperature dependence of the confinement energy is expected to be minimal. We find that E(T) agrees well with the bulk CdSe dependence for all sizes of NCs, in contrast to previous measurements of CdSe [16] and CdS [21] NCs.

2.1 Experiment

We measured the absorption spectra of 5 sizes of CdSe/CdS/ZnS NCs at temperatures between T=5K and T=300K. However, when we designed our experiment we wanted to measure more than just E(T). We wanted to measure both absorption and emission ensemble spectra from the same physical samples at temperatures between T=5K and T=300K. Furthermore, we wanted the spectra to be indicative of the properties of the individual NCs within the ensemble, so that we could infer properties of a single NC: the temperature dependence of the exciton transition, intrinsic spectral linewidth, and Stokes shift. In this section we discuss all aspects of our experiment, although we will only analyze the temperature dependence of the absorption spectra in this chapter. Chapter 3 will focus on the intrinsic linewidth and the Stokes shift. It will provide the temperature dependence of the photoluminescence (PL) which is important for the applications mentioned in the introduction.

2.1.1 Sample Preparation

In order to get reliable and relevant data, we needed to make trade offs between various characteristics of our samples. Some important considerations in sample preparation were: 1) Optical clarity – This is necessary in order to minimize scattering as light passes through the sample. Scattering manifests itself as a slope in the absorption spectra which makes it more difficult to infer the absorption spectra due NC absorption. 2) Low Optical Density – This is necessary in order to minimize reabsorption and remission which causes a red shift in the

emission spectra. 3) Low NC density – This is necessary in order to ensure that the NCs do not significantly interact with one another. If the NCs are too closely packed, then they can transfer energy from one to another via dipole-dipole coupling. This will cause a redshift in the PL spectrum. 4) Accurate temperature control – If the NC/polymer is too thick then the heat transfer between the middle of the polymer composite and the cryostat will be poor, and this will decrease the ability to control the sample temperature. These were major considerations that dictated many of the choices that we made in our sample preparation.

We embedded NCs in a poly laurylmethacrylate (PLMA) matrix using a procedure similar to the one described in ref. [32]. The basic procedure is: 1) Separate the NCs from their solvent. 2) Mix a monomer, a cross linker, and a catalyst with the NCs. 3) Activate the catalyst by heating to create a NC/polymer composite. However, because our NC samples were different from those used in ref. [32], their procedure needed to be modified in order to achieve a high enough sample quality for our needs. We used 545, 565, 585, 605, and 655 Qdot ITK Organic Quantum Dots from the Quantum Dot Corporation which come in decane with a TOP (trioctyl phosphine) and TOPO (tioctyl phosphine oxide) coating. The high quantum efficiency (>50% at room temperature) of these NCs indicates that the effects of defect/surface states are minimal, while the narrow size distribution allows accurate determination of the bandedge absorption energy.

Before continuing it is worth briefly mentioning some of our failed attempts. Evident Technologies sells CdSe NCs in an optically clear polymer that is similar to NOA (Norland Optical Adhesive) and can be cured with UV light. We mixed dried NCs with NOA and were able to make a reasonably clear NC/polymer composite. We cured the samples under UV, but the resulting samples were quite foggy at room temperature which looked to be the result of tiny cracks in the cured polymer. The PL intensity was also significantly reduced upon mixing with the NOA. We stopped using NOA for both of these reasons. Secondly, we tried incorporating the NCs into polyvinyl butyral (PVB). We dissolved dried NCs with some PVB, deposited drops of the solution onto two separate sapphire plates, waited a few hours for the solution to mostly dry, made a sandwich of the two sapphire plates with the NC/PVB in the middle, and put the sample in an oven at 100°C with a weight on top for half an hour. The heat served to fully dry out the PVB and to allow the polymer to flow. We successfully created an optically clear sample and were able to make accurate absorption measurements. However, the PVB quenched the PL of the NCs dramatically and the signal was not adequate for emission spectra measurements. Accordingly, we discontinued using PVB.

Our initial attempts to incorporate the NCs into PLMA did not work. In order to

incorporate the NCs into PLMA, they must first be separated from the decane solvent. We followed ref. [32] and separated the NCs from the decane using a familiar crash out procedure: add methanol and a little butanol until the mixture becomes cloudy and then centrifuge. The NCs collect on the bottom of the container and the remaining clear solvent can be removed, leaving just some moist NCs. We found that the polymer composite did not cure unless the NCs were thoroughly dried, which we accomplished by pulling vacuum on the NC container for about 1 hour. However, we also found that the crash out procedure removed much of the TOP/TOPO, which we believe caused the NCs to aggregate and resulted in a foggy sample. We tried to add some TOP to the dried NCs, but this also resulted in a foggy sample, possibly because we were unable to accurately add the small amount of TOP that is appropriate for the small amount of NCs sample that we had at our disposal. Eventually, we found that pulling vacuum directly on the NC/decane solution for a few hours removed the decane and left behind an appropriate amount of TOP/TOPO with the dried NCs. This is how we separated the NCs from solvent for all of our final samples.

After drying out 1 mL of QDot solution, we mixed the NCs with a premixed solution of 0.36g of laurylmethacrylate, 0.09g of ethyleneglycol dimethacrylate crosslinker, and approximately 0.005g of azobisisobutyronitrile (AIBN) radical initiator. The resulting solution was often times foggy, which we speculated was due to NC aggregation. However, after about 10 minutes of sonication the solution became optical clear. We then inserted some of the solution between two sapphire plates separated by 380-760μm with two Indium solder spacers. Following Ref. [32], we first tried to cure the samples in an oven at 77°C, but even after many hours our samples did not fully cure. We also tried to cure the sample by illuminating it with a 30W Xenon lamp overnight, but no curing occurred. We then put the samples in an aluminum dish, put it on a hot plate set to 100°C, covered the samples and hot plate with aluminum foil, and waited about 2 hours. The resulting cured samples were optically clear and flush with the sapphire plates on both upper and lower surfaces. We found that if the sapphire plates were spaced much less than 380μm then the curing polymer, which contracts as it is cured, would separate from the surface of the upper sapphire plate and the surface would be too wavy to accurately measure the absorption spectrum. The thicker spacing apparently allows the polymer enough room to bend inwards while curing without cracking or separating from the sapphire plates.

2.1.2 Optical Detection

We used the same optical detection setup to measure both the emission and absorption spectra of our samples. (see Figure 2-1) To measure the absorption spectra we used an LS1 halogen lamp from Ocean Optics as a white light source. The output light is collimated to a beam a few millimeters in diameter, passed through the sample, and collected with a CC3 diffuser attached to a 600μm fiber (both from Ocean Optics). (The diffuser minimizes the sensitivity to the angle and position of the incident beam.) A spectrum is measured by attaching the fiber to an Acton SpectraPro 300i spectrometer with a Princeton Instruments Spec10:400BR back illuminated, deep depletion camera cooled to -80°C. Next, the sample is removed from the beam path, and the halogen lamp spectrum is measured. After subtracting the dark counts from both spectra, the absorption spectrum is calculated by taking the absolute value of the log of the first spectrum divided by the second. The first absorption peaks of our samples have an optical density that varies between 0.04 and 0.07. This low optical density ensures that the PL redshift due to reabsorption and reemission is minimized. The absolute wavelength is verified to an accuracy of λ=1-2nm using the lines of a Mercury Xenon lamp.

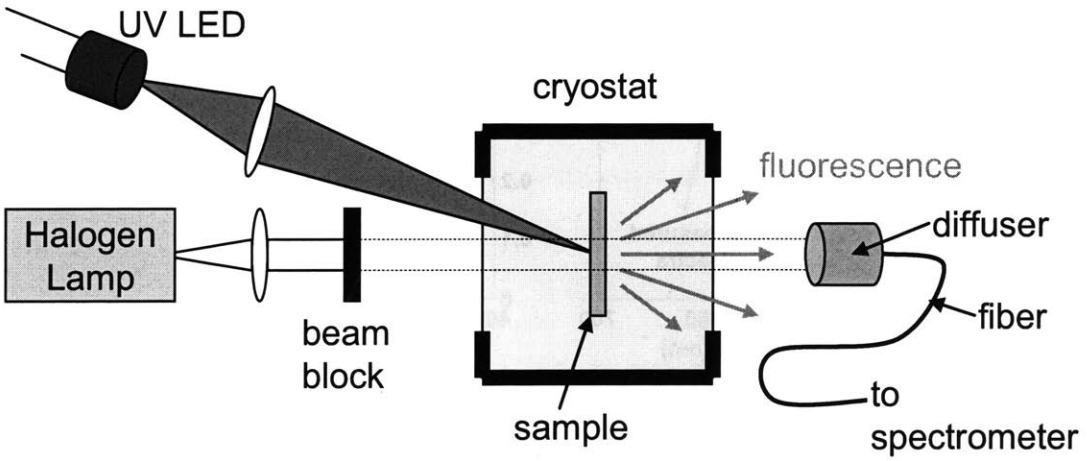

Figure 2-1: Schematic of our experimental setup. To measure emission spectra the UV LED is used to excite samples, while the halogen lamp is blocked. To measure absorption the beam block is used to block the UV excitation.

Accurately measuring the PL spectrum is slightly more complicated. We use a λ=380nm LED (Digikey LX5093SUVC) filtered with UG1 and BG40 colored glass filters as an excitation source. The UV light is focused to a few mm diameter spot on the sample, the NC emission is collected by the fiber, and a spectrum is measured using the same detection system that is used

for absorption. (The halogen lamp is physically blocked while taking emission spectra.) The relative efficiency as a function of wavelength of the detection system is calculated by dividing our measured LS1-CAL halogen lamp (Ocean Optics) spectra by the calibration spectrum sent with the lamp. (see Figure 2-2) It is reassuring that the calculated relative efficiency spectrum agrees well with the efficiency spectrum of the camera multiplied by our grating's spectral efficiency. The actual PL spectrum is then calculated by dividing the raw emission spectrum by the relative efficiency spectrum. We estimate that our calibration procedure corrects the center wavelength of NC PL spectra by up to $\Delta\lambda \sim 1$nm, or $\Delta E \sim 4$meV, which is small but not negligible. This calibration procedure is necessary for accurate measurements of the emission spectra, and we suspect that it is often overlooked by other researchers.

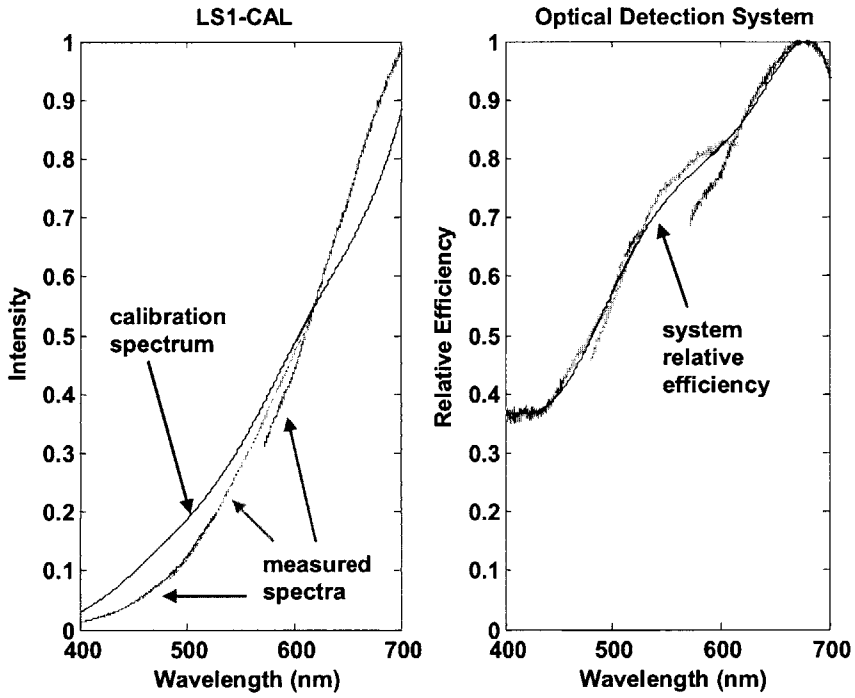

Figure 2-2: Left – Colored lines show the measured spectra of calibration source LS1-CAL at three spectrometer settings. Black line shows the calibration spectrum. Right – Colored lines show the measured spectra divided by calibration spectrum. Black line shows a fit to the colored lines, and is used as the relative efficiency for our optical detection system.

We were also concerned that the details of our LED might affect the measured emission spectra. The $\lambda \sim 20$nm FWHM linewidth of our LED excitation could preferentially excite NCs of a certain size within our inhomogeneously broadened sample. However, an emission spectrum taken with a $\lambda \sim 50$nm FWHM bandpass filtered Xenon lamp was experimentally identical to

spectrum using our LED, and we therefore concluded that any size selective effects of our LED excitation are negligible. Also, the magnitude of the emission spectra scaled linearly with excitation intensity, but the shape did not change. We concluded that our measurements are not sensitive to the LED excitation intensity which in theory could cause heating or have other effects. Using the cross sections of different sized NCs from [33] along with our absorption data, we calculated that the density of NCs in our samples are $1\text{-}2\times10^{15}cm^{-3}$ which corresponds to a NC spacing of approximately 80nm. Energy transfer between NCs is expected to be negligible at this distance.

2.1.3 Temperature Control

Accurately controlling the temperature of the NCs at low temperatures requires careful thermal engineering. Our samples are cooled in an Optistat CFV continuous flow helium cryostat from Oxford Instruments. Our samples are secured to a cold finger with a top plate and four screws. (see Figure 2-3) All thermal connections are made with Indium solder to ensure good heat transfer. [In the cryostat literature GE varnish is often recommended for making a good thermal contact, however our experience was that Indium solder makes a far superior thermal contact and is much easier to use. For example, we originally connected the cold finger to the cryostat body using GE varnish, and we were not able to lower the cold finger temperature below T=10K. After replacing the varnish with Indium solder the cold finger could be cooled below T=5K. We ran into similar problems using GE varnish to attach the sample to the cold finger, but were able to solve them by switching to Indium solder.] Three of the attachment screws passed through 2 or 3 spring loaded washers to ensure that pressure is maintained even if parts thermally expand or contract at lower temperatures. The fourth screw went through a mounting adapter for a silicon diode temperature sensor from Lake Shore (DT-470-BO) that was above the top plate. [We first tried to use silicon diode that was not premounted by Lake Shore and had a lot of difficulty making a good thermal contact to the cold finger without making an electrical contact. We highly recommend using the premounted sensor if possible.] This temperature sensor always agreed to within about T=2K with a sensor embedded in the cryostat body. We concluded that the sapphire plates, which were in the thermal path between the two temperature sensors, were maintained at the same temperature as the cryostat body. However, we were still concerned that there could be a large thermal resistance between the middle of the NC/polymer composite and the sapphire plates on either side. [In our preliminary experiments we created a NC/polymer composite in a

0.25" diameter hole of a metal washer. We mounted the sample/washer in our cryostat without Indium solder thermal connections. In retrospect, we can infer from the PL spectrum that the sample was only at T=150K when the cryostat was at T=5K. This was presumably due to bad thermal contacts between the sample, the washer, and the cold finger, even though they were all in physical contact.]

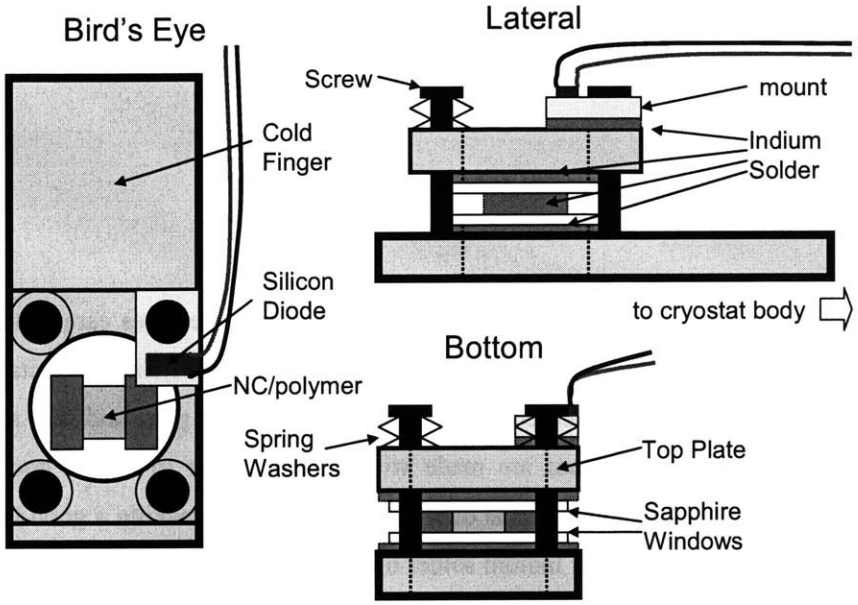

Figure 2-3: Schematic of our sample mounted on the cold finger.

We performed another experiment to validate that the temperature of the NC/polymer composite was cooled to the same temperature as the cryostat. We first set the cryostat to T=77K and measured the PL spectrum of a sample. Then, we removed the sample and immersed it in a dish filled with liquid nitrogen (T=77K) and again measured the PL spectrum. The two spectra were experimentally identical, and therefore we concluded that the cryostat temperature sensor accurately indicated the sample temperature at low temperatures. (The center wavelengths agreed to within λ=0.2nm, which is quite close considering that the PL wavelength shifts by λ=20nm as the temperature is changed from T=300K to T=77K.)

2.1.4 Data Processing

Since most of the theoretical models of NCs are reported in terms of energy, as opposed to

wavelength, it is convenient to transform the axes of our spectra from wavelength to energy in order to compare with theory. While this is trivial for an absorption spectrum, simply convert λ to $E=2\pi\hbar c/\lambda$ and replot the data, this is an INCORRECT procedure for emission spectra. An absorption spectrum is unitless, since it is the ratio of the POWER OUT divided by the POWER IN. The emission spectrum, on the other hand, has units. It measures the optical power per unit wavelength or per unit energy. Since $\Delta E=-2\pi\hbar c(\Delta\lambda)/\lambda^2$, simply converting the x-axis from λ to E and then replotting the emission data on the energy axis is incorrect, although this is correct for absorption. A correct procedure is to multiply the emission spectra by λ^2 and then plot on the energy axis. To illustrate this, figure 2-4 shows the theoretical blackbody spectrum for an object at T=3000K, and the spectrum that would be measured using a spectrometer. Simply converting the spectrometer bin wavelengths to energy, and replotting gives an incorrect result, as fig. 2-4 shows. Since the spectrometer bins are spaced evenly in wavelength, they are unevenly spaced in energy. Finally, fig 2-4 shows the result when the correct procedure is used. This procedure is more important for spectra with larger linewidth:wavelength ratios. The incorrect procedure causes only about a 5 meV error in our PL data, which is small but not negligible. We suspect that the incorrect procedure is common in the literature.

Additionally, there were some complications with the absorption spectra due to scattering. At T=300K, all of our samples were optically clear with flat absorption spectra at energies lower than the first absorption peak. However, by the time they had been cooled to about T=230K they became visibly foggy. This showed up as a negative slope when plotting the absorption spectra versus wavelength, and is presumably due to Rayleigh scattering. In order to correct for this we have subtracted off a variable straight line background from the absorption in the wavelength domain. We found that the fogginess was reversed when the sample temperature was returned to T=300K. In fact, we took 2 sets of data on the same physical sample and the data was experimentally identical. We speculate that some molecule in our sample came out of solution at lower temperatures, and went back into solution when the temperature was returned to T=300K, but we are not sure.

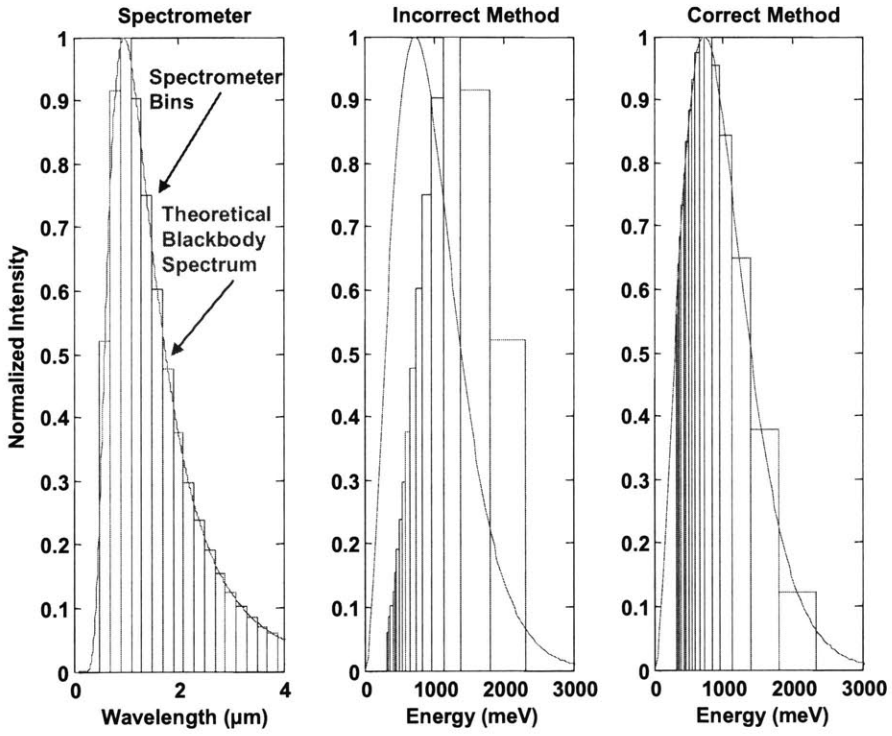

Figure 2-4: Simulation of data processing procedure. Left – Shows the theoretical T=3000K blackbody spectrum, along with a spectrometer measurement. Center – Shows the results of applying the incorrect data processing. Right – Shows the results using the correct procedure – multiply the spectrometer data by λ^2, convert λ to E, and then replot.

2.2 Experimental Results

The absorption spectra are fit to a series of either 2 or 3 Gaussians. Figure 2-5 shows the temperature dependence of the lowest energy absorption peak E(T) for all of our samples along with the raw absorption spectra at T=300K. (For the largest NCs, we use an average of the 1st and 2nd absorption features, since the lowest energy feature is partially buried beneath the 2nd feature and therefore the least squares fit is not sensitive to its position.) Our measured values of dE/dT are experimentally identical for all 5 NC sizes and agree well with the average bulk value of dE_{bulk}/dT=-0.36meV/K from T=100-300K. Our results are in contrast to previous measurements in CdSe [16] and CdS [21] NCs which indicate that the magnitude of dE/dT scales with NC size. We believe that our data is more reliable for several reasons. 1) Our implied size dispersion is narrow enough (σ_R/R~5%) that we are able to measure the shift of the bandedge absorption directly, while in [16] Stark spectroscopy is necessary to extract dE/dT values. The interpretation of Stark spectra of CdSe NCs is complicated since the electric field is known to

cause state mixing [34] and therefore may modify dE/dT. 2) NC manufacturing has improved dramatically in the last decade, so that we are confident that our NCs have a CdSe core. In contrast, measurements of CdS NCs in 1994 show a size dependent E(T) [21], but have a S/Cd ratio as low as 0.2, instead of 1.

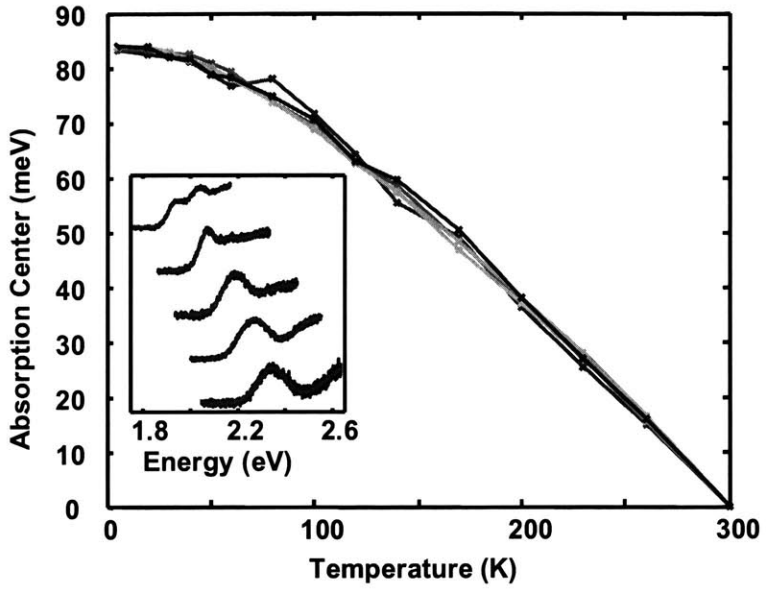

Figure 2-5: Temperature dependence of the lowest absorption feature for 5 sizes of CdSe/ZnS NCs from the QDot Corporation (655nm, 605nm, 585nm, 565nm, 545nm). Inset – Raw absorption data for all 5 samples at T=300K.

2.3 Analysis

In light of our different experimental results it is appropriate to revisit the analysis in [16] of the physical mechanisms that contribute to dE/dT in CdSe NCs. Additionally, it is important to consider experimental data of quantum dots in other material systems.

2.3.1 CdSe Nanocrystals

In bulk CdSe the temperature dependence of the bandgap is thought to result primarily from changes in the electron-LO phonon self-energy [15]. However, dE/dT could be modified in a NC due to changes in the pressure, Coulomb energy, exciton-phonon scattering, and the confinement energy. 1) Since our NCs have a ZnS capping layer, the CdSe core could potentially experience a

temperature dependent strain, due to different thermal expansion coefficients. However, we believe that strain effects are minimal since adding the ZnS cap causes a red shift in the exciton energy [35], not a blue shift as is expected for increasing pressure (dE/dP is positive). 2) Since the electron and hole wavefunctions are confined in a NC and therefore have a greater overlap than a bulk exciton, the Coulomb energy is higher in a NC. Since the Coulomb energy depends on the dielectric constant and the dielectric constant depends on temperature, dE/dT will be modified. Assuming that the Coulomb energy in a NC scales as 1/R, that $E_{Coulomb}$=15meV for the bulk exciton radius R=5.6nm, and that ε_{300K}=9.64 and ε_{100K}=9.17, we have calculated the dielectric contribution to dE/dT to have a maximum effect of about -0.01meV/K for our smallest NCs. (see Figure 2-6)

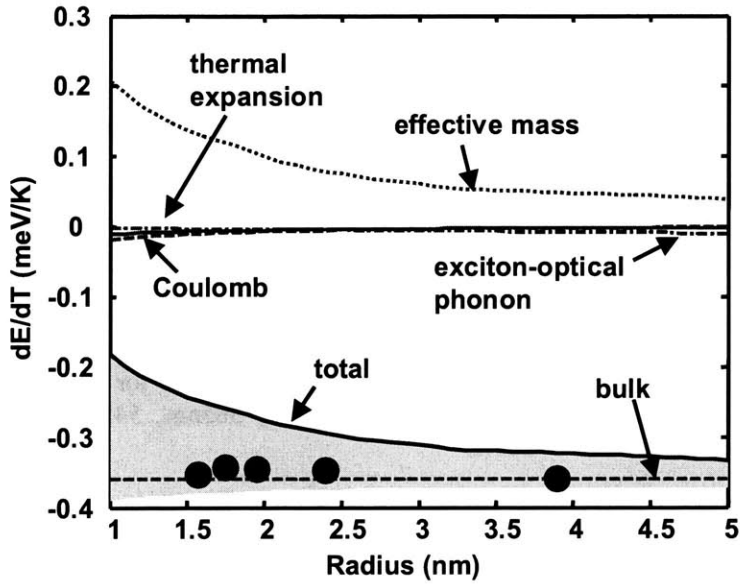

Figure 2-6: Calculated contributions to dE/dT for a CdSe NC: Coulomb energy, exciton-optical phonon scattering, thermal expansion, and effective mass (see text). Shaded area indicates the calculated range of dE/dT due to uncertainty in the effective mass contribution. Circles – experimental values.

3) Exciton-phonon scattering is expected to be modified in a NC since the phonon density of states, the electronic structure, and exciton wavefunction are different than in bulk. It has been suggested that this modification may lead to a change in dE/dT for NCs [16-18, 20]. The independent boson model is commonly used to describe exciton-phonon interactions in NCs [16, 36], but this model does not lead to a change in dE/dT [37]. A second order model which allows for the virtual absorption and emission of phonons and does modify dE/dT is simulated in [38] for optical phonons in CdSe NCs. The shift in energy $\hbar\Delta_{opt}=B\times N$ scales as the optical phonon

Boltzmann occupation N and the constant B can be inferred from simulations of the optical phonon contribution to the linewidth δ_{opt} in [38]. The contribution to dE/dT is quite small, reaching a magnitude of only about -0.01meV/K for R=5nm. (see Fig. 2-6)

4) Finally, there will be some contribution to dE/dT due to a change in confinement energy with temperature. Assuming an infinite potential well and a parabolic bandstructure, the confinement energy is given by $E_{conf} = \frac{\hbar^2\alpha^2}{2mR^2}$ where α is a geometric constant, m is the exciton effective mass, and R is the radius of the confining potential. Taking the first derivative with respect to temperature we find $\frac{dE_{conf}}{dT} = E_{conf}\left[\frac{-1}{m}\frac{\partial m}{\partial T} - \frac{2}{R}\frac{\partial R}{\partial T}\right]$, and we can therefore estimate the contribution to dE/dT due to changes in the confinement energy. The thermal expansion coefficient is approximately 5×10^{-6} for CdSe and therefore the second term is negligible [16]. We are not aware of any data on the temperature dependence of the effective mass in CdSe, but this can be estimated using Kane's k•p formula $\frac{1}{m^*(T)} = \frac{1}{m_e} + \frac{2\hbar^2\left|\langle p\rangle_{cv}\right|^2}{m_e^2 E_g(T)}$, where m_e is the mass of an electron, p_{cv} is a coupling constant, and $E_g(T)$ is the bulk bandgap. Since we know that the effective mass of CdSe is about $0.12m_e$ and we know dE_g/dT=-0.36 meV/K, we estimate a percentage change in effective mass of about 2×10^{-4}/K, although this is likely an overestimate since Kane's formula tends to overestimate the temperature dependence in other materials [39]. This effect is potentially the largest modification to dE/dT in a CdSe NC by far. However, in materials such as PbS and PbSe where the percentage change in effective mass with temperature has been measured to be quite large, 8.5×10^{-4}/K and 1.2×10^{-3}/K respectively at T=300K [40], we expect this effect to dominate.

2.3.2 Other Materials

Figure 2-7 shows our measured dE/dT values for CdSe NCs and experimental dE/dT values in other materials, all normalized by their bulk dE_{bulk}/dT values. While dE/dT in CdSe, InAs, InGaAs, and GaAs nanostructures are experimentally identical to their bulk values ($(dE/dT)/(dE_{bulk}/dT) = 1$), dE/dT in PbS and PbSe NCs decreases in magnitude with increasing confinement energy and actually goes to dE/dT=0 for PbS NCs with a confinement energy of approximately 700meV. To quantify the importance of the temperature dependence of the

effective mass on dE/dT for PbS and PbSe, we have subtracted this contribution $E_{conf}\left[\frac{-1}{m}\frac{\partial m}{\partial T}\right]$ from the raw data and plotted the result (open symbols) in Fig. 2-7. The resulting values of dE/dT are much closer to the bulk value dE_{bulk}/dT (their ratio is approximately one) across a range of sizes for both PbS and PbSe. We conclude that the temperature dependence of the effective mass can account for the majority of the size dependence in dE/dT for PbS and PbSe NCs. This effect was ignored in the analysis of [17]. We believe that our interpretation is strongly supported by measurements of PbSe NCs which show that the ratio of the second to first exciton confinement energies remains constant as a function of temperature [41], even though the first exciton confinement energy is strongly temperature dependent. If dE/dT were being modified by strain effects, for example, then we would not expect this ratio to remain constant. CdSe, InAs, InGaAs, and GaAs are expected to have a weaker percentage change in effective mass with temperature and hence are expected to have dE/dT values much closer to their bulk values, as Fig. 2-7 shows is the case. It is important to note that our model will break down once the confinement becomes so strong that the electrons occupy k states further from the band minimum and the parabolic band approximation breaks down. Since this breakdown occurs for confinement energies of about 800meV and 600meV for PbS and PbSe, we have only included data points with these lower confinement energies in Fig. 2-7.

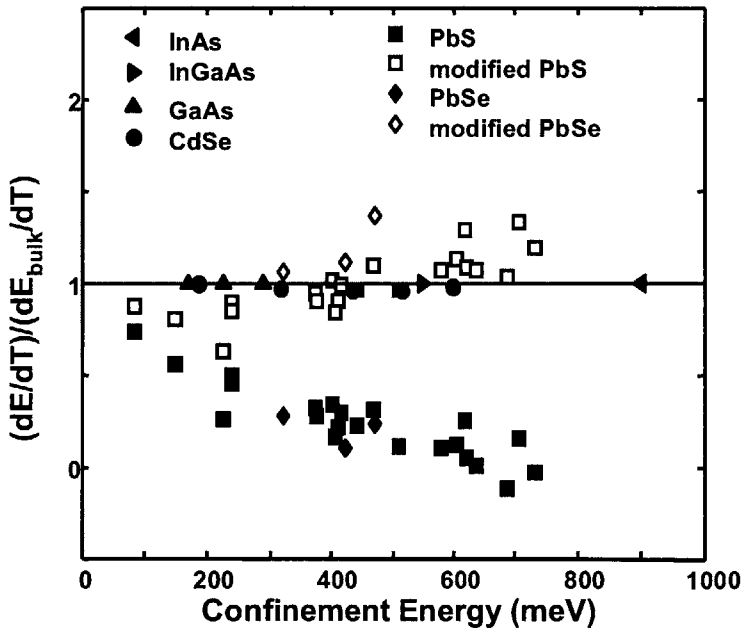

Figure 2-7: Filled shapes are raw experimental data for InAs [18], $In_{0.6}Ga_{0.4}As$ [18], and GaAs [20] epitaxial QDs, and CdSe (this work), PbS [17], and PbSe [17] NCs. Open shapes show PbS and PbSe data after subtracting the expected contribution of effective mass to dE/dT.

2.4 Conclusions

In conclusion, we have shown that a first order model that only considers changes in the effective mass with temperature can explain the existing experimental measurements of dE/dT for both epitaxial QDs and colloidal NCs, and hence both types of systems can be modeled using the same physical framework. Our absorption measurements of high quality CdSe/ZnS NCs show that there is no measurable size dependence to dE/dT, in contrast to earlier measurements in lower quality CdSe and CdS NCs. We are able to explain most of the size dependence in dE/dT in PbS and PbSe NCs by the strong temperature dependence of the effective mass of these materials. Previous explanations neglected this simple, yet dominant physical effect. We do not know of any experimental evidence that indicates that E(T) should be modified in nanostructures due to changes in exciton-phonon coupling. However, the next chapter will consider how exciton-phonon coupling scales with NC size and the effect on NC optical spectra.

Chapter 3

The Stokes Shift and Spectral Linewidth of CdSe Nanocrystals

Nanometer size structures have enabled the control of excitonic transition energies through confinement of the electron/hole wavefunctions. This has allowed the fluorescent properties of CdSe nanocrystals (NCs) to be tailored to any wavelength across the visible spectrum by controlling their size [32]. A desire to understand the physical mechanisms responsible for the optical properties of NCs, including the Stokes shift and the spectral linewidth, has lead to various theories about the fine structure of the bandedge exciton [3] and exciton-acoustic phonon coupling [27, 38].

In this chapter, we consider both perspectives in the analysis of the experimentally measured exciton fluorescence, absorption, and Stokes shift. Analysis of the observed temperature dependence of the Stokes shift through the lens of exciton fine-structure is a rigorous test of existing theory and can assist in locating the excitonic excited states with precision. However, if the same data is analyzed through the lens of strong exciton-acoustic phonon coupling, an alternative physical picture develops that can quantitatively reproduce the observed Stokes shift and exciton linewidth. Consideration of both theories in light of the data presented suggests that neither explanation is complete, and in fact both are demonstrably flawed when considering *both* ensemble and single particle data. Additionally, we infer the room temperature intrinsic linewidth of NCs for different sized NCs from our experimental data. As discussed in Chapter 1 this is an important parameter for determining the "fundamental limits" of many potential NC applications.

3.1 Introduction

Figure 3-1 shows schematically how the fine structure and exciton-acoustic phonon scattering theories account for the Stokes shift and linewidth broadening of NC ensembles with an inhomogeneous size distribution. This section discusses in detail the physics that is used to derive these theories and their implications.

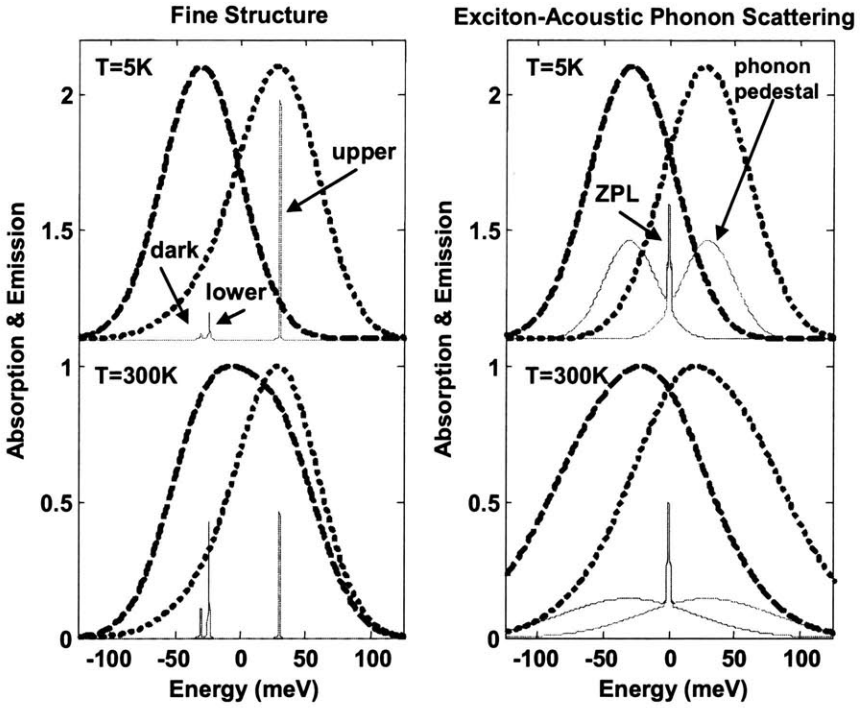

Figure 3-1: Schematic of fine structure and acoustic phonon theories applied to an ensemble with an inhomogeneous size distribution. The thick lines show the convolution of the single NC emission (dashed) and absorption (dotted) with an inhomogeneous size distribution. Upper Left – thin lines show absorption of a single NC, while the single NC emission is mostly from the lowest energy level at T=5K. Lower Left – Thin lines show the predicted single NC emission at T=300K by assuming an oscillator strength weighted Boltzmann distribution. This change in single NC emission causes the Stokes shift to decrease and the ensemble emission linewidth to broaden. Upper Right - According to the independent boson model of exciton-acoustic phonon coupling, the single NC absorption and emission have a Prussian helmet shape that consists of a sharp zero phonon line and a broad offset acoustic phonon pedestal, and they are mirror images of one another about the zero phonon line. Lower Right – At higher temperatures the acoustic phonon pedestal broadens and this causes both the emission and absorption spectra to broaden, but the Stokes shift does not change.

3.1.1 Fine Structure Theory

The fine structure is derived by considering confinement effects within a multiband effective mass framework. The analysis of CdSe NCs in [3] accounts for the effects of the hexagonal lattice structure, crystal shape asymmetry, and electron-hole exchange interaction, and results in five sublevels with different oscillator strengths including a dipole forbidden 'dark exciton' [3]. Evidence for the fine structure theory includes 1) PLE (photoluminescence excitation) and FLN (fluorescence line narrowing) spectroscopies which show sharp features in the spectrum of the bandedge exciton that compare reasonably well with theoretical predictions [24], and 2) Measurements of the low temperature fluorescence lifetime dependence on both magnetic field [3] and temperature [42-44] which are consistent with the existence of a dark exciton. While the fine structure is usually invoked to explain the Stokes shift, exciton-acoustic phonon scattering is usually invoked to explain the spectral linewidth.

In the fine structure theory, the bandedge exciton consists of multiple discrete energy levels. The single NC absorption spectra consist of sharp lines, weighted according to their oscillator strengths, while the emission spectra consists of sharp lines weighted according to an oscillator strength weighted Boltzmann distribution. (see figure 3-1) The single NC emission spectra changes as a function of temperature, which can result in ensemble broadening, while the absorption spectra is predicted to be temperature independent. Figure 3-2 shows how the strong temperature dependence of the Stokes shift arises for an example based on [3] with 4 energy levels (0^U, 1^U, 1^L, 2). Boltzmann statistics are used to calculate the occupation probability for each sublevel. This means that the ratio of occupation probabilities for states with energies E_1 and E_2 is given by $\frac{P_1}{P_2} = e^{\frac{-(E_1-E_2)}{k_B T}}$. At low temperatures the lowest energy levels are preferentially occupied, but at higher temperatures the occupation probabilities will become equal. When there are many states, the occupation probability of state n is given by $P_n = \frac{1}{C} e^{\frac{-E_{ni}}{k_B T}}$ where C is a normalization given by $C = \sum_i e^{\frac{-E_i}{k_B T}}$. The relative probability of emission PE_i/PE_j for two states is given by the ratio of their respective occupation probabilities P_i multiplied by their respective oscillator strengths o_i, or $\frac{PE_i}{PE_j} = \frac{P_i o_i}{P_j o_j}$. When there are many states, the emission probability of state n is given by $PE_n = \frac{o_n}{K} e^{\frac{-E_{ni}}{k_B T}}$ where K is a normalization

given by $K = \sum_i o_i e^{\frac{-E_i}{k_B T}}$. As Fig. 3-2 shows, this can lead to a complex temperature dependence when there are many levels. At high temperatures the emission probabilities will approach their normalized oscillator strengths, and will have the same spectrum as absorption. At low temperatures, the Stokes shift is large since most of the emission is from the low energy 2 state while the absorption is dominated by the high oscillator strength 0^U and 1^U states. At higher temperatures, the Stokes shift approaches zero.

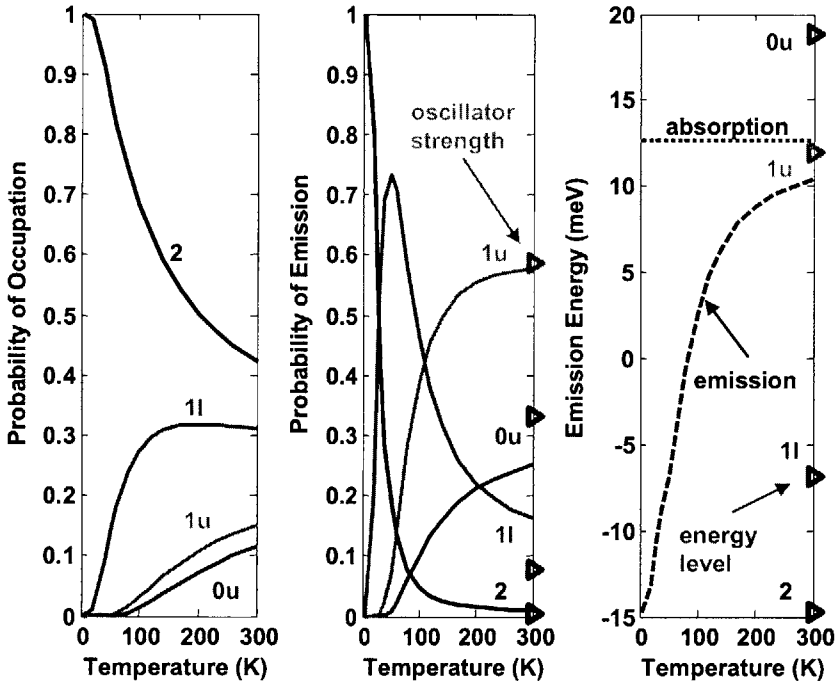

Figure 3-2: Left – Occupation probability calculated using Boltzmann statistics for the energy levels shown on the right. Center – Emission probability is calculated by multiplying the occupation probability by the oscillator strength. The oscillator strengths are shown as triangles. Right – Absorption energy is the sum of the oscillator strengths multiplied by the energies. The emission energy is the sum of the occupation probabilities multiplied by the energies. The energy levels are shown as triangles.

3.1.2 Exciton-Acoustic Phonon Scattering Theory

Exciton-acoustic phonon scattering is expected to be dominated by the deformation potential in CdSe NCs [27]. The deformation potential in a bulk material refers to the fact that the bandgap changes when a material is compressed. Since acoustic phonons locally compress a material,

they change the local bandgap, and hence change the energy of a localized exciton, which has an electron in the conduction band and a hole in the valence band. In NCs this interaction is normally modeled using the independent boson model [37], is expected to scale like $1/R^2$ [27], and has a magnitude that can be calculated using bulk material parameters [38]. The resulting absorption and emission spectra consist of a broad acoustic phonon pedestal under a narrow and offset (polaron shifted) ZPL (zero phonon line) whose shape has been described as a "Prussian helmet" [30]. Evidence for exciton-acoustic phonon coupling includes 1) Spectral hole burning experiments which show a sharp peak on top of a broad pedestal in self assembled CdSe QDs [45] and CdSe NCs [29], 2) Single CdTe QD emission spectra showing a sharp line on a broad pedestal [46], and 3) Femtosecond photon-echo experiments that measure spectra of CdSe NCs with a size and temperature dependence that is consistent with calculated exciton-acoustic phonon coupling [28]. While the spectral broadening effects of exciton-acoustic phonon coupling have been widely appreciated, the contribution of exciton-acoustic phonon coupling to the Stokes shift has not.

The Prussian helmet spectrum has two parts: the ZPL and the acoustic phonon pedestal. (see Fig. 3-1) For emission, the ZPL physically corresponds to an exciton recombining and emitting one photon, with no change in phonon occupation. Alternatively, an exciton can create both a photon and a phonon upon recombination. For optical phonons, this process leads to optical phonon replicas which are spaced in multiples of the optical phonon energy $\hbar\omega$=26meV on the low energy side of a single NC emission spectra. (see Figure 3-5) Since there many acoustic phonon modes with different energies, the same physical effect is expected to manifest itself as an acoustic phonon pedestal on the low energy side of the ZPL. At higher temperatures, when the acoustic phonon modes of a NC are thermally populated, a recombining exciton can emit a photon while annihilating a phonon and therefore the emitted photon will have a higher energy than the ZPL. This process is not possible at T=0K, since there are no phonons to be annihilated. Thus, the phonon pedestal becomes broader with temperature. Importantly, the ZPL is offset from acoustic phonon pedestal. (see Fig. 3-1) Intuitively, this offset occurs because the lowest energy lattice configuration of the NC is depends on whether an exciton is present or not. When there is an exciton present the equilibrium lattice configuration will relax in order to lower the bandgap, and thus reduce the energy of the exciton. The lattice relaxation energy is often referred to as a polaron shift. When the exciton recombines, the lattice will return to its original configuration. Figure 3-3 shows a schematic of what happens.

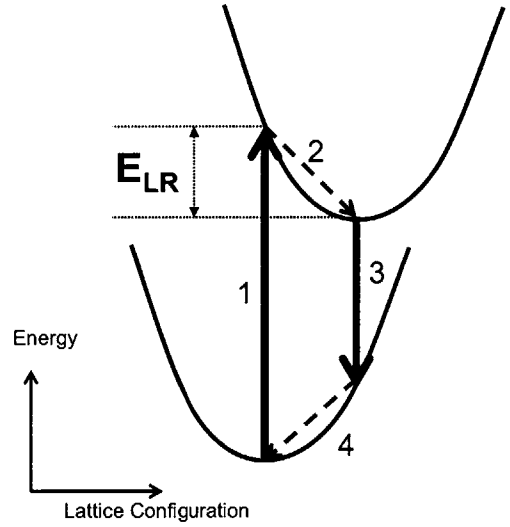

Figure 3-3: Schematic of how the lattice configuration changes within the independent Boson model. 1. NC absorbs a photon 2. lattice configuration relaxes 3. Photon emitted 4. lattice configuration relaxes back to original position.

For the exciton-acoustic phonon scattering model the emission spectrum is a mirror image of the absorption spectrum about the ZPL. For CdSe NCs, the acoustic phonon pedestal is expected to have most of the oscillator strength [45] and therefore the Stokes shift is approximately twice the polaron shift. (see Figure 3-1) In the independent Boson model, the Stokes shift is expected to be temperature independent and the ensemble emission and absorption linewidths are expected to broaden equally due to higher population of acoustic phonons at higher temperatures.

3.1.3 Outline

In the following sections, we present our measurements of the temperature dependence of the Stokes shift and spectral linewidth in high quality CdSe NC ensembles along with a single NC photoluminescence (PL) spectrum, and show that neither theory by itself is able to adequately explain our experimental results. In Section 3.2 we present our experimental data. In Section 3.3 we analyze the nonresonant Stokes shift, which has previously been primarily attributed to the exciton fine structure [3, 47]. If this model is correct, then our measurements of the temperature dependence of the Stokes shift allow us to infer the energy spacing and oscillator strength of the fine structure. Using this model, our results can be made to roughly agree with theoretical

predictions. We show that the lattice relaxation energy due to acoustic phonons that is implicit in the exciton-acoustic phonon scattering theory developed in [38] can reasonably account for both the magnitude and size dependence of the Stokes shift. In Section 3.4 we show that the fine structure is unable to explain our measured spectral broadening, while the exciton-acoustic phonon model shows reasonable agreement. However, we show that the exciton-acoustic phonon scattering theory is inconsistent with single NC emission spectra. We conclude that neither theory is able to explain our experimental results. In Section 3.5 we speculate that a model that consistently treats both the fine structure and the exciton-acoustic phonon interaction in the same physical framework is required to explain our measured anomalous Stokes shift. Section 3.6 discusses the inferred room temperature intrinsic single NC linewidth and the range of spectral diffusion. Section 3.7 reviews our calculation of the contribution of the inhomogeneous size distribution to the Stokes shift, before concluding in Section 3.8.

3.2 Experiment

We have taken absorption and emission spectra of 5 types of CdSe/ZnS NCs. Chapter 2 describes the details of our experimental setup, but we will briefly review the key considerations. In order to verify that the nonresonant Stokes shift is due to the intrinsic NC physics, we have taken care to minimize potentially distorting effects. The high quantum efficiency (>50% at room temperature) of these NCs indicates that the effects of defect/surface states are minimal, while the narrow size distribution minimizes the effects of the inhomogeneous contribution to the Stokes shift. We have embedded the NCs in a poly laural methacrylate (PLMA) matrix using a procedure similar to the one described in reference [32]. The NC/polymer composite was cured between two sapphire windows that were separated with Indium foil spacers (380-760μm) [23]. The first absorption peak has an optical density that varies between 0.04 and 0.07 for our samples. This low optical density ensures that the PL redshift due to reabsorption and reemission is minimized, while the low volume density of the NCs ($<5x10^{15}$ cm^{-3}) ensures that the NCs do not interact. Previous measurements had optical densities up to 0.3 which corresponds to 50% light absorption, and could lead to a significant red shift due to reabsorption and reemission [47]. Figure 3-4 shows the raw PL and absorption data for all of our samples at T=5K and T=300K, along with a fit to the absorption using a series of either 2 or 3 Gaussians. Figure 3-5 shows a single NC PL spectrum from the same physical batch of NCs that we used for the smallest NC ensemble measurements.

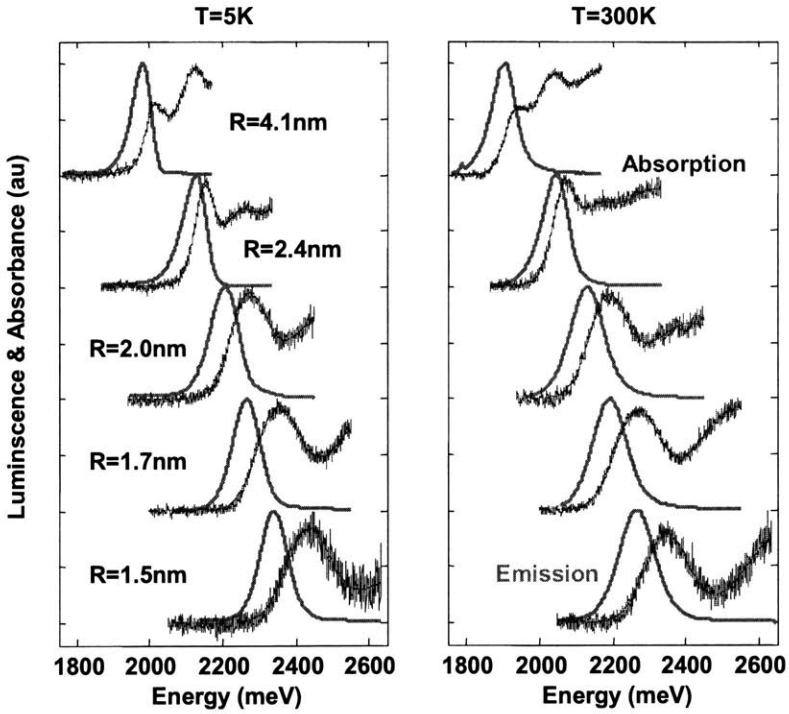

Figure 3-4: Raw PL (green) and absorption (blue) measurements for 5 samples of QDots (from top to bottom: 655, 605, 585, 565, 545) at T=5K and T=300K. The fit to a series of Gaussians is shown on the absorption spectra. The NC sizes are determined by comparing to the spectra in [24, 47, 48]. The range of implied radii are (3.5-4.3nm, 2.2-2.6nm, 1.7-2.2nm, 1.5-2.0nm, 1.35-1.8nm) respectively.

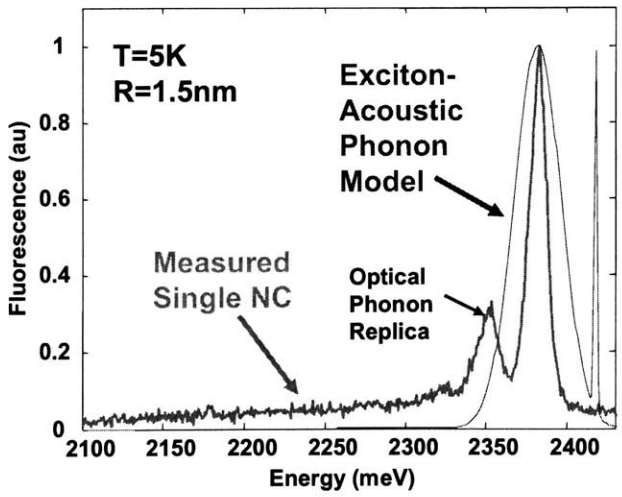

Figure 3-5: Single NC emission spectra from the same physical batch of 545 NCs that are used in the PL and absorption measurements.

Figure 3-6 shows the temperature dependence of the Stokes shift, PL ensemble linewidth, and PL center wavelength. The Stokes shift is weakly dependent on temperature and increases as size is decreased, in qualitative agreement with previous measurements [47]. The ensemble linewidth increases with temperature for all NC sizes, but has the strongest dependence for the smallest NCs. The temperature dependence of the center wavelength of the PL spectra is similar for all sizes, decreasing as a function of temperature except at low temperatures where there is a 2-4meV increase between T=5K and T=20K. We note that our R=2.4nm sample stands out from the other samples with regards to its small Stokes shift, weakly temperature dependent linewidth, and asymmetric emission spectrum. We are unsure if this is due to the intrinsic physics of R=2.4nm NCs or if there was a difference in the NC growth. We include all of the R=2.4nm data, but view it with some suspicion.

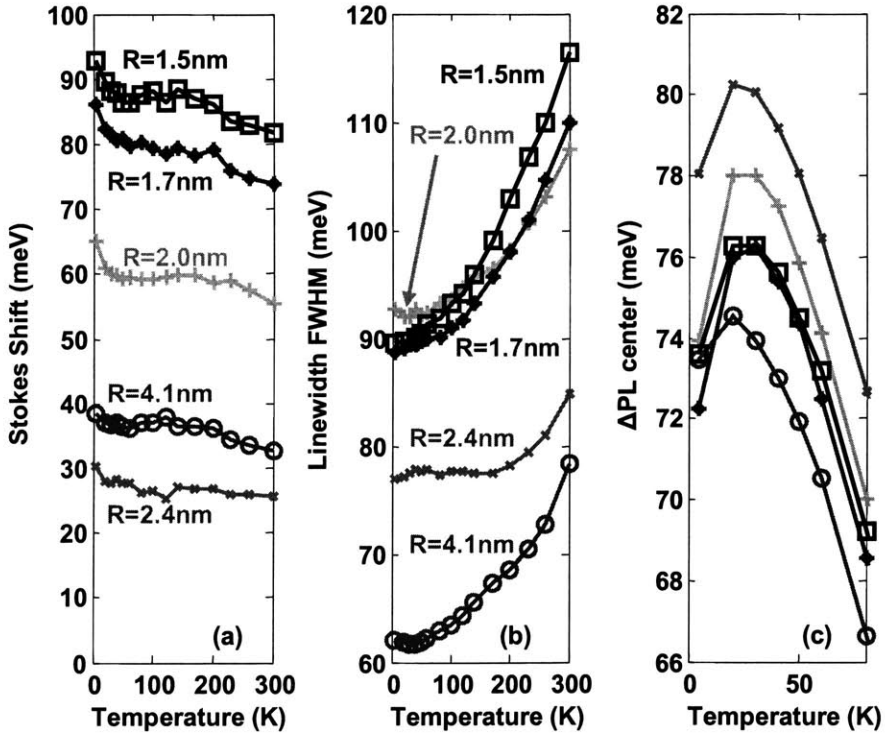

Figure 3-6: Left - Temperature dependence of the non-resonant Stokes shift for all 5 of our samples. Center – Ensemble emission linewidth versus temperature. Right – The temperature dependence of the emission wavelength is similar for all samples (in the plot the PL center is normalized to zero at T=300K for all samples). All samples have a "hook" at low temperatures that is consistent with emission from a dark exciton.

3.3 Analysis – Temperature dependence of the Stokes shift

Existing theory attributes the non-resonant Stokes shift to a combination of optical phonon replicas, the exciton fine structure, and the inhomogeneous size distribution in a NC ensemble. We consider the contribution of each to the Stokes shift. Optical phonons have a narrow energy range around $\hbar\omega$=26meV, and optical phonon assisted transitions manifest themselves as optical phonon replicas. To estimate the contribution to the Stokes shift, we follow the analysis in reference [3] which results in a contribution of 15meV independent of size and temperature, although it should be noted that this is very rough since the optical phonon replicas are not accurately described in the independent Boson model as is shown in reference [49]. Next, there is a Stokes shift that is due to the inhomogeneous size distribution. Since NC absorption cross sections scale as R^3 [3] away from the bandedge, large NCs preferentially absorb UV excitation resulting in a red shift of the ensemble PL spectrum. However, since the oscillator strength of the first absorption feature scales as R [33], the first absorption feature is also red shifted and partially cancels the first effect. Using appropriate inhomogeneous size distributions for our samples, we find a temperature independent contribution of only 4-8meV to the Stokes shift. Finally, the fine structure is assumed to account for the remaining Stokes shift and is calculated by assuming an oscillator strength weighted Boltzmann occupation of the fine structure energy states calculated in ref. [3]. In contrast to the previous explanation of the room temperature Stokes shift [47], we assume that the oscillator strengths for the PL are the same as those for absorption. (In [47] it is assumed that the oscillator strength of the three optically active energy levels are equal for emission, but different for absorption. Since we see no physical justification for this model, and none is given, we assume the oscillator strengths are the same for absorption and emission. This leads to almost no change at low temperatures, but gives a significantly lower Stokes shift than previously calculated at room temperature.) Figure 3-7 shows that the *a priori* predicted temperature dependence of the Stokes shift using the current literature model does not match experiment very well. (Our model is based on the analysis in ref. [3] but is slightly simplified. We haven't included the optically inactive states ($\pm 2, 0^L$) since they are not important for the temperature dependence of the Stokes shift between T=40K and T=300K. Also, we have combined the ($0^U, \pm 1^U$) levels, since they are spaced relatively close together.) According to the model, at low temperatures for small NCs, the Stokes shift is dominated by the fine structure contribution: emission occurs from the lowest energy 'dark' exciton state and the upper levels which have most of the oscillator strength dominate the absorption. The theory predicts a strong temperature dependent Stokes shift, which we do not observe experimentally.

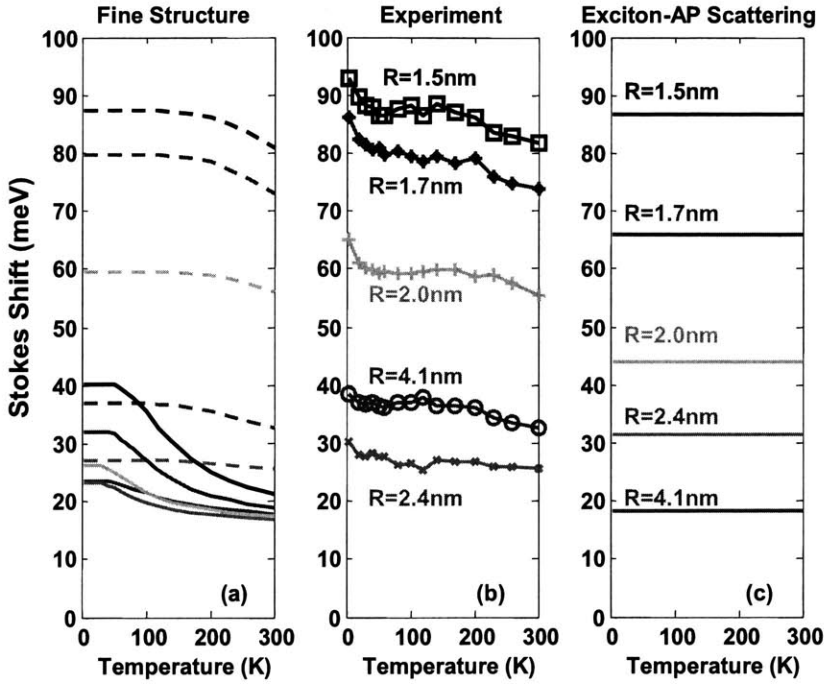

Figure 3-7: Left – The solid lines show the *a priori* prediction for the temperature dependence of the Stokes shift according to the fine structure theory. The plot assumes that there is a 15meV Stokes shift for all sizes and temperatures due to effects other than the fine structure, and the fine structure is assumed to look like the solid lines in bottom plot. The dashed lines correspond to a least squares fit of the fine structure to our data. The resulting energy and oscillator strengths are shown with the circles in Figure 3-8. Center – Repeat of Stokes data. Right – predicted temperature dependence of Stokes shift according to exciton acoustic phonon scattering theory for a CdSe core in a SiO_2 matrix.

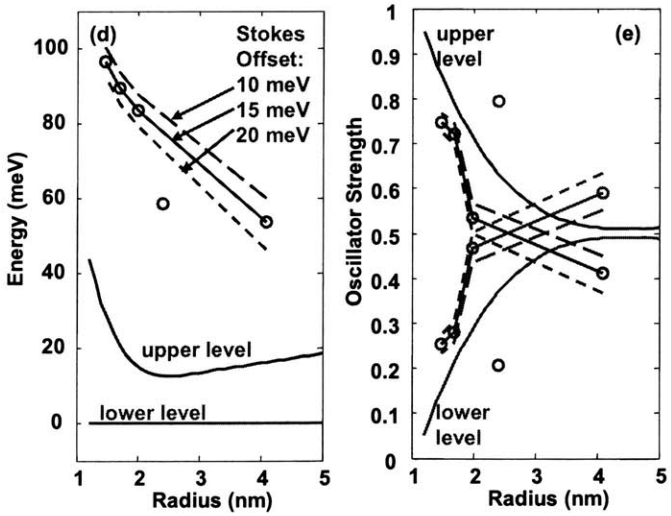

Figure 3-8: The solid line shows the simplified 2 level *a priori* theoretical fine structure based on ref. [24]. Circles show the implied energy and oscillator strength from a least squares fit to our experimental data. We vary the magnitude of the temperature independent Stokes contributions. The R=2.4nm data is skipped because of its unusual properties (see text in section 3.2).

However, figure 3-8 shows that by modifying the fine structure a reasonable agreement can be reached. If the fine structure model is correct, then the temperature dependence of the Stokes shift is an extremely sensitive way to measure the upper energy levels and oscillator strengths of the fine structure. Many previous experiments have measured the energy levels and relative oscillator strengths of the "dark" and lower fine structure energy levels using the temperature dependence of the lifetime at low temperatures [42, 43]. In fact, our experimentally measured PL wavelength shows a "hook" at low temperatures (see figure 3-7) that is consistent with the existence of a dark exciton about 2-4meV below the lowest allowed bright exciton level. At T=5K almost all of the emission is expected to occur from the dark exciton, while at T=40K almost all of the emission is expected to occur from the lower bright exciton level. (Importantly, our measurements show that the first absorption feature does not have a "hook" at low temperatures [23].) Our measurements of the dark exciton energy relative to the lowest bright exciton energy are consistent with previous lifetime measurements [42], but the upper exciton energy is 3x-5x published theory. Using our extracted fine structure we can calculate the corresponding ensemble absorption spectra. Fig. 3-9 shows that convolving our extracted fine structure single NC absorption spectrum for R=1.5nm NCs with the inhomogeneous broadening implied by the T=5K emission spectrum, we are unable to adequately account for the ensemble absorption spectrum. In summary, within the fine structure model the temperature dependence of the Stokes shift allows a sensitive determination of the energy levels and oscillator strengths, but these values do not agree with the theoretically expected values or our measured absorption spectra. We now consider the same data from a different perspective.

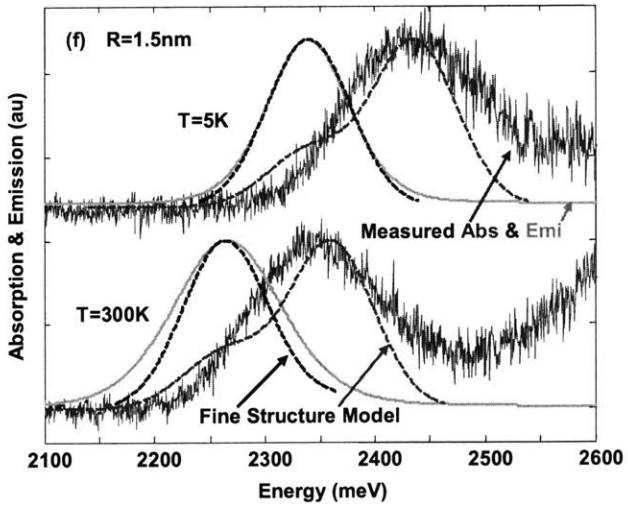

Figure 3-9: We fit the T=5K emission spectrum to a Gaussian to infer the inhomogeneous broadening for R=1.5nm NCs. We use this to calculate the corresponding absorption spectra (T=5K, T=300K) and emission spectrum (T=300K) using our extracted fine structure.

The temperature independent polaron shift that results from the exciton-acoustic phonon interaction offers an alternative explanation. In [38] the acoustic phonon interaction is calculated to first order in perturbation theory, so that the difference in the phonon Hamiltonians ("independent boson model") for the final and initial states is given by $\hat{H}_f - \hat{H}_i = \hbar\Omega_{fi} + \sum_\alpha A_\alpha\left(\hat{a}_\alpha^+ + \hat{a}_\alpha\right)$, where $\hbar\Omega_{fi}$ is the excitonic energy after excitation, $\hat{a}^+$ and $\hat{a}$ are phonon creation and annihilation operators, and the summation is over all phonon modes. (The solutions when all of the phonon modes have the same energy has an analytical form consisting of a series of delta functions [37], and has been used to model the optical phonon replicas in CdSe NC emission spectra [24, 50]. Within this model, the emission and absorption spectra are mirror images about the ZPL [37].) In [38] the spectrum of acoustic vibration modes for a NC embedded in a glass SiO_2 matrix is calculated and the lineshape of the phonon broadening is approximated as Gaussian. The calculated spectra physically corresponds to acoustic phonon assisted optical transitions, however there is also a narrow ZPL corresponding to optical transitions not requiring phonons that is offset from the acoustic phonon band by the lattice relaxation energy (polaron shift). In [38], the polaron shift (Δ_{ac}) is not explicitly calculated, but can be inferred from the linewidth (δ_{ac}) simulations. [Although refs. [27, 38, 46] all consider exciton-acoustic phonon scattering in similar frameworks, it is difficult to extract the relevant information from the simulations of any one paper. According to [38] the temperature dependence of the acoustic phonon pedestal is given by $\sigma_a(\Omega) = \exp\left[-\frac{(\Omega-\Omega_{fi}-\Delta_{ac})^2}{2\delta_{ac}^2}\right]$ where $\delta_{ac}^2 = \sum_\alpha \frac{A_\alpha^2}{\hbar^2}\coth\frac{\hbar\omega_\alpha}{2k_BT}$ and $\Delta_{ac} = \sum_\alpha \frac{A_\alpha^2}{\hbar^2\omega_\alpha}$. Since $\delta_{ac}^2(T=0) = \sum_\alpha \frac{A_\alpha^2}{\hbar^2}$ scales like $1/R^2$ [27] and values for R=1.1nm and R=6nm are given in the simulation results in ref [38], the values at intermediate sizes can be estimated. Using the simulation results for δ_{ac}(T=300K) and making an approximation $\delta_{ac}^2 = \frac{A_i^2}{\hbar^2}\coth\frac{\hbar\omega_i}{2k_BT}$, allows one to infer ω_α for all CdSe NC sizes and hence $\Delta_{ac}=\delta_{ac}/\omega_\alpha$ for all NC sizes. Our approximation accurately reproduces the simulations of the temperature dependence of R=1.1nm and R=6nm NCs in [38], and demonstrates that this is reasonable.] Since spectral hole burning experiments indicate that most of the oscillator strength is in the acoustic phonon pedestal, and PL and absorption spectra are mirror images of one another about the ZPL, there is a Stokes shift equal to approximately twice the polaron shift. Figure 3-7 shows that the acoustic phonon scattering theory without any fitting parameters agrees

reasonably well with our measured Stokes shift in terms of both size and temperature dependence. Since the Stokes shift can not definitively say which theory is correct, we next look at the temperature dependence of the ensemble linewidth.

3.4 Analysis – Temperature Dependence of the Linewidth

Existing theory attributes the temperature dependence of the spectral linewidth to homogeneous broadening due to exciton-acoustic phonon scattering [27, 28]. This effect is expected to scale approximately as $1/R^2$ and as T [27]. Figure 3-10 shows the predicted temperature dependence of the ensemble linewidth using the same single NC model that is used to calculate the Stokes shift, but convolved with a Gaussian size distribution that is chosen to fit our experimental linewidth at low temperature. The agreement with experiment is adequate in terms of size dependence and the magnitude of the spectral broadening. Furthermore, the exciton-acoustic phonon scattering model predicts that both the absorption and emission linewidths will broaden by the same amount. Our raw data are consistent with this prediction, as is clear from the large NC spectra in Fig. 3-4. However, there is too much noise in our data to allow for a quantitative measure of the absorption broadening. We conclude that the exciton-acoustic phonon scattering model can reasonably explain both the Stokes shift and spectral linewidth broadening. However, the fine structure theory also predicts that the ensemble emission linewidth will increase with temperature.

In figure 3-10 we have plotted the calculated broadening using the fine structure that was inferred from the temperature dependence of the Stokes shift. The broadening is not strong enough to explain our measured ensemble emission broadening. Additionally, the fine structure theory can not explain the broadening of the absorption features. (Optical phonon replicas are expected to cause a small but insignificant temperature dependence to the spectral linewidth.) We therefore conclude that the fine structure does not provide a full description of the relevant NC physics and that exciton-acoustic phonon scattering is necessary in any comprehensive physical model in order to account for spectral broadening.

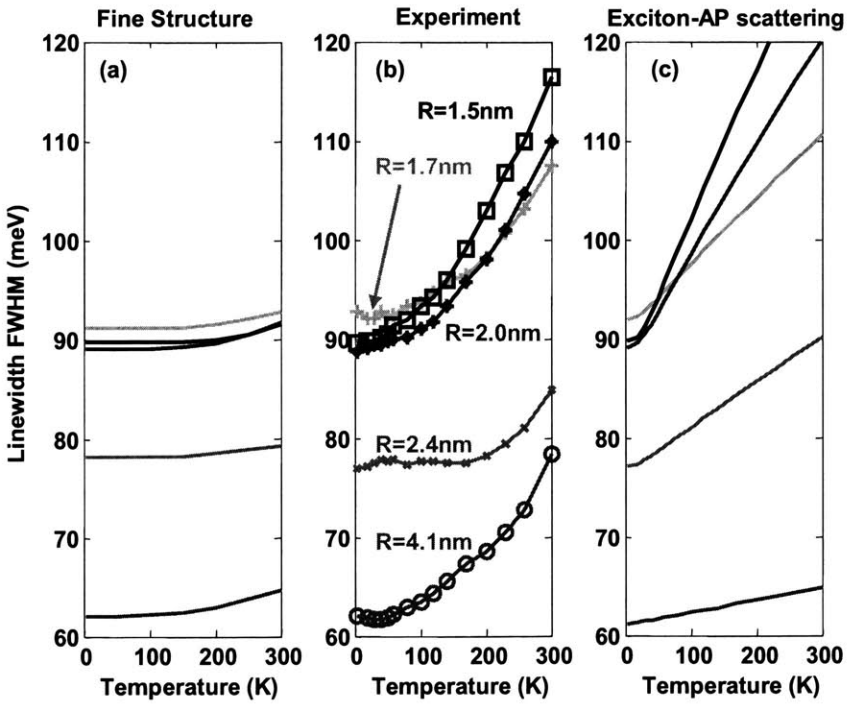

Figure 3-10: Left – calculated temperature dependence of an inhomogeneously broadened ensemble linewidth assuming the fine structure used to calculate the dashed Stokes shift in figure 4. The inhomogeneous broadening is assumed to be Gaussian whose width is choosen to fit the data at T=5K. Center – Repeat of linewidth data. Right – Predicted temperature dependence of the linewidth using exciton-acoustic phonon scattering model.

However, our single NC experimental data is inconsistent with predictions of the exciton-acoustic phonon scattering model. The theory that we have used predicts a broad acoustic phonon pedestal (~35meV FWHM) for our smallest NC sample at T=5K. However, the narrow linewidth (~12meV FWHM) of a single NC shows that this can not possibly be the case. While the single NC spectra is not necessarily indicative of the homogeneous linewidth, since spectral diffusion causes the spectra of the NC to shift during the integration time of the spectrometer, it does set a strict upper bound of 12meV on the homogeneous linewidth at T=5K. We therefore conclude that the exciton-acoustic phonon coupling model can not provide a full description of the NC physics necessary to explain the optical properties.

3.5 Discussion

Neither the fine structure theory nor the acoustic phonon scattering theory can adequately explain all of the experimental results. As has been pointed out in the literature, the independent boson

model for exciton-acoustic phonon scattering only takes one excited exciton state into account, neglecting higher energy exciton states [36, 51]. However, the effects of other excited states become important as the thermal energy k_BT approaches the relevant energy level spacing [51]. The fine structure theory and experiments suggest that the spacing between the 'dark exciton' and the next highest level can be as small as a few meV, and therefore the exciton-acoustic phonon scattering model should break down at low temperatures. A complete physical model that includes both the fine structure and acoustic phonon coupling is expected to yield complex results, as [52] indicates.

It is interesting to speculate how the NC spectra may be modeled phenomenalogically. The temperature dependence of the emission lifetime along with the "hook" in our PL spectra seems to strongly confirm the existence of a dark exciton and a lower excitonic level. However, the only experimental evidence of an upper exciton level that we are aware of comes from PLE experiments in [24]. These PLE experiments infer a single NC absorption spectrum that has a "Prussian helmet" shape, (see figure 7 in [24]) however in [24] the two peaks in the Prussian helmet were interpreted as discrete fine structure energy levels. We speculate that this "Prussian helmet" may in fact correspond to the ZPL and acoustic phonon pedestal due to exciton-acoustic phonon scattering. It seems that any model must incorporate a dark exciton that has a narrow spectrum and a higher exciton level that is broadened by exciton-acoustic phonon scattering, since these seem to be well established experimentally.

3.6 Room Temperature Spectral Linewidth

The room temperature single NC intrinsic linewidth is an important parameter in determining the "fundamental" potential for many NC applications. Even without a complete understanding of the physical mechanisms responsible for the temperature dependence of the linewidth, the room temperature intrinsic linewidth can be inferred from our experimental data. We consider the effect of spectral diffusion on the temperature dependence of the ensemble linewidth. We review the literature on spectral diffusion and conclude that its effects on the temperature dependence of the linewidth are minimal.

3.6.1 Data Analysis

Our results show that the ensemble linewidth increases with temperature. (see Figure 3-10)

While the inhomogeneous size distribution is believed to be responsible for most of the ensemble linewidth, we attribute the temperature dependence of the linewidth to the temperature dependence of the single NC intrinsic linewidth. To infer the room temperature intrinsic linewidth, we assume that the PL spectrum at T=5K is due to inhomogeneous broadening, that this contribution to the linewidth is independent of temperature, and that all of the temperature-dependent broadening is due to homogeneous broadening. We then do a least squares curve fit to the T=300K PL spectrum by convolving the T=5K PL spectrum with both a Gaussian and Lorentzian with variable width and center. The results are shown in figure 3-11. For small NCs, the inferred linewidth decreases with size before increasing for our largest NCs.

To compare our data with the exciton-phonon scattering theory, we define the homogeneous linewidth as $\Gamma^2_{homo}(T) = \Gamma^2_0 + \Gamma^2_T(T)$, and plot $\Gamma_T(300)$ on Figure 3-11, not the homogeneous linewidth. This is what we would infer using our deconvolution procedure if we had Gaussian inhomogeneous broadening and Gaussian homogeneous broadening. Exciton-acoustic phonon scattering is expected to dominate for small NCs and the acoustic phonon pedestal is expected to have a Gaussian spectrum [38]. The exciton-acoustic phonon scattering theory shows quite reasonable agreement with our experimental data for the smaller NCs, both in magnitude and size dependence. However, the effects of acoustic phonon scattering clearly can't explain the largest NC sample. We believe this is because optical phonon scattering becomes the dominant broadening mechanism for larger NCs.

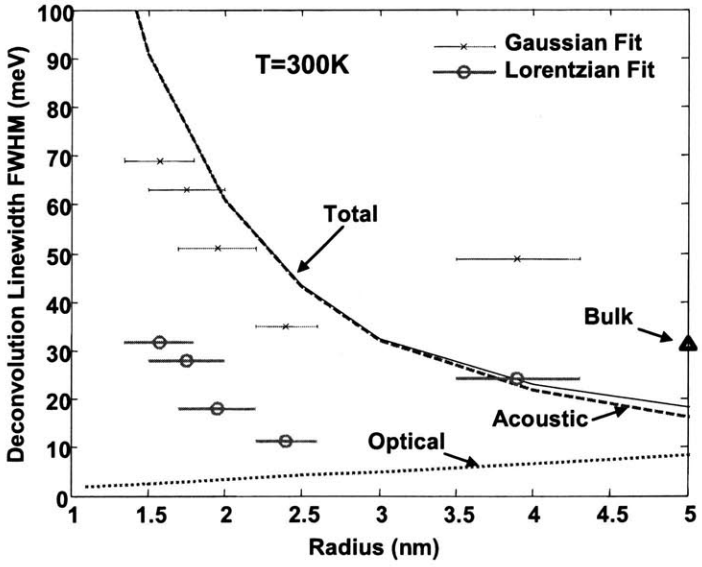

Figure 3-11: Experimentally deconvolved linewidth assuming Gaussian (x) and Lorentzian (o) homogeneous spectra. Dash – temperature dependent linewidth Γ_T for acoustic phonons (defined in text). Dotted – optical phonon broadening calculated in [38].

In bulk CdSe, the exciton linewidth is almost entirely due to optical phonon scattering, where the scattering is one phonon scattering between different excitonic states (mostly higher energy continuum states) [53]. In [54] the excitonic absorption linewidth in bulk is measured and fit to $\Gamma=\Gamma_0+BN$ with a Lorentzian lineshape, where N is the phonon occupation number. Assuming $\hbar\omega$=26meV for optical phonons, reference [54] finds that B=53±3 meV. This result has been misquoted multiple times, because [54] refers to the "half-width" of the exciton absorption. Other researchers including myself interpreted this to mean HWHM, but looking at the actual data that is included in the paper indicates that they mean FWHM. Since there are many other numbers quoted in the literature (B up to 200meV), we think that it is worth double checking the linewidth by considering an experiment by Cardona. In [55] the dielectric function of bulk CdSe is measured using spectral ellipsometry. Fixing the optical phonon energy at $\hbar\omega$=26meV, they find that for the lowest energy exciton, B=46±2 meV (FWHM) for the imaginary part of the dielectric function ε_2. Using Kramers-Kronig relations and their value for ε_1 we estimate that this underestimates the excitonic absorption linewidth by about 5%, so this ends up being in agreement with [54]. We believe that the data in [54] and [55] is the most reliable, and plot this bulk linewidth value in Fig. 3-11. (See matlab code in appendix for details.)

In a NC, the physics of optical phonon scattering is expected to differ from bulk, since the electronic states may not be separated by 26meV and hence there may not be a 1 phonon transition between exciton states. In NCs, the dominant optical phonon scattering mechanism is expected to be second order virtual transitions (simultaneous absorption and reemission of phonons) with no change in the electronic state. This effect has been estimated in [38] and is expected to scale like 1/R with size and $\sqrt{(n(n+1))}$ with temperature. In fact, measurements in substrate grown CdSe based dots show that B=23meV [56], consistent with the prediction of reduced coupling. However, it has also been observed that the strength of optical phonon scattering is sensitive to the shape of the electron and hole wavefunctions [57], and even observed to be enhanced by up to 5 times in GaAs/AlAs superlattices compared to bulk.

Our interpretation of the data is that for small NCs, acoustic phonon broadening dominates and the Gaussian fit is appropriate, while for large NCs optical phonon broadening dominates and the Lorentzian fit is more appropriate. Importantly, our experiment indicates that optical phonon scattering is reduced in CdSe NCs compared to bulk. This result is consistent with measurements in epitaxial CdSe QDs [56] and colloidal CdSe NCs [58]. We have treated the inhomogeneous broadening due to spectral diffusion as independent of temperature. In the next subsection we will discuss in detail why we believe this is appropriate.

3.6.2 Range of Spectral Diffusion

Measurements of single NCs show that their spectra change with time. This effect is referred to as spectral diffusion, and is believed to be caused by fluctuating local electric fields caused by charges moving in the matrix surrounding a NC. A direct result of spectral diffusion is that the longer the integration time of the spectrometer, the broader the measured linewidth will be. Spectral diffusion contributes to inhomogeneous broadening of our ensemble spectra. This subsection considers the possibility that spectral diffusion affects the temperature dependence of an ensemble linewidth.

While it has been shown that the rate of spectral diffusion increases with temperature [59], less attention has been focused on the temperature dependence of the range of spectral diffusion. The range of spectral diffusion refers to the linewidth that would be measured as the integration time of the spectrometer approaches infinity. The range of spectral diffusion must be smaller than the measured ensemble spectra, but clearly contributes to the inhomogeneous broadening of our ensemble spectra. Our ensemble measurements have no way of distinguishing homogeneous broadening from broadening due to a change in the range of spectral diffusion. In our analysis we have assumed that the range of spectral diffusion is independent of temperature, but it is possible that this is not the case. For example, any temperature dependence in the number of charges in the environment or the distance between occupied trap states and a NC will result in a temperature dependence of the range of spectral diffusion. We argue that experimental evidence indicates that the temperature dependence of the range of spectral diffusion is small compared to the measured temperature dependence of the ensemble linewidth.

First, experiments indicate that individual NCs on average have a large permanent dipole moment. This is commonly attributed to local electric fields inducing a polarization. In [60], the dipole moment of NCs is measured using dielectric dispersion measurements of NC ensembles between a parallel plate capacitor. Their measurements of the average dipole moment over a temperature range of about 80K near room temperature show that the dipole moment is independent of temperature. They calculate that the measured dipole moment of NCs could be explained if there is 1 charge on the surface of the NCs. The magnitude of the measured dipole moment is quite similar to measurements of single NCs at low temperatures in [61]. In [59] it is shown that the dipole moment is reduced for ZnS capped NCs, which means that any effect should be reduced in capped NCs. Furthermore, it has also been shown that the rate of spectral diffusion is reduced when a cap is added [59], which is consistent with the idea that the cap reduces the local E-field by keeping charges further from the core and screening the charge since

the cap is a dielectric. These experiments together indicate that the range of spectral diffusion is independent of temperature.

Secondly, experiments on individual CdSe NCs capped with elongated CdS shells show that "the spectral range of 30+/-10 meV over which peak shifts occur is virtually independent of temperature." [62] These experiments indicate that the change in the range of spectral diffusion between T=5K and T=300K is less than 10meV. Figure 3-10 shows that this is significantly smaller than the inferred homogeneous broadening.

Thirdly, within the model of spectral diffusion proposed above, if the fluctuations of the local electric field increased with temperature (because there are more charges or they get closer to the NC) then we would expect to see a larger average E-field. This larger average E-field would cause a larger average Stark shift, and hence we would expect to see a difference in dE/dT between bulk CdSe and the NCs. As Chapter 2 shows, this is not the case. Given the experimental evidence discussed above, we conclude that the range of spectral diffusion is independent of temperature with an uncertainty of 10meV from T=5K to T=300K, and therefore that our inferred homogeneous broadenings are reasonable.

Finally, it is interesting to estimate the range of spectral diffusion and its contribution to the ensemble linewidth. Reference [61] presents single NC PL measurements with an applied electric field. Modeling the NCs using the quantum confined stark effect, they are able to infer both the average polarizabilities α and the average local electric field ε for 4 different sizes of NCs. Using this data we estimate the average spectral energy shift $\Delta E = \frac{\alpha}{2}\varepsilon^2$. Although this data can not be used to definitively measure the range of spectral diffusion, we believe that it is reasonable to expect that the range of spectral diffusion is in the range of ΔE to $2\Delta E$. Figure 3-12 shows that the calculated values of $2\Delta E$ are quite similar for all 4 sizes of NCs. The shaded region shows the estimated range of spectral diffusion.

Figure 3-12 also shows our inferred homogeneous linewidth at room temperature and our measured ensemble linewidths. Assuming Gaussian spectra and that the ensemble linewidth $\sigma_{ensemble}$ is result of the homogeneous linewidth σ_{homo}, range of spectral diffusion σ_{SD}=10 nm, and size inhomogeneities σ_{size}, we can infer the broadening due to the size distribution $\sigma_{size}^2 = \sigma_{ensemble}^2 - \sigma_{homo}^2 - \sigma_{SD}^2$.

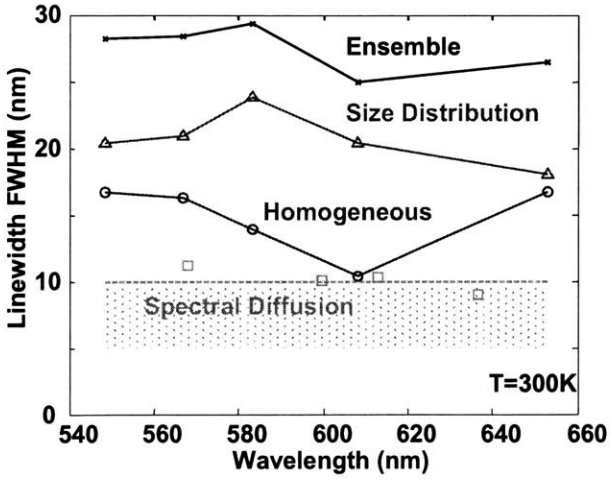

Figure 3-12: Shaded area shows our estimated range of spectral diffusion. Using our inferred homogeneous linewidths and measured ensemble linewidths at T=300K, we can infer the broadening due to our ensemble size distribution.

Our analysis indicates that even if the even if the size distribution can be narrowed and the effects of spectral diffusion can be eliminated, the ensemble linewidth at room temperature would be limited to about 50% of its surrent value by the homogeneous linewidth. This sets "fundamental" limits on what is possible for many potential NC applications.

3.7 Stokes Shift Contribution of Inhomogeneous Broadening

This section presents our simulations of the contributions to the Stokes shift due to inhomogeneous broadening. Since NC absorption cross sections scale as R^3 [3] away from the bandedge, large NCs preferentially absorb UV excitation resulting in a red shift of the ensemble PL spectrum. However, since the oscillator strength of the first absorption feature scales as R [33], the first absorption feature is also red shifted and partially cancels the first effect. The net effect is that an inhomogeneous size distribution contributes to the Stokes shift. Quantifying this effect is more subtle than it may appear on the surface.

The first step is to specify the relationship between the NC radius, R, and the NC energy, E. Figure 3-13 shows the relationship that we use in our simulations E(R). It is based on the implied bandedge absorption peak at T=10K in [24]. Secondly, the size distribution of the NC ensemble s(R) must be specified, where s(R) is the PDF (probability distribution function) of a randomly chosen NC having a particular radius. Multiplying the size distribution s(R) by R^3 and

renormalizing gives the PDF of a particular size of NC being excited by UV excitation and emitting a photon, $P_{emi}(R)$. The ensemble emission energy is then calculated by averaging the product of $P_{emi}(R)$ and E(R) over R, $E_{emi}=<E(R)\times P_{emi}(R)>$. The result is that the average ensemble emission energy is redshifted compared to the emission energy of a NC with an average ensemble radius. This happens because larger NCs are preferentially excited. Similarly, the bandedge absorption feature is also redshifted because of the inhomogeneous size distribution. Since the oscillator strength of the bandedge absorption feature scales as R [33], the PDF of a photon from a white light source being absorbed by a NC with radius R is given by s(R) multiplied by R and renormalized, $P_{abs}(R)$. The average absorption energy is then calculated by averaging the product of $P_{abs}(R)$ and E(R) over R, $E_{abs}=<E(R)\times P_{abs}(R)>$. This analysis allows us to quantify the contribution of an inhomogeneous size distribution to the Stokes shift.

Figure 3-14 shows that a $\sigma_R/R=5.5\%$ Gaussian size distribution contributes a maximum of about 7meV to the Stokes shift. This is the approximate size distribution for our smallest NCs, assuming that the low temperature PL spectrum is entirely due to the inhomogeneous size distribution. Our largest NC ensembles have an implied size distribution of approximately 10%. Since the contribution to the Stokes shift from inhomogeneous broadening scales like $(\sigma_R/R)^2$, the inhomogeneous contribution is approximately 4meV for our largest samples. We conclude that the contribution of an inhomogeneous size distribution to the Stokes shift is small.

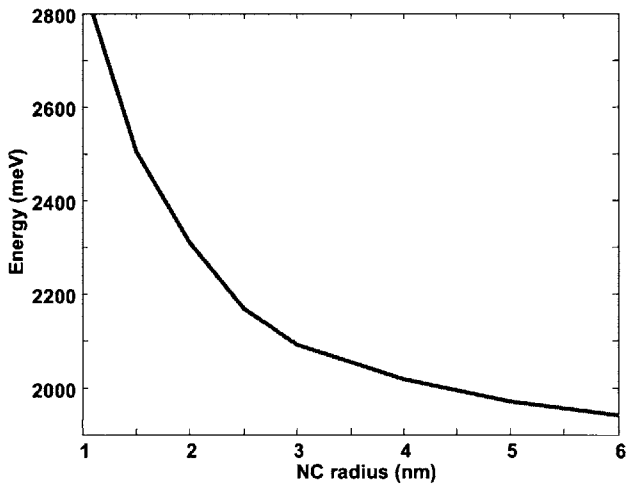

Figure 3-13: Approximate bandedge absorption energy at T=10K for CdSe NCs from [24].

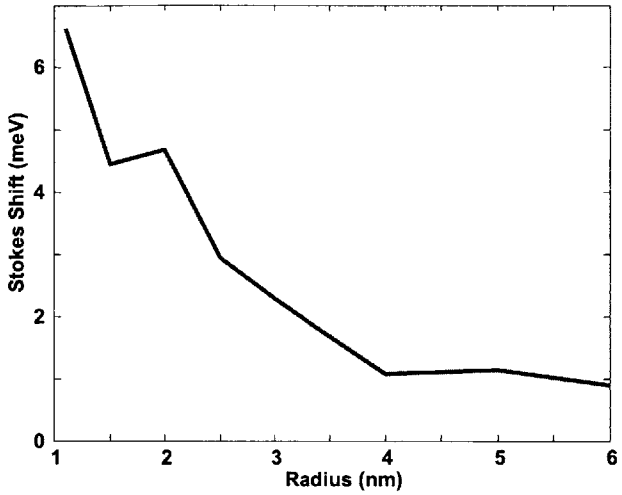

Figure 3-14: Calculated contribution to the Stokes shift assuming a Gaussian σ_R/R=5.5% size distribution.

3.8 Conclusion

In the literature, both exciton fine structure and exciton-acoustic phonon scattering models have been used to explain a wide variety of experiments in CdSe NCs. However, our careful measurements of the temperature dependence of the ensemble emission and absorption spectra, along with the single NC spectrum, can not be adequately explained by either theory in isolation. Using the acoustic phonon scattering model developed in [38], we are able to explain both the magnitude and size dependence of our measured Stokes shift and the ensemble linewidth temperature broadening, but not our experimentally measured single NC PL spectra. On the other hand, the parameters in the fine structure theory can be adjusted to adequately fit the temperature dependence of the Stokes shift, but the implied fine structure can not explain the spectral broadening of the emission linewidth or the broadening of the absorption linewidth. We believe that the existence of a 'dark exciton' with a narrow emission spectrum and a higher energy exciton state whose absorption is broadened by exciton-acoustic phonon scattering have been well established experimentally. We hope that this work provides the motivation to reassess the physics that has previously been used to explain experimental results.

Finally, we have estimated the contributions of the size distribution, spectral diffusion, and homogeneous linewidth to the ensemble PL linewidths for our samples. Our analysis indicates that even if the inhomogeneous broadening due to size distribution and spectral

diffusion could be eliminated, the room temperature homogeneous broadening will only allow the ensemble linewidth to be reduced to approximately half of the current value. The room temperature ensemble linewidth is an important parameter for many potential NC applications, especially NC microbead barcodes. The next chapter will analyze the potential of NC based microbeads for high throughput biological screening.

Chapter 4

Design of fluorescence microbead barcodes for high throughput screening

In previous chapters, we examined the physical processes that determine the optical properties of semiconductor nanocrystals. We inferred the room temperature intrinsic linewidth of CdSe nanocrystals, a parameter that puts "fundamental" constraints on many nanocrystal applications including microbead barcodes. After reviewing biological assays and the state of the art in microbead screening, we consider the design of nanocrystal based microbead barcode technology for use in high throughput biological screening.

4.1 Introduction

A recurring desire in many areas of biological research is screening for the presence of many predefined target biomolecules in large numbers of test samples in a rapid and economic manner. In Section 4.2, we review two dominant techniques for performing biological assays - planar array and microbead based technologies. In the microbead technology, different types of polymer microspheres are distinguished from one another by varying the amount of two dyes incorporated into the microbead. Currently 100 types of microbead are distinguishable using traditional dyes, but the literature suggests that using nanocrystals (NCs) instead of traditional dyes could dramatically increase the number of distinguishable microbead types. It has been speculated that between 10,000 and 40,000 distinguishable barcodes may be realized [31], with some guessing an upper limit closer to 1 million. Even increasing the number of distinguishable barcode types to around 1000 is important, since this would allow a single experiment to screen for every type of human microRNA, which are estimated to number at least 800 [63].

Although the benefits of replacing dyes with nanocrystals (NCs) has been anticipated, there are still very basic questions regarding how a NC based microbead barcode system should be designed that have not yet been addressed. Should the optical detection system use filters and

highly sensitive photomultiplier tubes or a spectrometer? How should information bits be encoded as fluorescence signals – what kind of code? How should the fluorescence signature be optimally decoded? How many distinguishable barcodes are possible for a given error rate? This chapter provides some quantitative analysis to help answer these questions.

Specifically, we look at the problem of NC based microbead barcodes through the lens of information and coding theory. Information theory has been widely applied to the analysis of biomolecular structure and sequence information [64-66]. Recently, applications have included using error control coding analysis as a tool in sequence analysis [64, 65] as well as string barcoding as a tool for developing minimal assays for sequence identification [67]. These are examples of channel coding, a field that is concerned with making the storage or transmission of information more robust to disturbances that can cause errors. Code design involves the construction of a collection of codewords (the code) where the individual codewords can be distinguished with minimal error. Once a channel has been specified, a code can be designed to appropriately trade off the size of the code with the chance of error. In this chapter, the utility of code design to molecular biology is demonstrated with the example of microbead based high-throughput assays.

In Section 4.3, we review what is currently achievable with NC doped polymer microbeads and develop a simple noise model based on what has been achieved experimentally. Section 4.4 discusses the similarities and differences between this problem and traditional communications problems. In section 4.5 we investigate multiple regular coding architectures, while we consider a Monte Carlo code generation technique in section 4.6. Section 4.7 presents a sensitivity analysis of our model. Before investigating the prospects of NC-based barcodes, it is appropriate to first review the current biological assay technologies.

4.2 Current Biological Multiplex Assay Technologies

This section reviews the two dominant biological assay technologies – DNA planar arrays and microbead based assays. Specifically, we discuss the specifications that are currently commercially available for microbead assays.

4.2.1 DNA Planar Array

A familiar solution to screening for gene expression in human cells is the DNA planar array. This

technology uses a planar array of 40,000 wells each containing sDNA' (single stranded DNA) that is complementary to the sDNA of a different human gene. After fluorescently labeling all of the sDNA strands in the sample of interest, the sample is flowed over the planar array. In biology, it is well known that an sDNA strand will bind to its complement sDNA'. (see figure 4-1) Therefore, if a particular gene is present in the sample, then the corresponding well in the planar array will accumulate sDNA. This is detected by illuminating the planar array with UV excitation and imaging the fluorescence. Since only wells that have accumulated sDNA will fluoresce, and the correspondence between well location and gene type is known, the expression of all 40,000 genes in the human genome can be inferred. Figure 4-2 summarizes the process. Figure 4-3 shows a picture of the fluorescence from a DNA planar array.

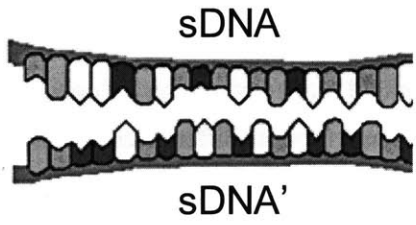

Figure 4-1: Schematic of a DNA molecule. A single strand of sDNA binds to its complementary sDNA' to form a DNA molecule.

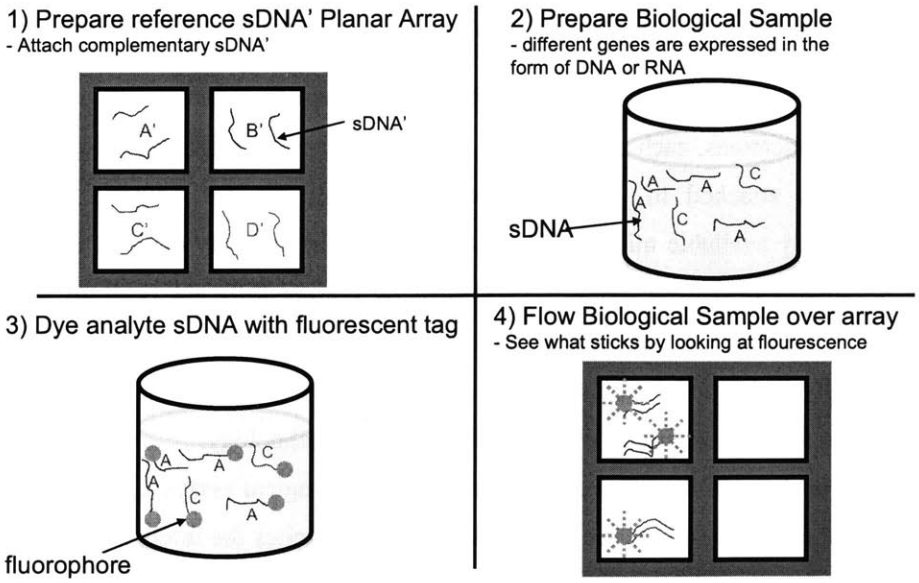

Figure 4-2: Schematic of traditional DNA planar array technology.

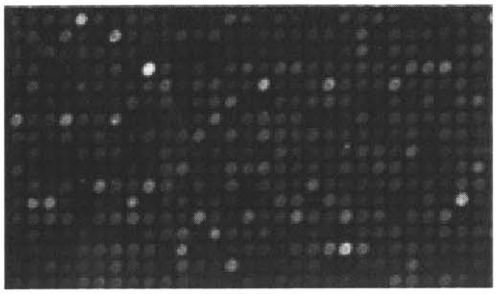

Figure 4-3: Picture of fluorescence from a DNA planar array. Fluorescence indicates that a particular gene has been expressed.

Biological screening applications can differ in the types of target biomolecules, the number of target biomolecules (degree of multiplexing), or the required experimental throughput. For example, a clinical setting might require screening for only a few types of antibodies in only a handful of samples per day. Because of these differences, alternative screening technologies such as microbead assays have been developed. The next section reviews the principle of operation behind microbead assays and discusses what is currently commercially available.

4.2.2 Microbead Assays

Optically encoded microbeads are used for multiplex assays in many areas of biology [31, 68-71]. In these applications, each biomolecular probe of interest (a single nucleotide polymorphism for example) is attached to the surface of a different type of encoded polymer microbead. Commercially available microbeads are encoded by the intensity of two fluorescent dyes within the microbead [72]. An assay is performed by mixing different types of microbeads with a sample, separating the microbeads, and using the fluorescence to both decode each microbead individually and to infer the amount of analyte that is attached to the surface of the microbead. Figure 4-4 shows a schematic of the microbead assay technology.

For some of the most common microbead biological assays, a flow cytometer is used to separate the microbeads, while a classification laser excites the internal dyes. The fluorescence intensity of the two dyes is measured using one colored glass filter and one photo-multiplier tube (PMT) for each dye. Figure 4-5 shows a schematic of how this separation and detection are performed. Commercial systems with 8 distinguishable bead types are specified to correctly decode greater than 80% of the time with an error rate less than 0.5% [72]. (The remaining

microbeads are ignored due to ambiguous fluorescence.) Systems with as many as 100 different microbead types are specified to have an error rate of less than 2% [72]. These error rates refer to decoding individual microbeads, but the effect of these errors can be reduced at the system level by simply removing the high and low outliers from the final statistics, since typically there are on the order of 100 microbeads of each type per experiment.

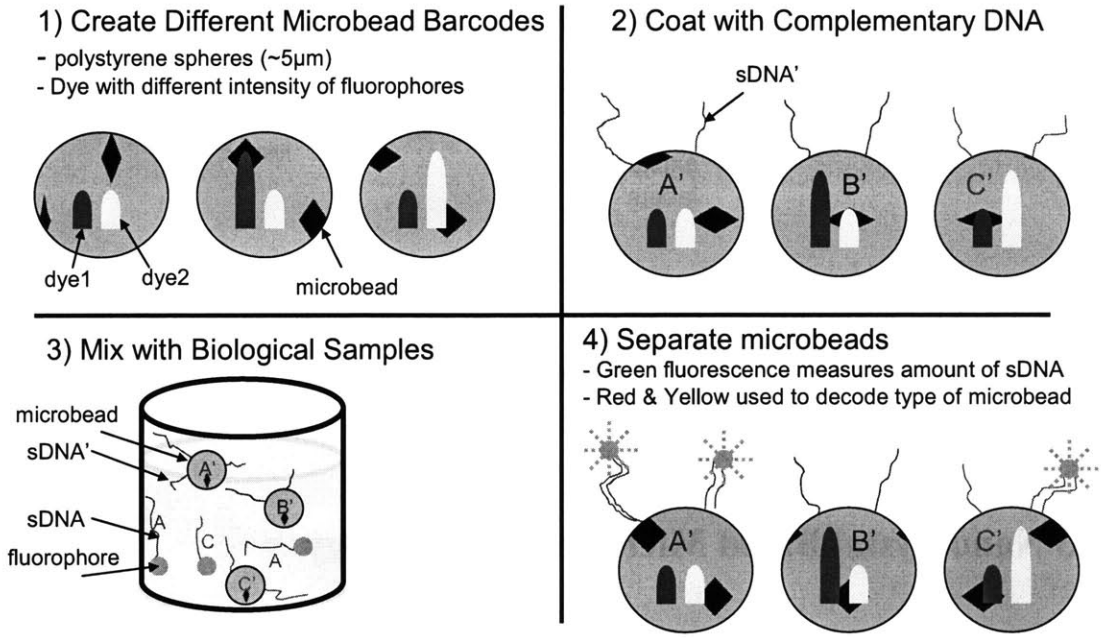

Figure 4-4: Schematic of microbead assay technology.

Particle analysis rates as high as 10,000/sec have been reported using flow cytometry, but 500/sec is more typical [73]. Relative to DNA planar arrays, microbead assays are considered less expensive, more flexible, and have a higher throughput, but have low multiplexing capabilities. With this in mind, it is interesting to consider if using NC based barcodes can improve the degree of multiplexing that is possible for microbead assays.

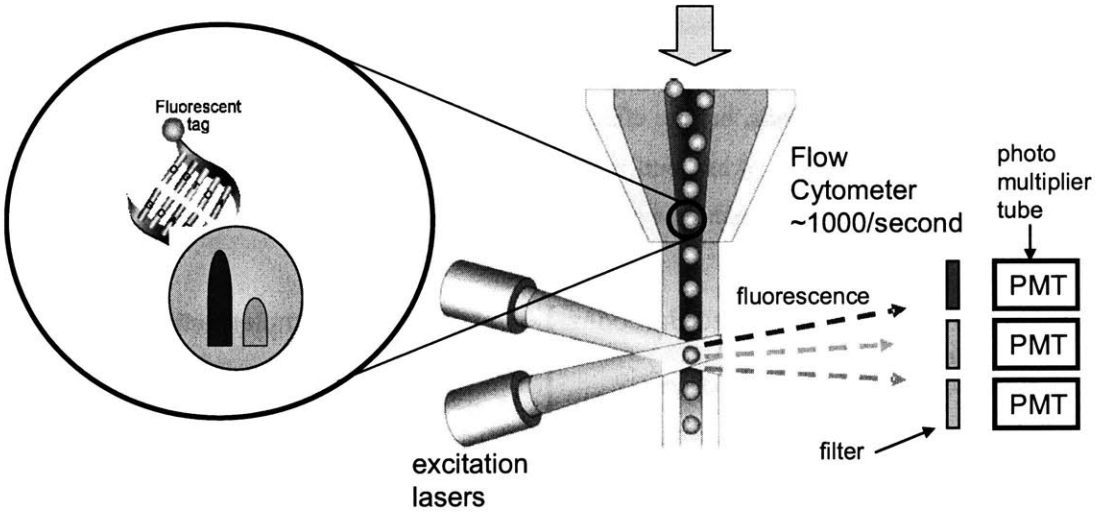

Figure 4-5: Schematic of detection system for traditional dye based microbeads. Red and yellow fluorescence are used to distinguish the type of microbead. Green fluorescence is used to measure the amount of biomolecule attached to the microbead.

4.3 Nanocrystal Based Microbead Technology

To analyze the potential of nanocrystal based microbead barcodes, we have created a simulation of what is experimentally reasonable using current technology. Specifically, we developed a Monte Carlo simulation of the expected noise sources in order to estimate the correct and error decode rates of different coding schemes. First, we had to make some educated choices about how a nanocrystal based microbead barcode system might be implemented.

4.3.1 System Implementation

While dye based microbead systems use colored glass filters and photomultiplier tubes for detection, as the number of colors used to label an individual microbead increases, fluorescence measurements with a spectrometer become a more practical solution. Figure 4-6 shows schematically what a system might look like. Assuming a spectrometer based system, we must choose an algorithm for how to decode a measured spectrum. Our algorithm first computes the mean-square-error (MSE) between the 'measured' noisy fluorescence spectrum and the expected fluorescence spectrum for all possible codewords, and then decodes by choosing the codeword

with the minimum MSE_1. However, no decision is made if the codeword with the second lowest MSE_2 has a similar MSE. In our simulations we have a relative error threshold β and if $MSE_1 > \beta * MSE_2$ then we choose not to decode. Our algorithm is similar to a correlation detector. Next we need to make a model of the expected noise given what can reasonably be achieved experimentally with NCs and microbeads.

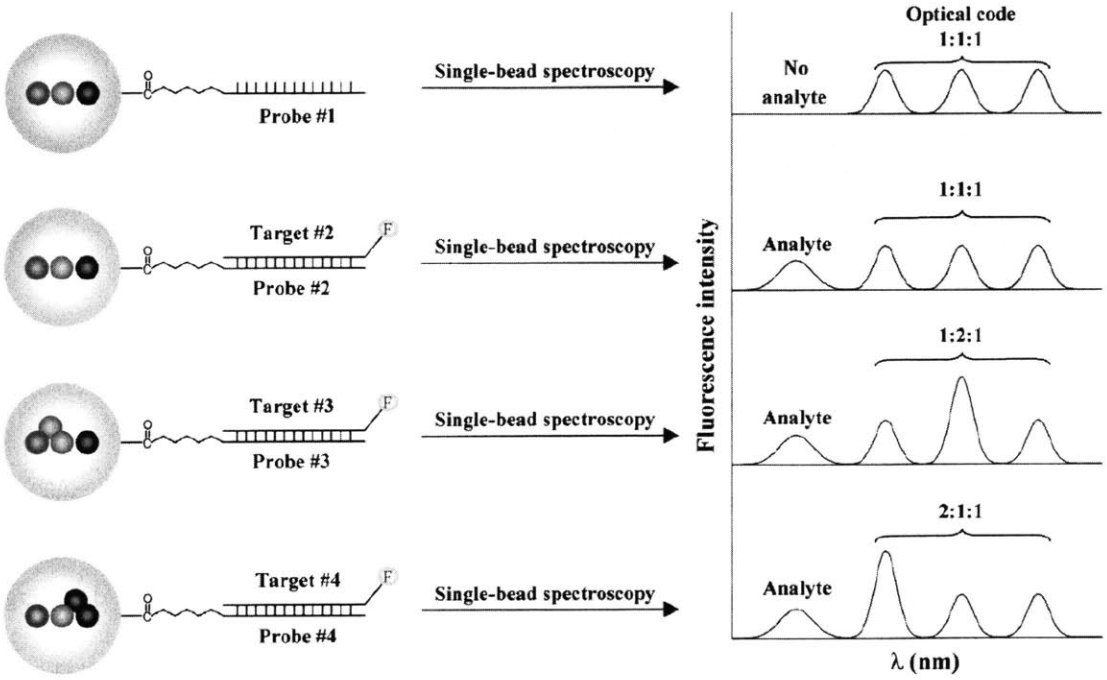

Figure 4-6: Schematic of NC based microbead assay technology from [31]. Different probe molecules are attached to different types of microbeads. The fluorescently labeled target molecules bind to their cooresponding probes. The spectrum of individual microbeads is used to both infer the type of probe molecule using the optical code and to measure the presence of the corresponding target analyte.

Since CdSe NCs are the most mature NC technology and have been studied most extensively, we will focus on them in this analysis. Incorporating NCs into polymer microbeads is a well established procedure. Figure 4-7 shows microbeads doped with different NC colors. In our simulations, we assume that the ensemble fluorescence spectra is Gaussian and has a linewidth of $\sigma_{linewidth}$=13nm ($\Delta\lambda$~30nm FWHM), although ensemble linewidths narrower than this are currently available for all colors of CdSe NCs [14]. Mathematically, we use $h(\lambda-\lambda_i)$ to denote the spectrum of a single color NC ensemble centered at λ_i. We assume that any color in the range λ_{blue}=530nm $< \lambda_i < \lambda_{red}$=650nm is readily available, even though a larger range has been demonstrated [32]. The full spectrum will be the superposition of many colors of NCs with

different amplitudes $S(\lambda) = \sum_i A_i h(\lambda - \lambda_i)$. We choose a spectrometer bin spacing of $\Delta\lambda$=5nm with a wavelength range from λ_{min}=450nm to λ_{max}=700nm for our simulations.

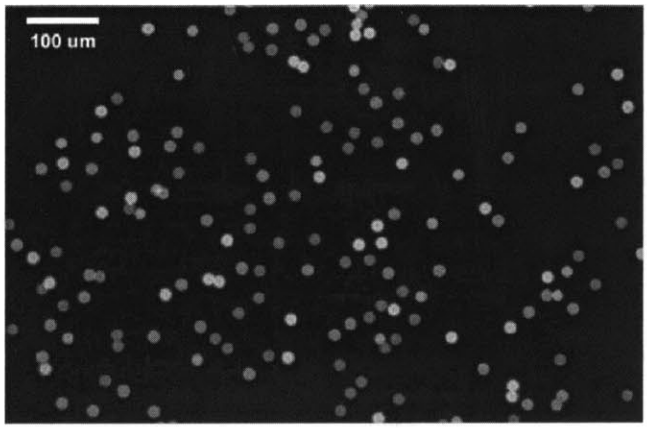

Figure 4-7: Picture of NC dyed microbeads from [74].

Although it may be possible to use the absolute intensity of the fluorescence spectra for microbead barcodes [31], a much more robust approach is to make decoding the barcodes independent of absolute intensity. Mathematically, we normalize the spectrum before decoding, so that $\int_{\lambda_{min}}^{\lambda_{max}} S(\lambda) d\lambda = 1$. This constraint not only makes the barcodes more robust to decoding – so that the coupling efficiency of the fluorescence to the detector does not matter – it also makes creating the barcodes potentially must easier, since controlling absolute intensities can be difficult [74]. (The fluorescence spectrum is the linear superposition of the emission from each color of NCs so long as there is minimal interaction between the NCs in terms of reabsorption of emitted light, or dipole-dipole coupling between NCs. Importantly, reference [74] does not observe any fluorescence quenching or spectral shift when NCs are incorporated into mesoporous polystyrene beads.)

4.3.2 System Noise Model

While there is no fundamental reason why NC ensemble samples can't be made with arbitrarily small uncertainty in NC color or linewidth, the cost and effort required to manufacture the NC

samples increase as the quality and control of the NC samples increase. We are interested in assessing what can be achieved given what is currently available commercially. Accordingly, we have ordered various NC samples from QDot Corp and find that the error in the center wavelength ε_{cen} versus what is expected has a standard deviation of σ_{cen}=2nm and a variation in fluorescence linewidth ε_{wid} that is about σ_{wid}=0.5nm. We believe that these uncertainties give a reasonable measure of the noise that can be expected when creating an individual instance of a barcode. The resulting spectrum will have the form $S(\lambda_i) = h\left(\frac{\lambda}{1+(\varepsilon_{wid}/\Gamma)} - \lambda_i + \varepsilon_{cen}\right)$, where Γ=13nm is the expected linewidth.

Incorporating NCs into mesoporous polymer microbeads has been established experimentally. The NCs reside in pores (~20nm) in the microbead [74]. Because the distribution of microbead pore sizes may vary from microbead to microbead, the relative dyeing efficiency for different colors of NCs will vary, since it is easier for larger NCs to fit into larger pores. We model this noise by multiplying the desired fluorescence spectra by a random slope ε_{amp} centered at $\lambda_{center} = \frac{\lambda_{red} + \lambda_{blue}}{2}$ and leaving $S(\lambda) = (1 + \varepsilon_{amp}(\lambda - \lambda_{center}))\sum_i A_i h\left(\frac{\lambda}{1+(\varepsilon_{wid}/\Gamma)} - \lambda_i + \varepsilon_{cen}\right)$.

Finally, we add a white Gaussian noise background $\varepsilon_{wn}(\lambda)$ to the fluorescence spectra to account for a variety of things – like environmental fluorophores, the detection sensitivity of the optical system, or photon shot noise. (All of the noise sources are modeled using zero mean Gaussian random variables.) The final noisy spectrum is given by $S(\lambda) = (1 + \varepsilon_{amp}(\lambda - \lambda_{center}))\sum_i A_i h\left(\frac{\lambda}{1+(\varepsilon_{wid}/\Gamma)} - \lambda_i + \varepsilon_{cen}\right) + \varepsilon_{wn}(\lambda)$. This spectrum S(λ) is then discretized into a vector of numbers S[n] corresponding to spectrometer bins, where $S[n] = \int_{\lambda_{min}+\Delta\lambda(n-1)}^{\lambda_{min}+\Delta\lambda(n)} S(\lambda)d\lambda$, and is normalized $\sum_n S[n] = 1$.

In order to calibrate the amplitude and background noise sources we compare our model to what has been achieved experimentally using the ratio of 2 colors of CdSe NCs separated by 70nm in wavelength [75]. Ref. [75] finds that the ratio of the amplitudes can be controlled to better than 2% accuracy and estimates that over 30 ratios could potentially be distinguished. We adjust the amplitude and background noise so that our model gives comparable results. Specifically, we generate a code based on the ratios of 2 colors separated by 70nm. We chose a

1:1 ratio of color#1 to color#2 as the first codeword in our code, and then generate many noisy instances with only the background and amplitude noise sources turned on. We then do a least squares curve fit to the amplitudes of two Gaussians with appropriate centers and linewidths. The distribution of the ratio of the amplitude fits is then calculated. The second codeword (ratio) is then chosen so that only 0.5% of the distribution is closer to the second ratio. (This effectively spaces the ratios by about six standard deviations of the distribution, which is what has been indicated in [75].) We continue this process until we reach zero.

Figure 4-8 shows the simulation results. As expected, we find that for small ratios, the background dominates the noise and hence it is best to space the ratios linearly, while for ratios close to 1, the amplitude noise is dominant and the best spacing is logarithmic. Fig. 4-8 only shows 17 ratios, all less than or equal to 1. Of course, for every ratio less than 1 (more of color #2 than color #1), there is a corresponding ratio greater than 1 (more color#1 than color#2). (For completeness, calibrated white noise in a spectrometer bin has a standard deviation of $\sigma_{wn}=0.001$ and $\sigma_{amp}=5\times10^{-4}nm^{-1}$.) Finally, the result of this analysis is that we now have a noise model that is grounded in what has been achieved experimentally.

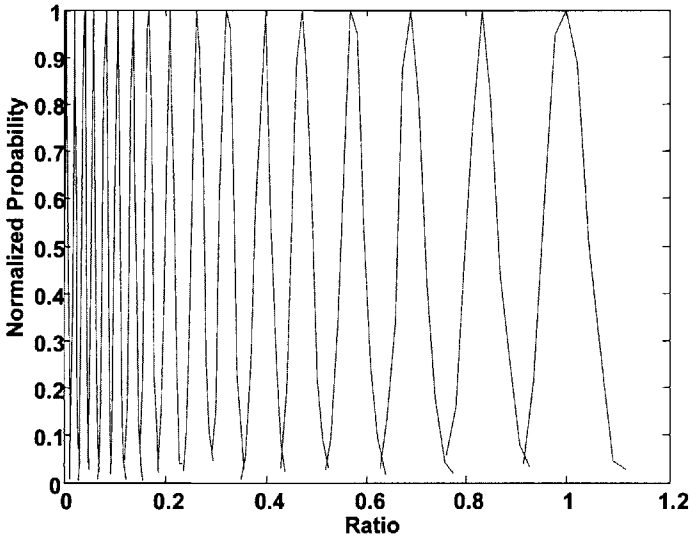

Figure 4-8: In order to calibrate the noise in our model to experiment, we simulate the ratio of 2 colors of NCs (with the center and linewidth errors turned off). Each peak is the result of a simulation for a particular ratio of NCs. The text explains in detail how the ratios were chosen.

At this point we have a fully specified mathematical problem, and we are left with the task of making an intelligent choice of how to design the barcodes to maximize the number of distinguishable codewords. Before continuing with barcode design, we will investigate this problem through the lens of information theory.

4.4 Information and Coding Theory

The microbead barcode system that we have specified in the previous section can be viewed as a noisy communications channel and can be analyzed with information theory, specifically the Shannon-Hartley Theorem. In this section we also examine the similarities and differences between a "typical" communications problem and microbead barcodes.

4.4.1 Shannon-Hartley Theorem

Shannon's channel capacity theorem sets a limit on the transmission rate of information C through a noisy communications channel with negligible chance of error as the length of a message becomes arbitrarily long. This is a relevant metric for most modern communications systems. Shannon's channel capacity in the time domain is $C = \int_0^{BW} \log_2\left(1+\frac{S(f)}{N(f)}\right)df$ where S(f) and N(f) are the signal and noise power spectral densities and BW is the channel bandwidth. There is a direct analogy between the usual the time domain version and our spectral domain problem that allows us to apply this theorem to microbead barcodes. One issue is that the signal and the noise are assumed to be independent in the Shannon-Hartley Theorem, which is not true for our problem. However, the background noise $\varepsilon_{wn}(\lambda)$ in our model is independent of the signal, and therefore we can still apply the Shannon-Hartley Theorem to our problem in order to set an upper bound on the information capacity of a microbead.

One possible analogy between the usual time domain and the optical spectral domain, is to imagine that the spectrometer range (λ_{min} to λ_{max}) corresponds to one second t=1s of signal. In this analogy, the spectrum of a single NC color corresponds to the impulse response h(t) of the channel. Then, the magnitude of the discrete Fourier transform of h(t) indicates the attenuation of sinusoids at 1 Hz intervals, and the square gives us samples of S(f) which we denote $S[k_i]$. N(f) is calculated by taking the average of the squared Fourier transform of many instances of $\varepsilon_{wn}[n]$. Figure 4-9 shows the power spectral densities, $S[k_i]$ and $N[k_i]$. The information capacity of a microbead is then calculated according to $C = \frac{\lambda_{red}-\lambda_{bluc}}{\lambda_{max}-\lambda_{min}} \sum_{k\neq 0_i} \log_2\left(1+\frac{S[k_i]}{N[k_i]}\right)$. The factor in front of the summation is due to the fact that we can not transmit for the whole t=1s, since we are

constrained by $\lambda_{blue} < \lambda_i < \lambda_{red}$. Also, S[0]/N[0] is not included because our normalization condition eliminates all the information stored in the DC offset. This analysis yields a capacity of C=42 bits/microbead. However, this metric is not especially useful for assessing microbead technology.

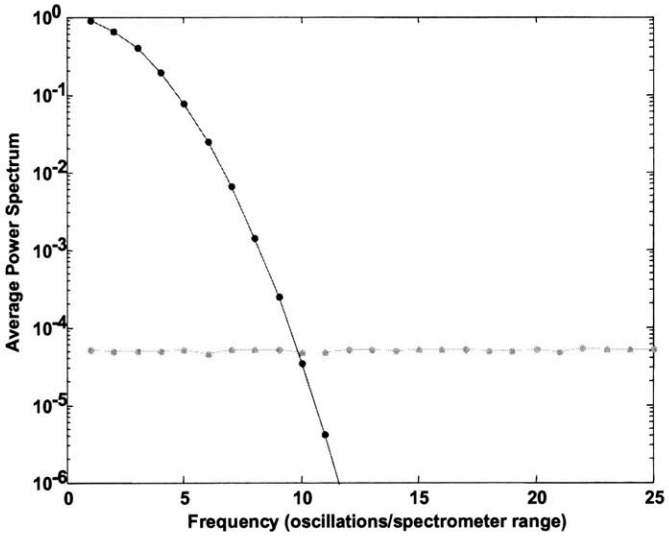

Figure 4-9: The plot shows the squared absolute magnitude of the Fourier transform of a single color NC optical spectrum and the background white noise.

First, the capacity C is not an upper bound on the number of codewords, since we allow a finite error rate. On the other hand, our system has other constraints that are not taken into account in our calculation, and will lower the microbead capacity – S[n] can not be negative, S[n] is normalized, and there are other signal dependent noise sources that we have neglected. Despite the difficulty of putting an upper bound on the code size, we can put a lower bound on the number of codewords by simulating different coding schemes to see what works the best. The main question is: How do we encode the information?

4.4.2 Channel Coding

Most of the analysis that has been done for traditional coding applications is not especially useful for our situation, but it is worth reviewing the basics in order to understand how our problem is different. A "normal" communications problem deals with the transmission of a large amount of information, typically assumes that signal and noise are independent, and assumes that there is no

ISI (inter symbol interference). A message is first converted into bits which are then physically encoded, for example as a plus or minus voltage. The receiver then makes a decision as to whether a 1 or 0 was sent by checking if the received voltage is above or below some threshold level. Channel coding deals with the problem of how to efficiently add redundant bits to a message in order to make the message more robust to decode errors, but not unnecessarily long. Hamming, Golay, Reed Solomon, and convolution codes all fall into this category of traditional binary codes. Because of channel noise, some of the received bits will be incorrect. As long as the number of errors is sufficiently small, the original message can be recovered by choosing the codeword that is closest to the received signal in the Hamming distance sense (minimum number of differences in bits).

In contrast to a "normal" communications problem, our microbead barcode application has a small amount of information per microbead (~10 bits) and is therefore in the short block length regime. Our signal and noise are not independent, so it is non-trivial to apply Shannon's theorem to set a strict upper bound on the number of distinguishable codewords. Finally, there is significant ISI if one chooses a PAM (pulse amplitude modulation) coding architecture, since the spectra of different colors massively overlap if more than approximately 5 colors are used.

For our application, the received signal is the measured light intensity in each spectrometer bin, or a vector of (700nm - 450nm)/5nm = 50 numbers. As explained previously, we decode by calculating the MSE between the received signal and the expected signal that corresponds to every codeword, and choose the codeword with the minimum MSE as long as there isn't a close second choice. For our application, decode complexity is not an issue since we will be dealing with a very small data rate (~10 bits/bead)*(~1000 beads/sec) = 10,000 bits/sec. Finally, we are ready to analyze the code design for microbead barcodes.

4.5 Regular Barcode Design

To begin our design analysis we consider pulse-amplitude-modulation (PAM) codes. First, we create a list of all valid PAM codewords for a given number of colors and number of intensity levels. Because we have assumed that our system will not be sensitive to absolute intensity we eliminate codewords that appear identical after normalization, like (132) and (264). Next, a random codeword is selected from the list (all codewords have equiprobability of being chosen) and a noisy instance of the fluorescence for that codeword is created according to the noise characteristics described above. Figure 4-10 shows an example of a noisy instance of the

spectrum corresponding to the codeword (20211), along with the non-noisy spectrum that was desired. The left most peak of the noisy spectrum is right shifted due to noise in the center wavelength, while the high frequency noise results from the background noise. Note that even with only 5 colors there is a lot of spectral overlap between colors. Figure 4-10 also shows a specific instance of an incorrect decode.

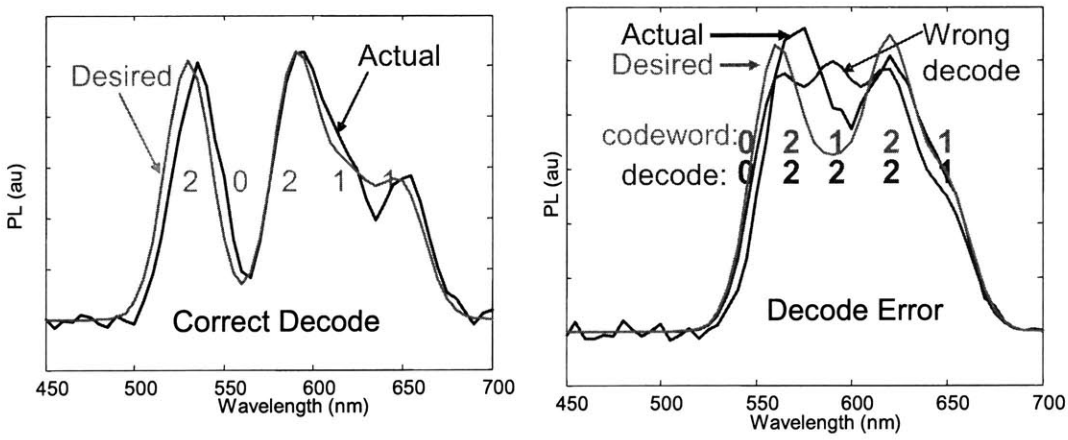

Figure 4-10: Specific instances of a correct decode and a decoding error.

To decode, we choose the codeword whose expected fluorescence spectrum has the lowest MSE with respect to the actual noisy fluorescence signal, unless $MSE_1 > \beta \times MSE_2$ in which case the spectrum is not decoded. The success rate and error rate are then calculated by repeating the simulation many times. We then optimize the choice of number of colors, number of intensity levels, and error threshold β in order to maximize the number of distinguishable codewords while maintaining a correct decode rate>80% and error rate<0.5%. Ideally we would like to have a large number of colors and a large number of intensity levels, since this would result in a large number of codewords. However, there is a trade-off. Fig. 4-11 shows that as the number of colors increases, the spectral overlap increases and it becomes more difficult to distinguish between intensity levels. This happens because increasing the number of colors while holding the spectral range fixed ($\lambda_{blue} < \lambda_i < \lambda_{red}$), means that the colors λ_i must be spaced more closely. This increases the spectral overlap and ISI.

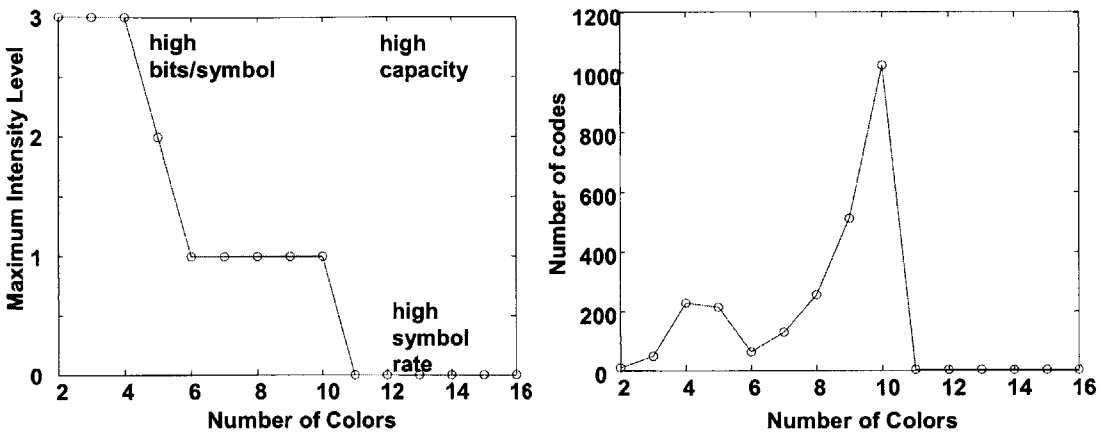

Figure 4-11: Left: shows maximum number of levels versus number of colors for PAM codes. Right: Number of codes versus number of colors.

Fig. 4-11 shows that the best results are obtained by using a 10 color binary architecture with 1023 codewords (all zeros is not valid). In the literature, it has been speculated that a "realistic" scheme would use PAM with 5 or 6 colors and 6 intensity levels for a total of 10,000 to 40,000 codewords [31]. However, our simulation indicates that for 5 colors, only 3 intensity levels (0,1,2) can be used and still satisfy the error rates. This only yields 211 codewords, far less than the expected 10,000. A typical error in the PAM scheme involves mistaking between the codewords: (203) and (304). Since there is no absolute intensity, only the ratio of the intensities matters, and 2:3 is close to 3:4.

In order to get a better intuition for how efficient a code is, we have created a type of diagram that is similar to a CIE diagram and plots all of the codewords (for a 3 color case) in a triangle. (see Figure 4-12) After choosing a particular code with 3 colors, we generate a set of noisy instances for each codeword. Then, we do a least squares curve fit to the amplitudes of 3 Gaussians summed together (the center and linewidth are fixed at their expected values) for each of the noisy instances. The 3 amplitude fits are used to generate a coordinate which is shown as a dot in the diagram. The sum of the 3 amplitudes is normalized to 1 and each amplitude is used as a scalar multiplier for a unit vector pointing away from the origin on the diagram. For example, the vector for color #2 points vertically from the origin and hence the code (010) shows up on the diagram at x=0, y=1. The 3 corners of the triangle correspond to having just 1 color, and the center of the triangle corresponds to having equal parts of each color.

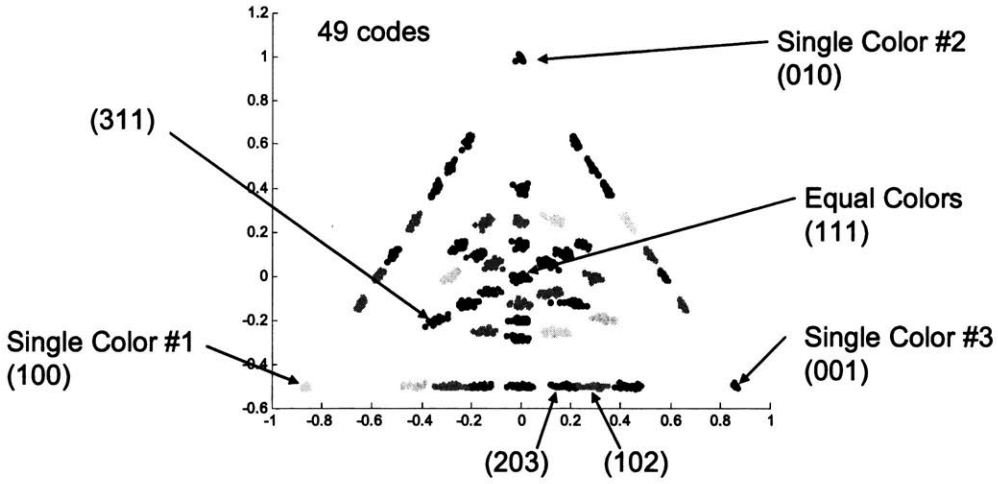

Figure 4-12: The diagram shows the codewords for PAM (3 colors, 4 levels) Scatter plot for 3 color codes. A least squares curve fit to the amplitude of 3 Gaussians is performed on several noisy instances of each codeword and the result is plotted as a point (a random color is chosen for each codeword). Each of the corners of the triangle corresponds to pure colors, and the middle is an equal weighting of each color. The noise has a different magnitude and shape in different regions.

Fig. 4-12 shows that the noise has a different magnitude and shape in different regions, and that the spacing of the codewords for the PAM scheme is quite inefficient. Along the lower edge of the triangle, the noise is in a horizontal line and is primarily due to the noise in the amplitude which is what causes the most errors for PAM codes. Figure 4-12 shows that the codewords (203) and (102) are very close and that the scatter plots overlap a bit, indicating errors.

A simple way to minimize these kinds of errors is to use PAM but choose codewords of equal weight (the sum of elements are equal). This method provides a kind of error correction since two of the elements need to be incorrect in order to create another valid codeword with the same weight. In this scheme the "nearest neighbors" of (063) are {(072), (162), (153), (054)} all of which differ by at least 2 elements. (see Fig. 4-13) We find that the optimal code uses 5 colors and a weight of 10 for a total of 1001 total codewords, which is actually worse than non-equal weight PAM.

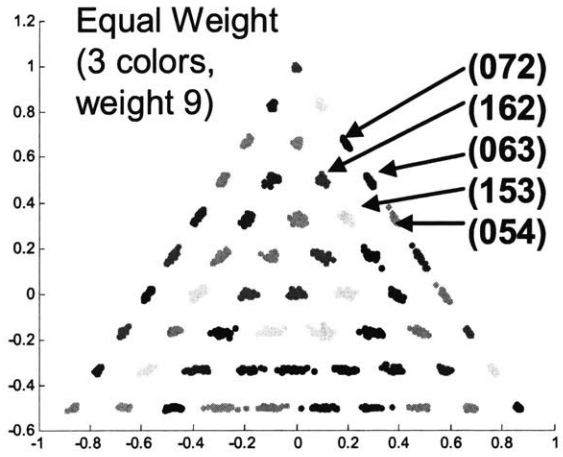

Figure 4-13 Diagram of equal weight PAM (3 colors, weight 9)

However, a further improvement can be made by adding the additional constraint that there must be at least 1 zero between any 2 colors with non-zero elements. Using this, we find that the optimal code uses 8 colors and a weight of 12 for a total of 2164 codewords. (see Figure 4-14) Intuitively, this technique gives better results because more information can be stored in the color choice of the non-zero elements – it is a kind of mix between amplitude modulation and pulse position modulation. (For example, if we consider a return-to-zero coding scheme with 6 colors, then there are 4 ways to arrange the elements (1,2,3) in that order {(102030), (102003), (100203), (010203)}. In the PAM coding scheme with 3 colors, there is only 1 way to do this.) In fact, the return-to-zero coding scheme can be improved further by constraining codewords to have at least 2 zeros between non-zero elements. In this scheme, the optimal parameter choice is 10 colors with a weight of 15 for a total of 2586 codewords. If the noise associated with the center wavelength were reduced, then further gains could be made by constraining codewords to have even more zeros between non-zero elements. However, for our choice of parameters the return-to-2zeros scheme is the best regular coding scheme that we have been able to come up with. Looking at Fig. 4-12 it is clear that codes should not be spaced evenly, but instead should be packed more densely in regions with low noise and less densely in regions with high noise. The next section discusses our Monte Carlo code generation algorithm which achieves exactly this.

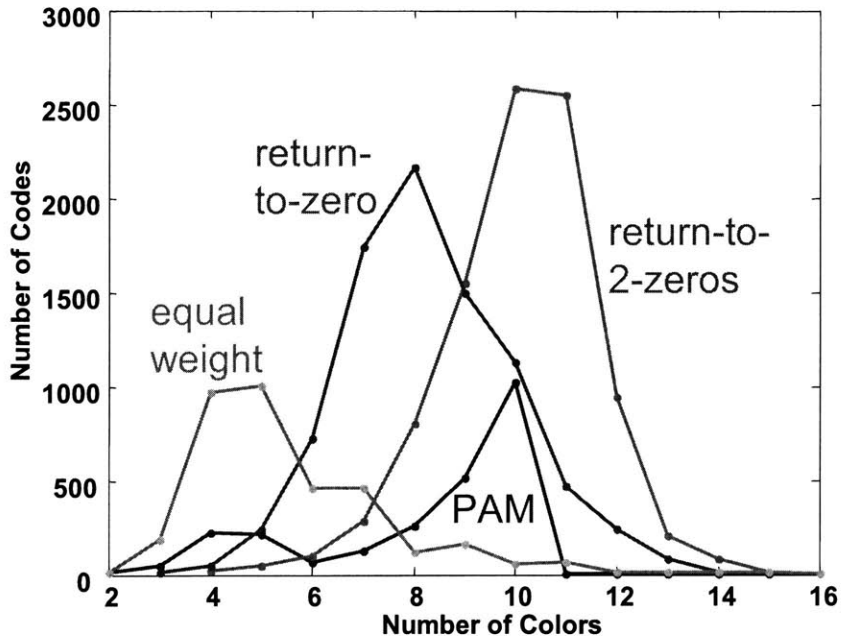

Figure 4-14: Codewords versus number of colors for different regular PAM based coding schemes described in the text.

4.6 Monte Carlo Code Generation

This section describes the details of our Monte Carlo code generation algorithm and its results. Using this technique we find a code with 9000 codewords, a large improvement over the regular codes discussed in the previous section.

4.6.1 Barcode Generation Results

We begin by describing our Monte Carlo code generation algorithm for three colors. First, we randomly generate a trial PAM codeword with 100 levels (a list of 3 numbers from 0-99). We then generate 100 noisy fluorescence spectra for that trial codeword, and decode using the usual technique with the trial codeword plus all of the codewords that are already part of the code. If all of the noisy fluorescence spectra are decoded correctly, then the trial codeword is added to the code. If any are incorrectly decoded, then we throw out the trial codeword and continue by generating another random trial codeword.

Figure 4-15 shows the results of this Monte Carlo code generation. This technique allows codewords to be packed more closely in regions that have low noise, and further apart in regions where the noise is larger. In fact, Fig. 4-15 shows that the codewords along the bottom edge of the triangle are spaced closer in the vertical direction than the horizontal, which is exactly what we want since the noise is larger in the horizontal direction. This code generation procedure can be continued indefinitely, but it is clear that there is a limit to how many codewords can be added to the code while still satisfying the error rate condition.

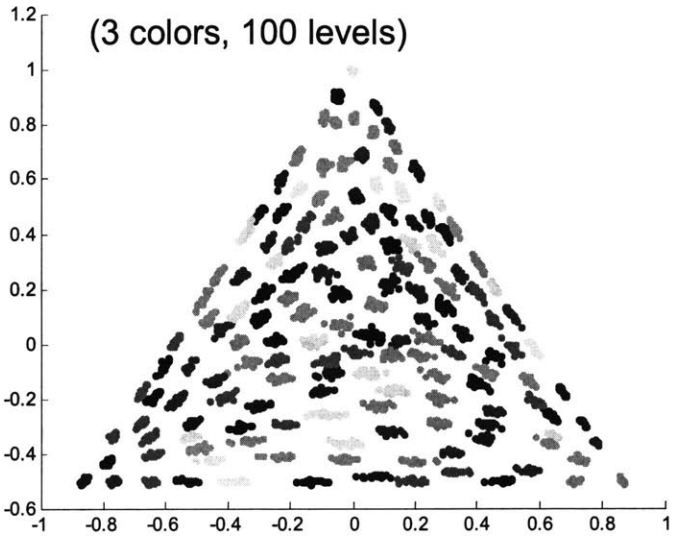

Figure 4-15: Triangle diagram for Monte Carlo code generation.

Figure 4-16 shows the results of our Monte Carlo code generation as a function of the number of colors. The number of codes increases monotonically as expected, although it is perhaps surprising that some of regular coding schemes manage to do better than the Monte Carlo generation scheme for a certain number of colors. We attribute this to the fact that in the PAM based schemes, the codewords are spaced in a regular fashion and hence can be packed efficiently. The Monte Carlo scheme, on the other hand, sometimes leaves spaces between codewords that are large, but not large enough to fit another codeword, and therefore there is some wasted space. Using the Monte Carlo generation procedure with 50 colors, we have found a code with over 9000 codewords that still satisfies the error conditions. Although this result can presumably be improved upon, it does set a lower bound on the number of codewords that is over 8 times bigger than the PAM scheme. The algorithm that is used to create this large code must be carefully designed in order to be computationally efficient.

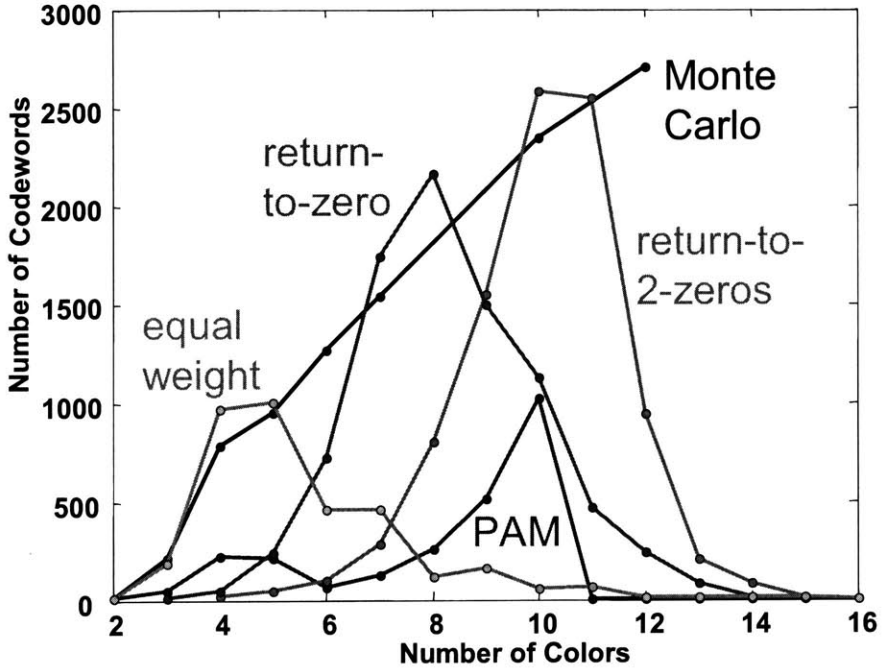

Figure 4-16: Number of codewords versus the number of colors for various coding schemes. For each choice of coding scheme and number of colors, the weight/number of levels and error threshold β are optimized to maximize the total number of codewords while still maintaining a correct>80% and incorrect<0.5% error rate.

4.6.2 Barcode Generation Algorithm Details

The Monte Carlo code generation with 50 colors requires careful thought to get the best results since it is computationally impossible to consider all 100^{50} possible codewords. A code generation technique that generates a random number uniformly distributed between 0-99 for each of the 50 colors gives poor results. This simple technique tends to preferentially generate codewords with a fluorescence spectrum that is relatively flat and therefore similar to other spectra in a MSE sense. For example, {99, 0, 99, 0, 99, 0, ...} is almost indistinguishable from {50, 50, 50, 50, 50, 50, ...} in the MSE sense even though they are far apart in a traditional Hamming distance sense. This happens because each color overlaps massively with its neighbor since they are spaced by 2.4nm and have a linewidth FWHM > 30nm. Figure 4-17 shows six trial codewords using this simple technique (n=1 strategy). All six are relatively smooth and are similar.

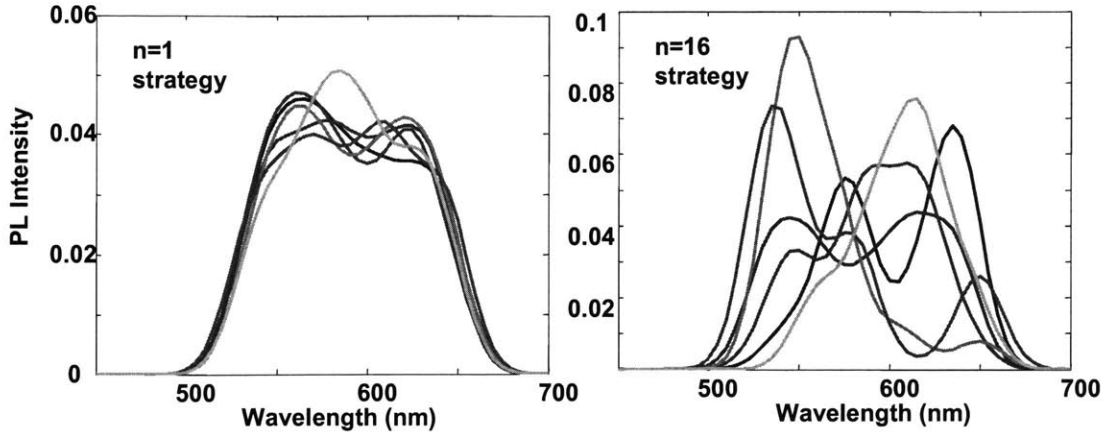

Figure 4-17: The first six trials of the n=1 and n=16 strategies.

In order to get sharp spectral features, most of the numbers should be small or zero with only a few large numbers. This can be accomplished by first generating 50 uniformly distributed numbers, then exponentiating each to some power n, normalizing so that the largest possible value is 100, and rounding to the nearest integer. Following this procedure on the vector {0, 20, 80, 40, 60, 0, ...} with a power n=2, gives the new vector {0, 4, 64, 16, 36, 0, ...}. Using a power n=6 gives {0, 0, 26, 0, 5, 0, ...}, which will generate a spectrum with sharper features than the original vector. Fig. 4-17 shows that codewords generated with the n=16 strategy have sharper features and are less similar in the MSE sense. As n becomes larger the generated spectra become even more peaked and start to look like one another again.

Our Monte Carlo code generation algorithm uses seven strategies to generate trial codewords n=1,2,4,8,16,32,64. We keep track of success rate = (number of times the trial codeword is added to the code)/(number of attempts) for each strategy. Each time through the algorithm we choose a strategy based on what has worked in the past, such that the probability of choosing a strategy is proportional to its marginal success rate. (We start the simulation by artificially giving each strategy 1 success and 1 attempt.) The idea behind this, is that if a particular strategy is generating a lot of codewords that are similar (in the MSE sense), like the n=1 strategy, then eventually its success rate will decrease and therefore its probability of being chosen as a strategy will decrease and other more productive strategies will be used instead. Using this kind of strategy diversity ensures that our algorithm is robust. Figure 4-18 shows the number of attempts and successes for each strategy in our algorithm. The n=4 and n=8 strategies have high success rates relative to other strategies, and hence they are preferentially chosen.

Interestingly, we find that using a diverse set of strategies has a higher overall success rate after 30,000 attempts than an algorithm that only uses the n=8 strategy. We attribute this outperformance to the fact that any one particular strategy tends to generate similar codewords and hence preferentially fills a certain fraction of the total codeword phase space. Other strategies can then fill in the less filled parts of the phase space.

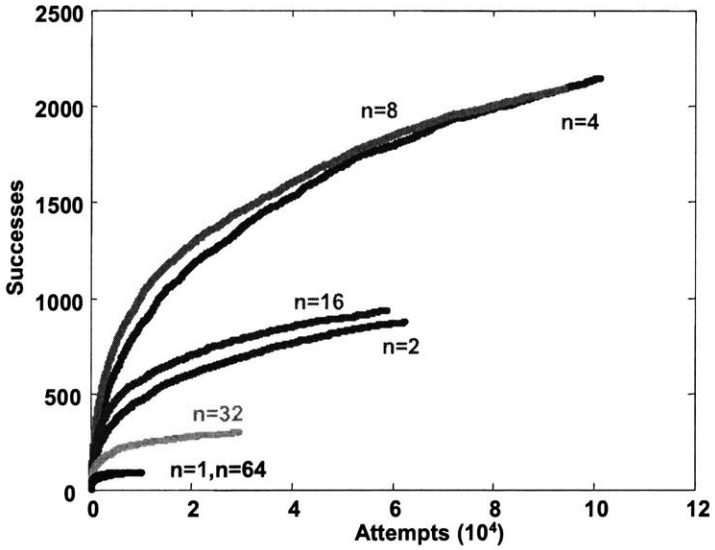

Figure 4-18: Plot of the number of trial codewords versus the number of successful attempts for each strategy we used. The probability of choosing a particular strategy is based on the marginal success rate.

4.6.3 Information Theory

At this point, it is worth stepping back again to consider how our Monte Carlo code differs from codes used in "typical" communications applications. Often, the modulation and channel coding decisions are considered independently. In our case, these have been combined and we directly try to find codewords that are spaced such that noise does not cause a codeword to be incorrectly decoded. Another difference is that for our application we do not expect the noise to be independent of the signal or to have a trivial structure. As a result it is difficult to find a regular coding scheme that uses all of the information capacity that is available. Instead, we find that by using our Monte Carlo generated code we are able to more fully utilize the information capacity of a microbead barcode.

While it is relatively easy to visualize what is happening when only 3 mostly non-

overlapping colors are involved, it is much more difficult to visualize what is happening when 50 colors with a lot of overlap are used. In order to help get an intuition for what is happening, we have plotted the power spectral histogram of the error sources and signal for our 50 color Monte Carlo code in Figure 4-19. (The signal power histogram is generated by averaging the magnitude of the Fourier transform of the spectral contribution of the noise from just one source. The noise power histograms are generated by averaging the magnitude of the Fourier transform of many instances of the spectra of just the noise source. Although Shannon's Theorem can not technically be applied since the signal and noise are not independent, pretending that the signal and total noise are power spectral densities and applying Shannon's Theorem yields a microbead capacity of 19 bits.) The plot shows that the power spectrum of the signal decreases at higher frequencies. This makes sense because the linewidth of 1 color of NCs effectively acts like a low pass filter. Fig. 4-19 shows that for low frequencies, which is where most of the information capacity lies (S/N is the best), the uncertainty in the center wavelength is the dominant noise source. This is interesting because it suggests that uncertainty in the center wavelength of NC ensembles may be the limiting factor for NC-bead based barcodes. This is in contrast to [75] which hints that the uncertainty associated with the intensity of different colors of NCs may be the limiting factor. However, a better and more direct way to understand what noise sources are most critical is to perform a sensitivity analysis on the parameters in our model.

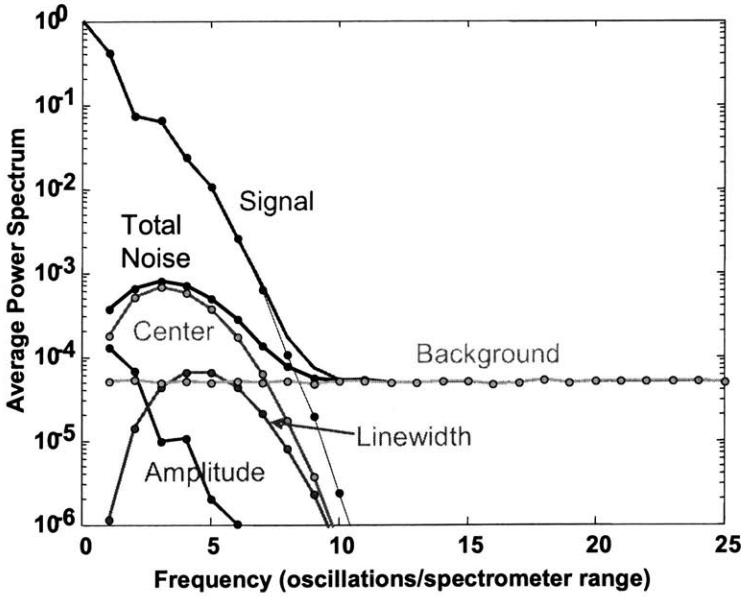

Figure 4-19: Power spectral histogram of the 50 color Monte Carlo coding scheme. Each line of the labeled lines shows the power spectral density of each power source individually. The dotted line corresponds to the total luminescence, and the solid black corresponds to all of the noise sources.

4.7 Other System Considerations

In this section we consider how sensitive our model is to the parameters we have used and estimate the system throughput.

4.7.1 Sensitivity Analysis

We performed a sensitivity analysis of our model in order to assess the importance of our parameter choices. For each parameter, we made a slight change (~20%) and then varied the number of colors, number of intensity levels, and the relative error threshold β in order to maximize the number of codewords while still satisfying our error constraints (correct > 80%, error < 0.5%). We use an equal weight return-to-2-zeros architecture for this analysis. Using the Monte Carlo code generation for a sensitivity analysis is complicated by the fact that we do not know of any way to quantify how well filled the code space is, and therefore can not be sure that we have waited long enough for the algorithm to fill the code space. Figure 4-20 shows how a 1% change in each parameter is expected to change the total number of codewords = 2^{bits}. The results show that a 1% increase in the NC color range (bandwidth) increases the number of bits by about 1%. It is comforting that this agrees with our intuition from the Shannon channel capacity $C = BW \times \log_2(S/N)$ which indicates that the capacity scales proportionally to bandwidth BW.

In our analysis we tried to choose parameters that are reasonable for currently available CdSe NC technology, but it may not be too difficult to expand the range of colors that are available by using CdS or CdTe NCs. All of these types of NCs can be capped with tri-n-octylphosphine oxide (TOPO), which should allow them to be incorporated into the same polymer and could vastly expand the number of barcodes. Also, our results show that reducing the ensemble linewidth is important. A narrower linewidth will reduce spectral overlap and ISI.

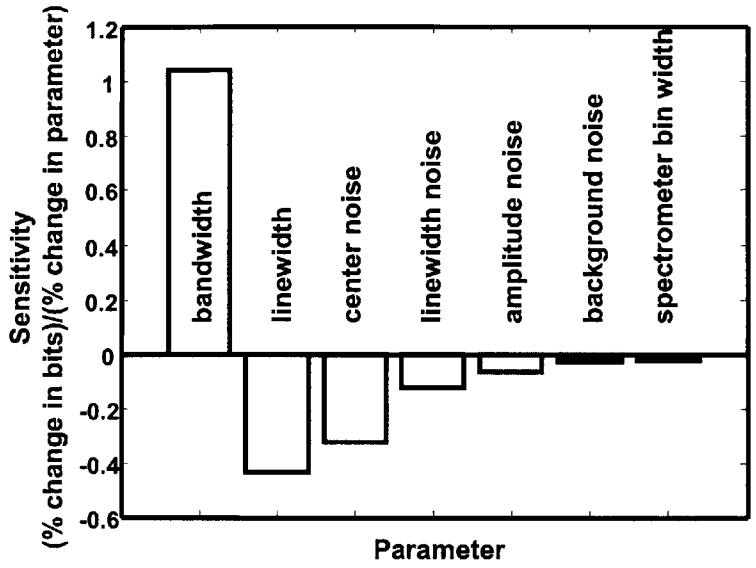

Figure 4-20: Sensitivity analysis of parameters in simulation. A PAM architecture with equal weighting and return-to-2zeros constraints is assumed for this analysis.

The sensitivity to different noise sources gives qualitatively the same answer as the power spectral histogram: the uncertainty in the center wavelength dominates. It is noteworthy that we do not appear to be limited by the relatively large 5 nm spectrometer bin width that we have used. In fact, we can increase the bin width to 12.5nm with only minor effects on our results, which makes intuitive sense when one considers the Nyquist criterion. According to the Nyquist criterion if we sample a bandlimited signal at twice the signal bandwidth, then the original analog signal can be recreated with perfect fidelity. Because the "impulse response" of our system (the sharpest spectrum we can create) has a linewidth of about 30nm FWHM, we should be able to sample at 15nm spacing (half the impulse response linewidth) without losing much information. An additional error source is due to uncertainty in the temperature.

Since both the emission wavelength and linewidth are temperature dependent, any uncertainty in the temperature of the microbeads will introduce additional noise. Figure 4-21 shows our measured temperature dependence of the ensemble emission wavelength for CdSe/ZnS NCs. We model this by linearly interpolating between a temperature dependence of $d\lambda/dT$=0.11nm/K for λ=650nm NCs and $d\lambda/dT$=0.08nm/K for λ=530nm NCs. Figure 4-22 shows our measured temperature dependence of the ensemble emission linewidth for CdSe/ZnS NCs. Since the slope is similar for all sizes, we model the linewidth with a linear temperature dependence such that the linewidth (FWHM) increases by λ=2nm for a T=40K change in temperature.

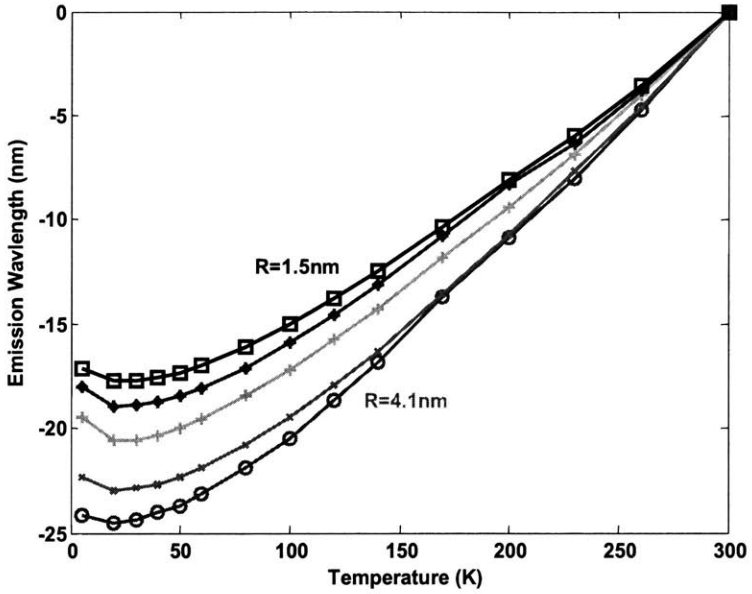

Figure 4-21: Measured temperature dependence of the emission wavelength for 5 sizes of CdSe/ZnS NCs. The wavelengths are offset to equal zero at T=300K so that the slopes can be compared.

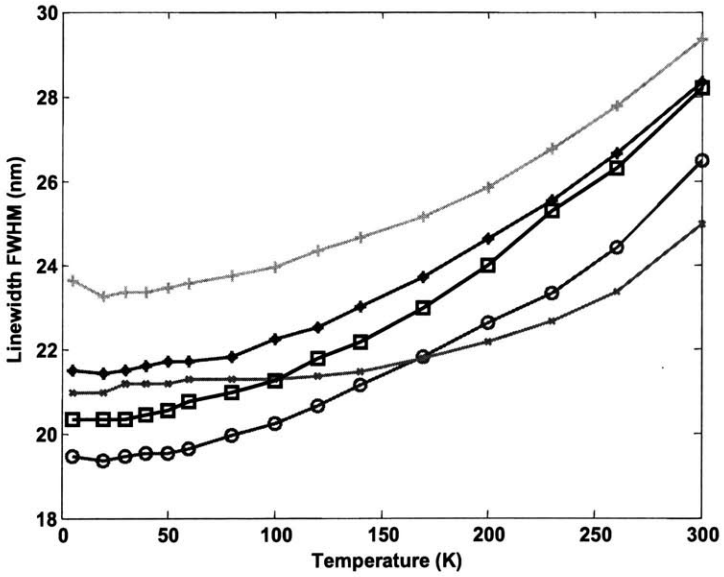

Figure 4-22: Measured temperature dependence of the emission linewidth for 5 sizes of CdSe/ZnS NCs. Color and shape convention is the same as previous figures.

To estimate the effects of an unknown temperature offset, we adjust the NC emission spectra accordingly but do not change our decode algorithm. We then find the set of parameters that maximizes the number of codewords with an acceptable error rate. Figure 4-23 shows the

results of our simulation. Our simulation indicates that an unaccounted for 20°C increase in temperature will reduce the maximum number of distinguishable codewords within the PAM return-to-2zeros scheme from 2586 to 1066. Such a large temperature uncertainty seems unlikely in a real system. However, if the temperature uncertainty of the microbead system is a concern, we expect that the performance degradation can be minimized by installing a thermometer inside the microbead system and then adjusting the expected emission spectra for each codeword in the decode procedure. In fact, our simulations indicate that if the temperature offset is known and the temperature dependence of NC emission spectra has been characterized, then the expected center wavelength and linewidth can be modified in the decode algorithm, allowing for the full 2586 code to meet the error rates across a -30°C to +30°C offset range. We conclude that temperature uncertainty will not be a major source of error in a NC based microbead system.

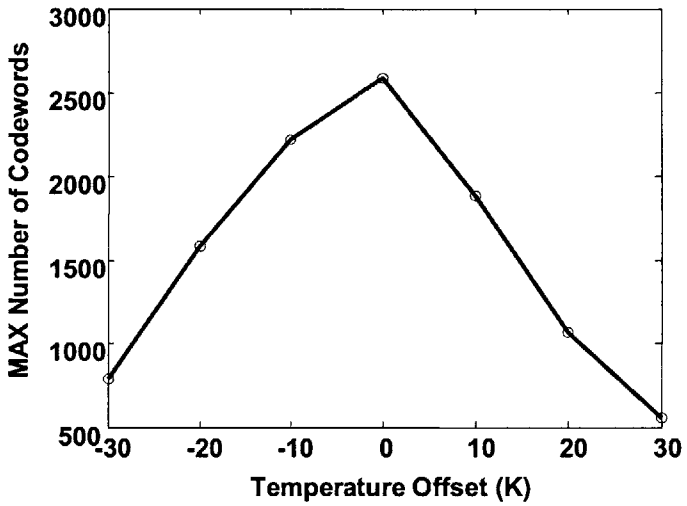

Figure 4-23: Simulation of the maximum code size using a PAM-return-to-2-zeros scheme if there is an unknown temperature offset.

4.7.2 System Throughput

Finally, it is important to remember that for the applications that we are considering - medium density biological assay applications – we would like the throughput to be as high as possible, but we need to make sure that there will be enough collected light to properly decode. A 5μm bead can have about 1 million NCs, each of which can emit 100 photons in the 10 μs that it is in the path of a focused argon laser [74]. Assuming 1% collection efficiency, about 1 million photons will reach the detector per microbead. The photons will be mostly spread over 24 spectrometer

bins (120nm range, 5nm/bin). So, about 40,000 photons will reach each bin, and photon shot noise will be less than 1% of the signal. Since this is less than the white noise that has already been added to our noise model, we don't believe that the throughput of the system will necessarily be limited by the amount of light that can be detected by the optical detection system.

4.8 Conclusion

In conclusion, for many biological applications there is a desire to be able to perform medium density (~1000) assays with high throughput. In order to assess the viability of using NC-based (instead of dye based) barcodes we have created a Monte Carlo simulation of NC barcodes that is grounded in what is currently achievable using today's technology. We find that the simple PAM coding scheme can be improved upon by using an equal weighted, return-to-2zeros PAM coding scheme. Furthermore, we used a Monte Carlo technique to generate a code with over 9000 codewords that satisfies our error conditions. This number of codewords is much bigger than the 100 currently available dye based commercial technology, but is much less than the 1 million codewords that has been mentioned in the literature. Our analysis shows the perhaps unintuitive result that the number of distinguishable codewords can be increased quite dramatically by using many different colors of NCs even though their spectra massively overlap! Accordingly, we conclude that controlling the center wavelength of NC ensembles will be the limiting noise source, rather the amplitude uncertainty. We hope that our work provides a useful framework for thinking about NC based microbead barcodes, even if future developments indicate that the noise model should be modified. Finally, our analysis indicates that NC-based barcodes have the potential to fill the need for medium-density high throughput biological assays. Whether this technology ever comes to fruition will largely depend if it is economically advantageous to create such a system.

From the perspective of information theory and channel coding, our problem seems quite unique. In practice, most problems are in the long block regime (~1000 bits) and it is computationally impractical to run a Monte Carlo code generation algorithm. In this situation, the concept of a random code generation is used as a theoretical concept, but is not actually implemented. However, the microbead barcode problem is in such a small block length regime (~10bits/barcode), that it is actually computationally possible to implement what is normally a theoretical concept. At the same time the problem is complex enough, that there is no easy analytic solution to our problem, and a Monte Carlo simulation seems to be the only option. We

are not aware of any other applications that fall into this small block length regime, where constructing a code is nontrivial analytically, but small enough to be tractable using a Monte Carlo approach.

Chapter 5

Conclusions

This thesis has investigated the optical properties of semiconductor nanocrystals and attempted to relate these properties to NC applications. In Chapters 2 and 3 we presented our experimental measurements of CdSe/ZnS NCs and investigated the physical mechanisms that have been invoked to explain the temperature dependence of the exciton energy, the Stokes shift, and the spectral linewidth. In Chapter 4 we used a Monte Carlo simulation to investigate the prospects of using NC based microbead barcodes for high throughput biological assays.

This chapter reviews our main conclusions, discusses the implications for NC applications, and suggests directions for future research. In section 5.1 we review our conclusions regarding the physical mechanisms responsible for NC optical properties and relate these conclusions to the applications discussed in Chapter 1. In section 5.2 we review the prospects for NC based microbead barcodes for high throughput biological screening. We also review microbead barcodes through the lens of information and coding theory, and suggest additional topics for future research.

5.1 Implications of NC Physics for Applications

This section reviews our conclusions regarding the temperature dependence of the emission energy dE_{emi}/dT and the spectral linewidth of semiconductor nanocrystals. We discuss the implications of these properties for the applications discussed in Chapter 1.

5.1.1 Temperature Dependence of the Emission Energy dE_{emi}/dT

In Chapter 2, we showed that a first order model that only considers changes in the effective mass with temperature can explain the existing experimental measurements of dE/dT for both epitaxial QDs and colloidal NCs, and hence both types of systems can be modeled using the same physical

framework. Previously, there was no model, either theoretical or semi-empirical, to predict the temperature dependence of the exciton energy dE/dT in nanostructures. Our absorption measurements of high quality CdSe/ZnS NCs show that there is no measurable size dependence to dE_{abs}/dT, in contrast to earlier measurements in lower quality CdSe and CdS NCs. We explained most of the size dependence in dE_{abs}/dT in PbS and PbSe NCs by the strong temperature dependence of the effective mass of these materials. Previous explanations neglected this simple, yet dominant physical effect.

One way to test our model is to measure the temperature dependence of the absorption energy dE_{abs}/dT of InSb quantum dots, which our model predicts will be reduced from its bulk value because of the large percentage change in effective mass as a function of temperature. It is difficult to make an exact prediction due to the lack of reliable measurements of the effective mass with temperature, but k·p theory indicates that materials with a large percentage change in $E_g(T)$ with temperature should also have a large percentage change in effective mass with temperature. Specifically, reference [39] indicates that the percentage change in effective mass with temperature for InSb is about $d\%m^*/dT = -4\times10^{-4}/K$ near room temperature, while reference [76] indicates that at room temperatue, E_g=170meV and dE_g/dT=-0.33meV/K. Using $\frac{dE_{conf}}{dT} = E_{conf}\left[\frac{-1}{m}\frac{\partial m}{\partial T} - \frac{2}{R}\frac{\partial R}{\partial T}\right]$ we find that if a nanostructure was made with E_{conf}=1000meV, then our model predicts dE/dT=0. It is important to note that as the confinement potential increases, the effective mass approximation will break down. The parabolic band approximation fails as increasing confinement forces electrons further from the band minimum. Additionally, once the confinement energy becomes comparable to the bulk bandgap, the effective mass approximation will break down. However, we expect that even for InSb nanostructures with smaller confinement energies (100s of meV), there should be a measurable decrease in the magnitude of dE/dT from bulk.

In Chapter 2 we focused on dE_{abs}/dT, while Chapter 3 focused on the temperature dependence of the Stokes shift $E_{abs}(T)$-$E_{emi}(T)$. Combining these two properties one is able to model the temperature dependence of the emission energy dE_{emi}/dT, an important parameter for many NC applications. Our measurements on CdSe NCs show a weak temperature dependence of the Stokes shift near room temperature and hence dE_{emi}/dT is similar to dE_{abs}/dT. In fact, in the literature it is often implicitly assumed that dE_{emi}/dT and dE_{abs}/dT are the same. Having any model for dE/dT in useful for assessing potential NC applications.

In chapter 1 we discussed using NCs imbedded in organic devices as light emitters as a way to provide a solid state solution for yellow traffic lights. Currently, the options for solid state

yellow lights are limited by material properties. Because of the narrow spectral range perceived as yellow by the human eye and the wide temperature range that a traffic light is subjected to, a crucial specification for yellow traffic lights is the chromaticity drift as a function of temperature. British railway specifications allow $\Delta\lambda$=2.5nm of chromaticity drift from -20°C to +40°C. Our measurements of CdSe/ZnS NCs show that the chromaticity drift across this temperature range is $\Delta\lambda$~6nm, thus precluding the use of CdSe/ZnS NCs for this application. However, PbS or PbSe NCs may provide an answer. Since the Stokes shift is small in PbS and PbSe NCs, the temperature dependence of the absorption energy should be a good approximation for dE_{emi}/dT. Measurements from [17] indicate a chromaticity drift $\Delta\lambda$=0±1nm for PbS NCs across the relevant temperature range, indicating their potential suitability for yellow lighting applications. Although, the quantum efficiency of PbS NCs may be a concern. Our analysis indicates that InSb nanostructures are potentially another good solution.

Another potential application is to use NCs as a temperature sensor with a high spatial resolution (10s of nanometers). Researchers have demonstrated the ability to deposit a monolayer of NCs in organic electronic devices. By measuring the emission spectrum of NCs, the temperature of the organic device at the depth of the NCs can be inferred. It is difficult to imagine how to measure the temperature with 10 nanometer resolution using traditional techniques. For this potential application, it is desirable to make dE_{emi}/dT as large as possible in order to increase the temperature sensitivity. In general, materials with a large dE_g/dT and with a minimal temperature dependence of the effective mass are desirable for this application. Large CdSe/ZnS NCs have $d\lambda/dT$~0.1nm/K making them ideal candidates for this application. Figure 4-21 shows that the temperature dependence of the emission wavelength of CdSe/ZnS NCs scales with size, making larger CdSe/ZnS NCs more sensitive temperature probes. Our measurements indicate that it is reasonably easy to detect changes of T=2°C using CdSe NC emission spectra. Infrared images of OLEDs in [77] show that surface temperatures can reach 50°C before degradation begins. The ability to measure internal temperatures, which are presumably even higher, with T=2°C temperature resolution and a vertical spatial resolution of approximately 10nm could allow the internal temperature of OLEDs to studied with far greater precision than is possible using traditional techniques. The temperature dependence of the emission energy will have an impact on other applications, but it is often of secondary importance compared to the spectral linewidth.

5.1.2 Spectral Linewidth and Stokes Shift

In the literature, both exciton fine structure and exciton-acoustic phonon scattering models have been used to explain a wide variety of experimental results in CdSe NCs. These two theories are based on fundamentally different physical mechanisms and normally only one model is invoked to explain the results of an experiment. In Chapter 3 we presented our careful measurements of the temperature dependence of the ensemble emission and absorption spectra for different sizes of CdSe/ZnS NC ensembles. Our experiment is performed in a regime where both theories are potentially important, and therefore allows us to compare the theories directly. We interpret our results through the lens of both theories.

In the fine structure framework, the temperature dependence of the Stokes shift gives a highly sensitive measurement of the energy levels and oscillator strengths. As the temperature is lowered from T=30K to T=5K, our measurements show a sharp 2-4meV increase in the Stokes shift for different NC sizes. This behavior indicates the existence of lower energy level with small oscillator strength, consistent with the existence of a dark exciton. The 2-4meV increase of the Stokes shift is a measure of the energy difference between the dark exciton and the lowest bright exciton state, and agrees well with temperature dependent lifetime measurements [42]. At temperatures higher than T=40K, the dark exciton is expected to have a minimal impact in determining either the emission or absorption spectra because of its small oscillator strength. As a result, the temperature dependence of the Stokes shift between T=40K and T=300K provides a sensitive measure of the energy level spacing and oscillator strengths of higher fine structure energy levels. Previously, PLE experiments provided the only experimental measurements of the upper fine structure levels that we are aware of [24]. According to the fine structure theory, we expected to find a strong temperature dependence of the Stokes shift especially for our smallest NCs. Surprisingly, we measured a weak temperature dependence of the Stokes shift for all sizes of CdSe/ZnS NCs between T=40K and T=300K. Although these results were unexpected, we found that adequate agreement could be obtained by adjusting the parameters in the fine structure theory to fit our experimental results. Within the fine structure framework our results provide a sensitive measure of the energy levels and oscillator strengths. However, the fine structure model can not explain the temperature dependence of the spectral linewidth, which is considered to be a result of homogeneous broadening which results from exciton-acoustic phonon scattering.

Within the exciton-acoustic phonon scattering model, the absorption and emission spectra have a 'Prussian helmet' shape and are mirror images of one another about the ZPL. While the spectral broadening predicted by this model is well known, we are not aware of any mention of

this model's contribution to the Stokes shift in CdSe NCs, which turns out to be quite large. Using the exciton-acoustic phonon scattering model developed in Ref. [38], we are able to reasonably account for both the magnitude and size dependence of our measured Stokes shift and the ensemble linewidth temperature broadening. Importantly, this model uses only material parameters and has no adjustable parameters. However, we have measured single NC emission spectra which are narrower than predicted and are directly inconsistent with this model.

We conclude that neither the fine structure model nor the exciton-acoustic phonon scattering model can provide a complete description of the NC physics that is relevant for explaining NC optical properties. Although both theories are able to adequately explain experiments in certain regimes, it is not obvious how to combine the separate theories to explain experiments in a regime where both are important, like the temperature dependence of the Stokes shift. We speculate that a comprehensive theory that includes the physics of both the fine structure and exciton-acoustic phonon scattering is needed to explain our experimental results.

Figure 5-1 compares the implied single CdSe NC bandedge absorption spectrum from PLE experiments in [24] to the exciton-acoustic phonon scattering model of [38]. Previously, the wide high energy peak from PLE experiments was interpreted as a higher energy exciton level in the fine structure. We suggest that an alternative explanation is that this peak is due to exciton-acoustic phonon coupling. One way to potentially determine the correct explanation would be to measure the absorption of a single NC. At low temperatures, this peak would presumably be narrow if it is due to a fine structure level, while the exciton-acoustic phonon scattering model indicates a large width even at T=0K. In fact, the absorption spectrum of a single NC has been measured by performing PLE on a single NC [78], however the measurements were performed on a large NC where the difference between the two theories is minimal. If the single NC PLE experiments were repeated on small NCs, then measuring a narrow high energy PLE peak would strongly enhance the fine structure interpretation. In the end we suspect that reality is more complicated, and that a comprehensive theory which combines the physics from both theories is required. We hope that our work provides the motivation to perform additional experiments and to reassess the physics that has previously been used to explain experimental results.

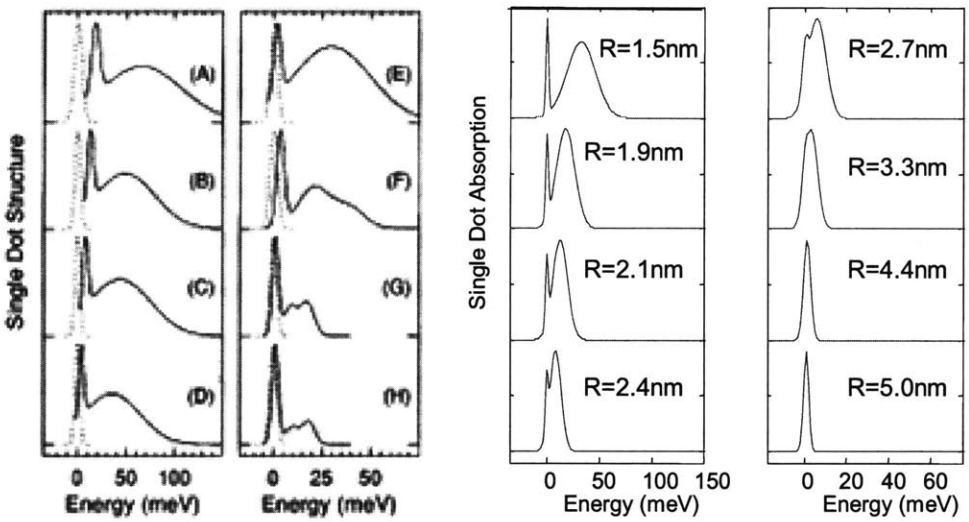

Figure 5-1: Left – inferred single CdSe NC bandedge absorption spectrum (without optical phonon replicas) from PLE experiments in [24]. Predicted absorption spectra of CdSe NCs based on exciton-acoustic phonon scattering model in [38]. The oscillator strength and linewidth of the ZPL are chosen to make the comparison more clear.

Another mystery that has yet to be consistently addressed, but may provide a clue to resolving the issues we have been discussing, is why adding a ZnS capping layer to a CdSe NC core increases the Stokes shift. A direct effect of adding a ZnS capping layer, is that the electron and hole wavefunctions are less confined, since they can extend into the ZnS capping layer, and hence the emission wavelength is red shifted. This effect indicates that the Stokes shift should be reduced since redder NCs have smaller Stokes shifts, however figure 5-2 shows that experimentally the opposite effect is observed [35, 79]. Adding a ZnS cap is also observed to broaden the emission linewidth. Previously, this broadening has been interpreted as resulting from an increased effective size distribution of the NCs. The increased Stokes shift was then explained by the increased contribution of inhomogeneous broadening [35]. Our calculations of the contributions of inhomogeneous broadening to the Stokes shift indicate that this is a small effect, and can not account for the increased Stokes shift. Figure 3-14 shows that a typical contribution of the inhomogeneous size distribution to the Stokes shift is 5meV for a high quality sample. Assuming that adding a ZnS capping layer increases the size distribution by 10% (from σ_R/R=5% to σ_R/R=5.5%), the contribution to the Stokes shift of the inhomogeneous size distribution will increase by approximately 1meV, to 6meV total. This is far less than the 20meV that is observed in [35]. We speculate that adding a capping layer may increase the lattice relaxation energy (within the exciton-acoustic phonon scattering model), and hence may increase

the Stokes shift. However, we are not aware of any quantitative analysis of exciton-acoustic phonon scattering for NCs with a capping layer to support our speculation.

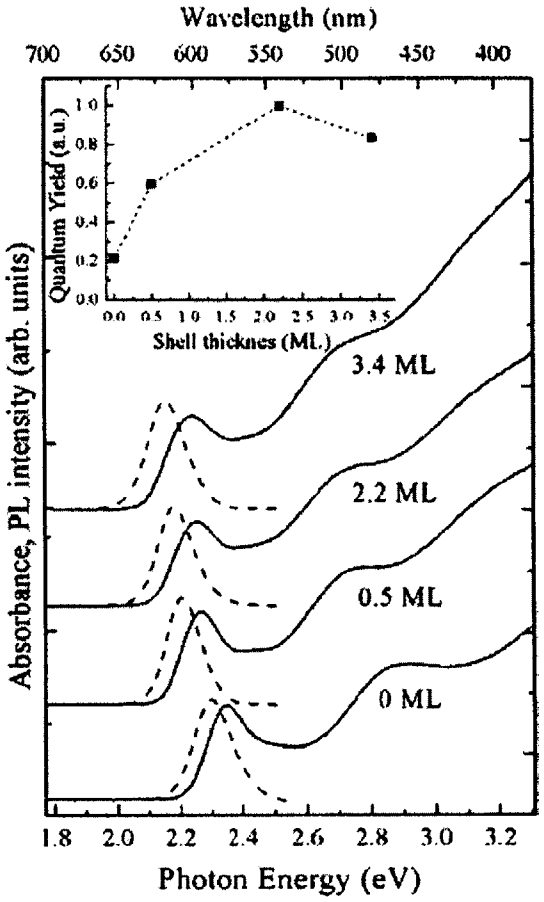

Figure 5-2: Absorption and emission spectra of CdSe NCs with different thicknesses, or monolayers ML, of the ZnS capping layer. (from [79])

Finally, we have estimated the contributions of the size distribution, spectral diffusion, and homogeneous linewidth to the ensemble PL linewidths for our samples at room temperature. Our analysis indicates that even if the inhomogeneous broadening due to size distribution and spectral diffusion could be eliminated, the room temperature homogeneous broadening will only allow the ensemble linewidth to be reduced to approximately half of the current value. The room temperature ensemble linewidth is an important parameter for many potential NC applications.

Reducing the ensemble linewidth by 50% would improve the performance of many applications. For NC based display applications, a wider range of colors could be displayed. On the CIE diagram, the points corresponding to NCs could be moved about half the distance from where they are currently to towards the edge of the diagram. For biological imaging, the number

of colors that can be used simultaneously could potentially double. For laser gain applications, the maximum gain would double for a given pumping power. For microbead barcodes, our sensitivity analysis indicates that the number of codewords could potentially be increased from about 2^{13} to 2^{20}. Whether it is worthwhile to devote time, energy, and money to reducing the emission linewidth is a complex question that will depend on the economic costs and benefits of doing so. The primary goal of our research was to analyse what is possible and to assess how improvements in NC manufacturing could improve NC applications.

5.2 Prospects of NC Based Microbead Barcodes

This section reviews the prospects of NC based microbead barcodes from the perspective of biology and from the perspective of information and coding theory.

5.2.1 Biological Assay Perspective

For many biological applications there is a desire to be able to perform medium density (~1000) assays with high throughput. Microbead barcodes are one commercially available method for performing biological assays. The advantages of replacing organic dyes with NCs for this application have been widely anticipated in the literature, but we are not aware of any quantitative analysis of what could be achieved. In Chapter 4 we analyzed the performance that a NC-based microbead system could be expected to achieve. Here we review our analysis and conclusions.

We began by making some design decisions regarding how a NC-based system would operate. Among our choices, we choose to use a spectrometer, to make decoding the barcodes independent of absolute intensity, and to decode based on MSE. We then developed a noise model based on what can reasonably be achieved experimentally using current NC and microbead technology. All of the parameters in our noise model have an experimental basis. We then developed a Monte Carlo simulation of the noise in our system in order to assess the decode error rates for different types of code design. We found that the simple PAM coding scheme that is suggested in the literature, performs much worse than anticipated. It was anticipated that 5 colors and 6 intensity levels could be used for a total of 7776 codewords, while we found that for 5 colors only 3 intensity levels could be used (and still satisfy our error conditions) for a total of 211 codewords. We then investigated other coding schemes. We found that the PAM results can be improved upon by using an equal weighted, return-to-2zeros PAM coding scheme which

allows over 2500 codewords. Furthermore, we developed a Monte Carlo code generation algorithm to find a code with over 9000 codewords that satisfies our error conditions. This number of codewords is much bigger than the 100 currently available using dye based commercial technology, but is much less than the 1 million codewords that were speculated as possible in the literature. Our analysis shows the perhaps unintuitive result that the number of distinguishable codewords can be increased quite dramatically by using many different colors of NCs even though their spectra massively overlap! Our sensitivity analysis indicates that controlling the center wavelength of NC ensembles will be the limiting noise source, rather the amplitude uncertainty as is implied in the literature. We hope that our work provides a useful framework for thinking about NC based microbead barcodes, even if future developments indicate that the noise model should be modified. Finally, our analysis indicates that NC-based barcodes have the potential to fill the need for medium-density high throughput biological assays. A goal of our research was to analyze what is possible using currently available technology. Whether this technology ever comes to fruition is a more complex question that will require weighing the economic costs and benefits of further developing this technology.

5.2.2 Information and Coding Theory Perspective

From the perspective of information theory and channel coding, NC based microbead barcodes seem quite unique. In practice, most coding problems are in the long block regime (~1000 bits) and it is computationally impractical to run a Monte Carlo code generation algorithm. In this situation, the concept of a random code generation is used as a theoretical concept, but is not actually implemented. However, the microbead barcode problem is in such a small block length regime (~10bits/barcode), that it is actually computationally possible to implement what is normally a theoretical concept. At the same time the problem is complex enough, that there is no easy analytic solution to the optimal design of NC microbead barcodes, and a Monte Carlo simulation seems to be the only option.

Additionally, our research raises questions that may be of interest to the information and coding theory communities. Can an algorithm be developed to space the codewords in a regular fashion, so that codewords can be packed more densely without increasing the error rate? In order to better picture what is going on, is there a way to extend the triangle diagram that we developed for the 3 color case, to more colors? Is there a way to quantify how fully a code covers the total coding phase space? Is there a way to improve our Monte Carlo code generation

algorithm to make it more computationally efficient? All of these questions strike us as potentially interesting topics for further research.

Appendix A

Frequency Domain Lifetime Measurements

We measured both the absorption and fluorescence lifetime of CdSe/ZnS NCs in the frequency domain. These experiments were a first step towards performing a spectral hole burning experiment at cryogenic temperatures. They were discontinued for multiple reasons: reference [29] reported excellent experimental results before we were able to complete the experiment, we had trouble getting a NC sample that was well matched to our laser wavelength (λ=635nm) at T=5K, and we found that careful measurements of ensemble absorption and emission were quite interesting and more assessable experimentally.

For the fluorescence lifetime measurements, we excited the NCs with a green LED that was sinusoidally modulated using a function generator. The λ=640nm NCs were suspended in toluene in a square cuvette. A New Focus 1801 detector that was connected to a SR844 lock-in amplifier was used to the measure the amplitude and phase of the fluorescence signal. To get a reference signal, the sample cuvette was replaced by a mirror and the LED excitation was measured directly. Figure A.1 shows that the relative amplitude and phase of the fluorescence agrees well with the prediction for a molecule with a τ=20ns lifetime. The slow response of our LED limited the frequency range of our measurement.

For the absorption lifetime measurement, we used a λ=635nm, 5mw diode laser modulated by an AOM (acousto optic modulator) to excite the NCs. This effectively modulated the absorption of the NC sample, which was monitored with a probe laser at the same wavelength. The induced modulation of the probe laser is detected with the same setup used for fluorescence lifetime. Fig. A.1 shows that the absorption lifetime agrees well with the fluorescence lifetime of τ=20ns. The most difficult aspect of this experiment is eliminating the effects of scattered pump light. It is difficult to separate the signal due to scattered pump light from the induced modulation in the probe laser.

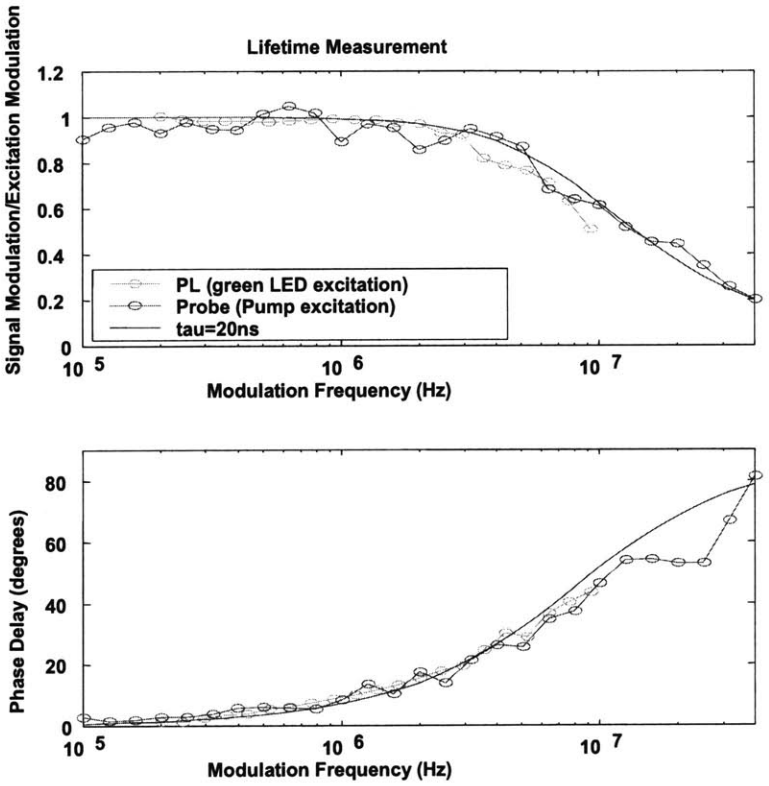

Figure A.1: Shows the magnitude and phase delay of both fluorescence and absorption lifetime measurements. The results agree well with the predicted lifetime of τ=20ns.

Appendix B

Thermal Fluctuations

Every object in thermal equilibrium with its environment has energy fluctuations. For large objects, these fluctuations are not noticeable since their heat capacities are large. However, because NCs have small heat capacities, these fluctuations can potentially be measurable. For instance, since the number of phonons in a NC fluctuates, even when the NC is in thermal equilibrium with its environment, and the excitonic energy of a NC is dependent on the number of phonons, the excitonic energy of a NC will fluctuate. This will manifest itself as linewidth broadening in the absorption and emission spectra. The goal of this appendix is to quantify this broadening.

B.1 Analysis to Date

Thermodynamics tells us that the thermal energy of any system in thermal equilibrium with a large reservoir will fluctuate. This is a result of the fact that any object is constantly exchanging heat with its environment. The dispersion in the energy of a system in thermal equilibrium is given by

$$\overline{(\Delta E_{thermal})^2} = kT^2 C_V$$

where C_V is the heat capacity of the system [80]. Because the thermal energy of a NC fluctuates, one can also think of the temperature of the NC as fluctuating. By relating a change in thermal energy to a change in temperature using

$$\Delta E_{thermal} = C_V \Delta T$$

a NC temperature fluctuation can be calculated. There is some controversy regarding the validity

of interpreting $\Delta E_{thermal}$ and ΔT as widths of the distribution of E and T. However, experiments using superconducting magnetometers to measure the temperature of paramagnetic salts at 2K are consistent with its validity [81]. Assuming the equation is valid, the above relations imply that

$$\overline{(\Delta T)^2} = \frac{kT^2}{C_V}$$

Using the heat capacity of bulk CdSe c_v=1.454 J/(cm^{3}K) and R~5nm one finds that ΔT~1K at room temperature. Arzberger and Amann have created a more complicated, but more accurate, model of NC temperature fluctuations using this equation as their starting point [13]. (The primary correction is to consider the volume of the electron and hole wavefunctions when calculating C_V, instead the NC volume.) Their model indicates an excitonic broadening of 1.8 meV at room temperature for R=5nm CdSe NCs. This is comparable to the expected 3 meV acoustic phonon broadening at room temperature and suggests that it may be important to include temperature fluctuations in any complete analysis of NC linewidth.

In their analysis, they use the bulk value of c_v at room temperature and assume that it is independent of temperature. In fact, $c_v(T=0)=0$ and increases with temperature. So, while their calculated broadening at room temperature should be reasonably accurate, they underestimate the broadening at lower temperatures. The next subsection analyzes the linewidth broadening at low temperatures (T<20K).

B.2 Our Analysis

For sufficiently low temperatures, only the lowest energy acoustic phonon mode has a significant chance of being occupied. Therefore, in the low temperature regime the thermal energy dispersion can be accurately estimated by modeling the NC as having only one phonon mode. The probability distribution of the number of phonons occupying that mode can be calculated using the canonical distribution

$$P_r = Ce^{-E_r/kT}$$

where P_r is the probability of the system being in state r, E_r is the energy of state r, and C is a constant of proportionality independent of r [80]. Adding up the probabilities of all states must

equal 1, so C is found to be $C^{-1} = \sum_r e^{-E_r/kT}$. We also know that the energy for oscillator is given by $E_n = (n + \frac{1}{2})\hbar\omega$. Combining these equations we find the probability of having n phonons in a mode is

$$P(n) = (1 - e^{-\hbar\omega/kT})e^{-\hbar\omega n/kT}$$

Figure B-1 plots the probabilities of n=0,1, and 2 versus temperature for an acoustic phonon mode with E_a=1.5meV. This is the energy of the lowest acoustic phonon mode in a CdSe/ZnS NC with R~1.5nm [29]. This single phonon model will break down when the probability of occupation of higher phonon modes becomes significant. Since the next highest acoustic phonon mode is expected to have an energy of about 3meV, and the probability of n=2 which corresponds to an energy of 3meV is about 7% at T=15K, this model should be reasonably accurate up to 15K. The mean thermal energy $E_{thermal}$ and the standard deviation of the thermal energy $\Delta E_{thermal}$ are calculated directly from the probability distribution of phonon mode occupation. Figure B-1 shows the probability of phonon occupation, the mean thermal energy, and the standard deviation of thermal energy versus temperature according to the above model. For T>15K this model will tend to overestimate the thermal energy dispersion.

The excitonic line broadening $\Delta E_{exciton}$ due to thermal energy fluctuations can be estimated using $\Delta E_{exciton} = (\partial E_{exciton}/\partial T) \times (\partial T/\partial E_{thermal}) \times \Delta E_{thermal}$. From the above analysis, we know the standard deviation in the thermal energy $\Delta E_{thermal}$, and can calculate the inverse slope of $E_{thermal}(T)$. Finally, our data indicate that $\partial E_{exciton}/\partial T$ is experimentally identical to bulk $\partial E_g/\partial T$. [Our preliminary data indicated that the average value of $\partial E_{exciton}/\partial T$ between 0 and 50 K was much larger than bulk, about -0.1meV/K, and spurred our interest in temperature fluctuations. However, after improving our experimental technique, we now believe that the bulk model is a good model.] Putting these pieces together gives a thermal linewidth of $\Delta E_{exciton}$(R=1.5nm, T=15K) = 0.02μeV. This is much smaller than what has been observed epxerimentally and what is expected theoretically due to phonon scattering. We conclude that excitonic broadening due to thremal fluctuations is not significant for NCs at low temperatures.

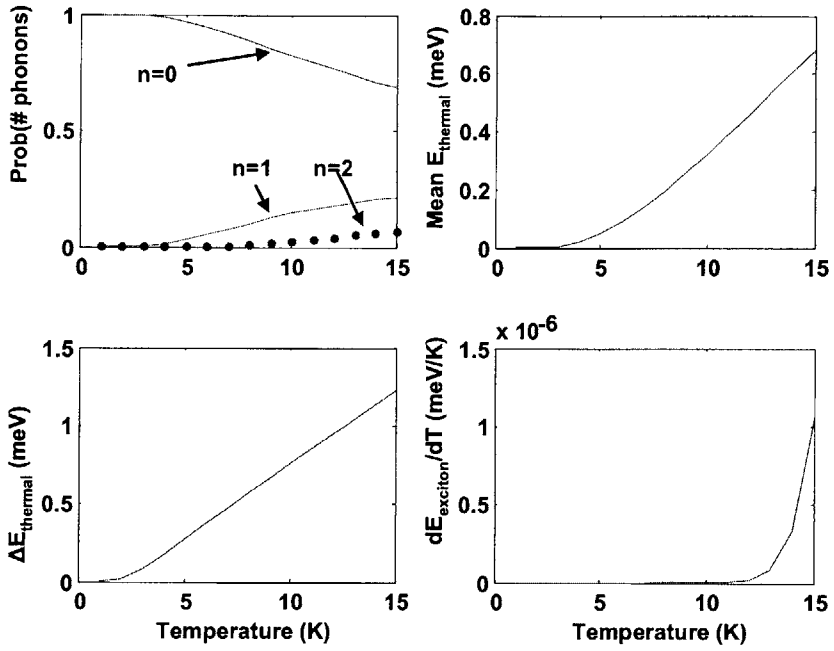

Figure B-1. Top left – Shows the occupation probability of n=0,1, and 2 for a phonon mode with E=1.5meV. Top right – Mean thermal energy is calculated using the occupation probability. Bottom left – standard deviation of the thermal energy distribution calculated using the occupation probability. Bottom right – derivative of $E_g(T)$ for bulk CdSe based on [82].

Appendix C

Calculation of Optical Trap Depth for a Nanocrystal

Initially we hoped to use a laser to optically trap a NC in free space. This was motivated by the belief that trapping the NC would minimize the environmental effects on the NC (since it would no longer be in contact with a substrate or polymer) and would therefore allow us to better measure the intrinsic properties of the NC. In retrospect, this idea is probably fundamentally flawed. NCs are typically coated with TOPO in order to passivate the surface states of the NC. Removing the TOPO is expected to quench the PL of a NC, since an electron or hole can get trapped in a surface state and therefore not recombine. Since the TOPO provides the local environment of the NC, and can not be removed, optically trapping a NC will not eliminate the environmental effects of TOPO on a NC. Here we present our calculation of the optical trapping potential for a NC.

The basic idea behind optical tweezers for small dielectric particles is quite simple. First, a laser is focused to a spot. The average magnitude of the electric field is greatest where the intensity is greatest, at the laser beam waist. Since the energy potential seen by a dielectric particle is given by $U=-(\alpha/2)|E|^2$, where α is the polarizability of the particle, the particle will feel a force towards the region of highest intensity, the beam waist. A 100 mw laser focused to a spot size of 1μm diameter has an electric field magnitude of about $|E|=10^7$V/m. A CdSe NC with diameter a=10nm and dielectric $\varepsilon=10$, has a polarizability $\alpha = \frac{\varepsilon - 1}{\varepsilon + 2} a^3 \varepsilon_0$ of approximately 10^{-35} Fm^2. These values give a trap depth of about 6meV. We do not expect this to be deep enough since it is small compared to thermal energy at room temperature kT=25meV. Since α scales like a^3, it becomes increasing difficult to trap smaller particles. We conclude that it is very difficult to use the simple optical tweezer setup that we described to trap NCs.

Appendix D

Matlab Code

This appendix includes some of the key matlab code used to produce many of the figures in this thesis.

D.1 Chapter 2 code

```
% For calibrating the efficiency of the optical detection as a function
of wavelength

clear all;

dark = 73;
cen = {'640'; '550'; '460'};

lambdamax = [705.60 616.57 527.47];
lambdamin = [572.77 481.89 391.07];

for I = 1:length(lambdamax),
    dlambda(I) = (lambdamax(I)-lambdamin(I))/1339;
    lambda(I,:) =(lambdamin(I):dlambda(I):lambdamax(I));
end

%Wavelength Calibration
load mercury460t1s.txt;
load mercury550t1s.txt;
load mercury640t1s.txt;

mer460=mercury460t1s(3:end)-dark;
mer550=mercury550t1s(3:end)-dark;
mer640=mercury640t1s(3:end)-dark;

%The line wavelengths from HG-1
mer_lines = [404.7 435.8 546.1 577.0 579.1 696.5];

figure(1);
splot(lambda(1,:),mer640);
splot(lambda(2,:),mer550);
splot(lambda(3,:),mer460);
xlabel('Wavelength (nm)');
```

```
ylabel('Intensity');
title('Measured Mercury/Argon Lines');

% To find the peak positions
[Y,I]=max(mer460(1:400));
mline(1)=lambda(3,I);
[Y,I]=max(mer460);
mline(2)=lambda(3,I);
[Y,I]=max(mer550);
mline(3)=lambda(2,I);
[Y,I]=max(mer640(1:60));
mline(4)=lambda(1,I);
[Y,I]=max(mer640(1:200));
mline(5)=lambda(1,I);
[Y,I]=max(mer640(200:end));
mline(6)=lambda(1,I+200);
mline-mer_lines
mline
mer_lines
mean(mline-mer_lines)

% Intensity Calibration
load cal460t10s.txt;
load cal550t10s.txt;
load cal640t5s.txt;
cal460=cal460t10s(3:end)-dark;
cal550=cal550t10s(3:end)-dark;
cal640=2*(cal640t5s(3:end)-dark);

%---------------- Efficiency Data for Calibration ---------------------

% Actual spectrum for the LS1CAL with cc3 diffuser on SMA connector
ls1lam = [350 360 370 380 390 400 420 440 460 480 500 525 550 575 600
650 700 750];
ls1cc3 = [0.0761 0.0930 0.1238 0.1796 0.259 0.333 0.566 0.880 1.31 1.72
2.06 2.79 3.57 4.50 5.52 7.40 9.95 13.95];
%ls1amp1 = [1.56 2.01 3.33 5.24 7.82 9.43 11.6 15.3 19.9 25.1 31.3 47.0
64.7];
ls1cal_fit = polyfit(ls1lam,ls1cc3,9);

figure(2);
splot(lambda(1,:),cal640);
splot(lambda(2,:),cal550);
splot(lambda(3,:),cal460);
splot(lambda(1,:),3500*polyval(ls1cal_fit,lambda(1,:)));
splot(lambda(2,:),3500*polyval(ls1cal_fit,lambda(2,:)));
splot(lambda(3,:),3500*polyval(ls1cal_fit,lambda(3,:)));
xlabel('Wavelength (nm)');
ylabel('Intensity');
title('Measured LS1-CAL');

lam = (400:25:700);
pts = [1500 1500 1650 1950 2300 2700 3050 3150 3350 3600 3900 4100
3900];
eff_fit = polyfit(lam,pts,7);
```

```
figure(3);
splot(lambda(1,:),cal640./polyval(ls1cal_fit,lambda(1,:)));
splot(lambda(2,:),cal550./polyval(ls1cal_fit,lambda(2,:)));
splot(lambda(3,:),cal460./polyval(ls1cal_fit,lambda(3,:)));
splot(lam,pts,'o');
splot(lambda(1,:),polyval(eff_fit,lambda(1,:)));
splot(lambda(2,:),polyval(eff_fit,lambda(2,:)));
splot(lambda(3,:),polyval(eff_fit,lambda(3,:)));
xlabel('Wavelength (nm)');
ylabel('Relative Efficiency');
title('CC3 diffuser on 600um fiber');
axis([400 700 0 4500]);

mnorm = max(cal640);

figure(4);
subplot(1,2,1);
splot(lambda(1,:),cal640./mnorm,'r');
splot(lambda(2,:),cal550./mnorm,'g');
splot(lambda(3,:),cal460./mnorm,'b');
splot(lambda(1,:),3500*polyval(ls1cal_fit,lambda(1,:))./mnorm,'k');
splot(lambda(2,:),3500*polyval(ls1cal_fit,lambda(2,:))./mnorm,'k');
splot(lambda(3,:),3500*polyval(ls1cal_fit,lambda(3,:))./mnorm,'k');
xlabel('Wavelength (nm)');
ylabel('Intensity');
title('LS1-CAL');
axis([400 700 0 1]);

nnorm = max(polyval(eff_fit,lambda(1,:)));

subplot(1,2,2);
splot(lambda(1,:),cal640./polyval(ls1cal_fit,lambda(1,:))./nnorm,'r');
splot(lambda(2,:),cal550./polyval(ls1cal_fit,lambda(2,:))./nnorm,'g');
splot(lambda(3,:),cal460./polyval(ls1cal_fit,lambda(3,:))./nnorm,'b');
%splot(lam,pts,'ko');
splot(lambda(1,:),polyval(eff_fit,lambda(1,:))./nnorm,'k');
splot(lambda(2,:),polyval(eff_fit,lambda(2,:))./nnorm,'k');
splot(lambda(3,:),polyval(eff_fit,lambda(3,:))./nnorm,'k');
xlabel('Wavelength (nm)');
ylabel('Relative Efficiency');
title('Optical Detection System');
axis([400 700 0 1]);
```

```
% Verifies that my data processing is correct by converting the
theoretical blackbody spectrum from wavelength to energy

clear all;
clf;

h = 6.626e-34; % m^2kg/s
c = 3e8; % m/s
k = 1.3807e-23; %j/K
```

```
T = 3000; %K
kT = k*T;
meV = 1.60e-22; % meV expressed in joules

lambda = (600:200:3800)*1e-9;
freq = (1:10:1000)*1e12;

lambda_fine = (10:10:5000)*1e-9;

% Theoretical Black body as a function of lambda
Slam = 8*pi*h*c./(lambda.^5.*(exp((h*c)./(lambda*kT))-1));
Slam_fine = 8*pi*h*c./(lambda_fine.^5.*(exp((h*c)./(lambda_fine*kT))-
1));
% Theoretical Black body as a function of frequency
Sfreq = 8*pi*h.*freq.^3./(c^3*(exp((h.*freq)./kT)-1));

% Now lets convert lambda to freq
Lfreq = c./lambda;
lcorr = lambda.^2;
SLfreq = lcorr.*Slam;

figure(1);
subplot(1,3,1);
%bar(lambda*1e6, Slam./max(Slam),1,'w');
vwhist(lambda*1e6, Slam./max(Slam));
hold on;
plot(lambda_fine*1e6,Slam_fine./max(Slam_fine), 'r');
xlabel('Wavelength (um)');
ylabel('Normalized Intensity');
title('Spectrometer');
axis([0 4 0 1]);

subplot(1,3,2);
vwhist(Lfreq*h/meV,Slam./max(Slam));
hold on;
plot(freq*h/meV,Sfreq./max(Sfreq), 'r');
xlabel('Energy (meV)');
title('Incorrect Method');
axis([0 3000 0 1]);

subplot(1,3,3);
vwhist(Lfreq*h/meV,SLfreq./max(SLfreq));
hold on;
plot(freq*h/meV,Sfreq./max(Sfreq), 'r');
xlabel('Energy (meV)');
title('Correct Method');
axis([0 3000 0 1]);
```

```
% For processing experimental data

clear all;
clf;
```

```
colors = {'r'; 'm'; 'g'; 'c'; 'b'; 'k'; 'r'; 'm'; 'g'; 'c'; 'b'; 'k';
'r'; 'm'; 'g'; 'c'; 'b'; 'k'};

hbar = 1.055e-34; % js
c = 3.00e8; % m/s
meV = 1.60e-22; % meV expressed in joules
kB = 0.0863; %meV/K

% For kaiser filtering to smooth data
N = 31;
Bet = 5;

% load all of the data files into dat
colorstring = {'qdot655'; 'qdot605'; 'qdot585'; 'qdot565'; 'qdot545'};
condstr = {'p'; 'a'};

tempstr = {'300'; '260'; '230'; '200'; '170'; '140'; '120'; '100';
'80'; '60'; '50'; '40'; '30'; '20'; '5'};
temp = [300 260 230 200 170 140 120 100 80 60 50 40 30 20 5];

% Use this for all - second set of 605 data
lambdamax = [705.60 666.04 641.30 621.51 606.67];
lambdamin = [572.77 532.37 507.13 486.94 471.80];


%---------------- Efficiency Data for Calibration --------------------

% This is calculated in precal.m in the calibration directory
% eff_fit is the efficiency of the total diffuser/fiber/spectrometer
system
lam = (400:25:700);
pts = [1500 1500 1650 1950 2300 2700 3050 3150 3350 3600 3900 4100
3900];
eff_fit = polyfit(lam,pts,7);

% So, in order to correctly calibrate data, need to divide by
polyval(eff_fit,lambda)
% And this needs to be done while in lambda, before converting to
energy

% data processing
for I=1:length(colorstring),

   % Note that the way that I calculate lambda is an approximation,
   % in reality dlambda varies by 5% from beginning to the end
   dlambda(I) = (lambdamax(I)-lambdamin(I))/1339;
   lambda_dummy =(lambdamin(I):dlambda(I):lambdamax(I));
   lambda(I,:) = lambda_dummy(3:end); % because there is some funny
business with the first 4 points
   energy(I,:) = 2*pi*hbar*c./(meV*1e-9*lambda(I,:)); % meV

   % there is a distortion when converting to energy since dl/dE is not
constant
```

```
   % So, need to multiply signal by lcorr when converting to energy
   lcorr = lambda(I,:).^2; % See blackbody program to verify this is
correct

   for J=1:length(condstr),

      % Just take average value of dark, since it is flat
      dummy = load([colorstring{I} '/d300.txt']);
      dark = mean(dummy(5:end));

      length(colorstring)-I

      for K=1:length(tempstr),

         if (condstr{J}=='p'), % for PL

           dummy = load([colorstring{I} '/' condstr{J} tempstr{K}
'.txt']);
           pl = dummy(5:end)-dark;

           % This is a better place to do the convolution
            pl = convolution(dummy(5:end)-dark,kaiser(N,Bet));

           %I convolve with a kaiser window to smooth data, and divide
by efficiency of system
           ldat(I,K,J,:) = pl./polyval(eff_fit,lambda(I,:));
           lam_emi = pl./polyval(eff_fit,lambda(I,:));
           edat(I,K,J,:) = lcorr.*pl./polyval(eff_fit,lambda(I,:));
           ene_emi = lcorr.*pl./polyval(eff_fit,lambda(I,:));

           % Full Width Half Max
           dum = fwhm(lam_emi,lambda(I,:));
           pl_lam_center(I,K) = dum(2);
           pl_lam_width(I,K) = dum(1);

           % Full Width Half Max
           dum = fwhm(ene_emi,energy(I,:));
           pl_center(I,K) = dum(2);
           pl_width(I,K) = dum(1);

           figure(I);
           splot(energy(I,:),ene_emi/(max(ene_emi))-0.5*K,'g');
           xlabel('Energy (meV)');

           figure(99);
           if temp(K)==300,
               subplot(1,2,2);
               splot(energy(I,:),ene_emi/(max(ene_emi))-I,'g');
               xlabel('Energy (meV)');
               title('T=300K');
               axis([1750 2650 -5.2 0.2]);
           elseif temp(K)==5,
               subplot(1,2,1);
               splot(energy(I,:),ene_emi/(max(ene_emi))-I,'g');
```

```
            xlabel('Energy (meV)');
            ylabel('Luminscence & Absorbance (au)');
            title('T=5K');
            axis([1750 2650 -5.2 0.2]);
        end

        if ((temp(K) == 300) && (I == 5))
            qdot545pl300 = ene_emi;
            save ../../simulation/qdot545pl300 qdot545pl300;
            qdot545energy = energy(I,:);
            save ../../simulation/qdot545energy qdot545energy;
        end

        if ((temp(K) == 5) && (I == 5))
            qdot545pl5 = ene_emi;
            save ../../simulation/qdot545pl5 qdot545pl5;
            qdot545energy = energy(I,:);
            save ../../simulation/qdot545energy qdot545energy;
        end

    end

    if (condstr{J}=='a'), % for absorption

        tempstr{K}

        %Need this for absorption data processing
        dummy_white = load([colorstring{I} '/w300.txt']);
        white = dummy_white(5:end)-dark; % since first two numbers
don't mean anything

        dummy = load([colorstring{I} '/' condstr{J} tempstr{K}
'.txt']);
        abs = dummy(5:end)-dark;
        % normalize abs to account for refletions
        absorb = abs*mean(white(1300:end))/mean(abs(1300:end));

        ab = -1*log10(absorb./white);
        ldat(I,K,J,:) = -1*log10(absorb./white);

        % TO SUBTRACT SCATTERING BACKGROUND
        if (1)
        if (temp(K)>180),
            scat1 = mean(ab(1288:1338));
            scat2 = mean(ab(1108:1158));
            scat_slope = (scat2-scat1)/180
            ab = ab-(length(absorb):-1:1)*scat_slope;
        else
            scat1 = mean(ab(1300:1338));
            scat2 = mean(ab(950:988));
            scat_slope = (scat2-scat1)/350
            ab = ab-(length(absorb):-1:1)*scat_slope;
        end

        if (temp(K)==300),
```

```
              figure(50);
              hold on;
              plot(lambda(I,:),ab/max(ab)-0.5*I,'b');
             end

             end

             % fitting 2 gaussians....
            OPTIONS =
optimset('MaxFunEvals',1e4,'MaxIter',2000,'TolFun',1e-7);
            OPTIONS =
optimset('MaxFunEvals',1e4,'MaxIter',2000,'TolFun',1e-6);

            % Fits for different colors
             if (colorstring{I} == 'qdot605'),
                 if (temp(K)>110),
                   ptest = [0.5 0.5 2 25 40 100 2100 2220 2300];
                 else
                   ptest = [0.5 0.5 2 25 40 100 2150 2250 2350];
                 end
            end

            if (colorstring{I} == 'qdot655'),
                 if (temp(K)>110),
                   ptest = [0.5 0.5 2 25 40 100 1950 2050 2200];
                 else
                   ptest = [0.5 0.5 2 25 40 100 2000 2100 2200];
                 end
            end
            if (colorstring{I} == 'qdot545'),
                 if (temp(K)>110),
                   ptest = [0.5 2 40 100 2400 2700];
                 else
                   ptest = [0.5 2 40 100 2450 2750];
                 end
            end
            if (colorstring{I} == 'qdot585'),
                 if (temp(K)>110),
                   ptest = [0.5 2 40 100 2250 2400];
                 else
                   ptest = [0.5 2 40 100 2300 2450];
                 end
            end
            if (colorstring{I} == 'qdot565'),
                 if (temp(K)>110),
                   ptest = [0.5 2 40 100 2300 2500];
                 else
                   ptest = [0.5 2 40 100 2350 2550];
                 end
            end


             pfit =
lsqcurvefit('afun2',ptest,energy(I,:)',ab',[],[],OPTIONS)
            abs_width(I,K)=pfit(length(ptest)/3+1)*2.3548; % to convert
from sigma to fwhm
```

```
            abs_center(I,K)=pfit(length(ptest)*2/3+1);
            abs_center2(I,K)=pfit(length(ptest)*2/3+2);


            figure(I);
            hold on;
            plot(energy(I,:),ab/max(ab)-0.5*K,'b');
            plot(energy(I,:),afun2(pfit,energy(I,:)')/max(ab)-
0.5*K,'r');

            figure(99);
            if temp(K)==300,
                subplot(1,2,2);
                splot(energy(I,:),ab/max(ab)-I,'b');
                splot(energy(I,:),afun2(pfit,energy(I,:)')/max(ab)-
I,'r');
            elseif temp(K)==5,
                subplot(1,2,1);
                splot(energy(I,:),ab/max(ab)-I,'b');
                splot(energy(I,:),afun2(pfit,energy(I,:)')/max(ab)-
I,'r');
            end

            figure(98);
            axis([1750 2650 -5.2 0.2]);
            if temp(K)==300,
                splot(energy(I,:),ab/max(ab)-I,'b');
                splot(energy(I,:),afun2(pfit,energy(I,:)')/max(ab)-
I,'r');
            end


          if (temp(K)==300)
              figure(55);
              hold on;
              plot(energy(I,:),ab,colors{I});
              xlabel('Energy (mev)');
              ylabel('Optical Density');
          end

          if ((temp(K) == 300) && (I == 5))
              qdot545abs300 = ab;
              save ../../simulation/qdot545abs300 qdot545abs300;
              qdot545energy = energy(I,:);
              save ../../simulation/qdot545energy qdot545energy;
          end

          if ((temp(K) == 5) && (I == 5))
              qdot545abs5 = ab;
              save ../../simulation/qdot545abs5 qdot545abs5;
              qdot545energy = energy(I,:);
              save ../../simulation/qdot545energy qdot545energy;
          end
        end
      end
```

```
   end
end

% SAVING DATA

if (0)
data_temp = temp;
save data_temp data_temp;
save ../../simulation/data_temp data_temp;
save pl_lam_width pl_lam_width;
save pl_lam_center pl_lam_center;
save lambda lambda;
save ldat ldat; % data in lambda
save energy energy;
save edat edat;
save pl_width pl_width;
save pl_center pl_center;
save abs_width abs_width;
save abs_center abs_center;
save abs_center2 abs_center2;
save ../../simulation/pl_width pl_width;
save ../../simulation/pl_center pl_center;
save ../../simulation/abs_width abs_width;
save ../../simulation/abs_center abs_center;
end

if (0)
    for I=1:9,
        figure(50+I);
        plot(temp,pfit_save(1,:,I));
    end
end

%NEED to save data in simulation folder in order to compare to theory
fwid_temp = temp;
fwid = pl_width;
for I=1:length(colorstring),
    stokes(I,:) = abs_center(I,:)-pl_center(I,:);
end

save ../../simulation/stokes stokes;
save ../../simulation/fwid_temp fwid_temp;
save ../../simulation/fwid fwid;

% PLOTTING DATA

if (0)
    figure(13);
    for I=1:length(colorstring),
        splot(temp,pl_width(I,:),[colors{I} 'o-']);
    end
    xlabel('Temperature (K)');
    ylabel('Linewidth (meV)');
end
```

```
if (0)
    figure(23);
    errorbar(temp,abs_width(1,:),-1,1,'rx-');
    xlabel('Temperature (K)');
    ylabel('Linewidth (meV)');
end

end
```

```
function g = afun2(params,x)
% called from data_fit
% for some stupid reason need to lump everything in terms of params

num = length(params);
N = (num)/3;

amp = params(1:N);
sig = params((N+1):2*N);
cen = params((2*N+1):3*N);

y = (ones(length(x),1)*amp).*...
   (1./(ones(length(x),1)*sig).*sqrt(2*pi)).*...
   exp(-((x*ones(1,length(amp))-
ones(length(x),1)*cen)./((ones(length(x),1)*sig).*sqrt(2))).^2);

g = sum(y,2);
```

```
% Important - I don't compare neighboring samples
% This will give erratic results if data is not smoothed

function fw = fwhm(y, x)
% for calculating linewidth

left = 0;
right = 0;

for I = 1:(length(y)-2),
   if ((y(I)<max(y)/2) & (y(I+2)>=max(y)/2))
        left = I+1;
   elseif ((y(I)>max(y)/2) & (y(I+2)<=max(y)/2))
      right = I+1;
   end
end

fw(1)=x(left)-x(right); % fwhm
fw(2)=(x(right)+x(left))/2; % center
```

```
% For calculating the various contributions to dE/dT for CdSe and
```

```
% PbS NCs

clear all;

% Fundamental Constants
h = 6.62e-34; %js
me = 9.1e-31; %kg
kB = 0.0863; %meV/K

% ----------------- CdSe NCs ----------------------------------
r = 1:.1:5;

bulk_coulomb_energy = 15; %meV
% I'll assume that this scales like 1/R, and in bulk R=5.6nm
coulomb_energy = 15*5.6./r; %meV

% First get an estimate for the confinement energy
Ebulk300 = 1750; %meV at 300K - DOUBLE CHECK WITH CARDONA
energy = radius_to_energy(r); %meV
Econfinement = energy - Ebulk300 - coulomb_energy;

% Bulk CdSe
dEdT_bulk = -0.36*ones(1,length(r)); %meV/K - according to Cardona

% Thermal Expansion
coeff_thermal_expansion = 5e-6; %/K
dEdT_thermal_expansion = -2*coeff_thermal_expansion*Econfinement;

% Effective Mass - using k.p theory (see notebook 3/27/06 p28)
% Should really use dmdT for 100-300K, which will be bigger
dmdT = -0.039/200; %/K
dEdT_effective_mass = -1*dmdT*Econfinement;

% Dielectric Change - from Nomura
epsilon300 = 9.64;
epsilon100 = 9.17;
% energy goes like 1/epsilon
dEdT_dielectric = (coulomb_energy-bulk_coulomb_energy).*(1-
(epsilon300/epsilon100))./200;

% Exciton-LO phonon - see Goupalov, Citrin, Nanotechnology
n300 = 1/(exp(26/(kB*300))-1); % LO population at 300K
n100 = 1/(exp(26/(kB*100))-1);
dopt = 5*r/7; %meV
Bopt = -1*dopt./sqrt(n300*(n300+1));
dEdT_exciton_LOphonon = Bopt*(n300-n100)/200;

% Total is just the sum
dEdT_tot = dEdT_bulk + dEdT_thermal_expansion + dEdT_effective_mass +
dEdT_dielectric + dEdT_exciton_LOphonon;

% Plot results
figure(1);
plot(r,dEdT_bulk,'b-');
```

```
hold on;
plot(r,dEdT_thermal_expansion,'b-');
plot(r,dEdT_effective_mass,'b:');
plot(r,dEdT_exciton_LOphonon,'b-.');
plot(r,dEdT_dielectric,'b--');
JackKnife(r,dEdT_tot-dEdT_effective_mass/2,dEdT_effective_mass/2);
plot(r,dEdT_tot,'k');
plot(r,dEdT_bulk,'b--');
xlabel('Radius (nm)');
ylabel('dE/dT (meV/K)');
title('CdSe NCs');

% NEED TO ADD EXPERIMENTAL RESULTS
rlow = [3.5 2.2 1.7 1.5 1.35];
rhi = [4.3 2.6 2.2 2.0 1.8];
rave = 0.5*(rlow+rhi);
rdif = 0.5*(rhi-rlow);
dEdT_CdSe = -1*[0.3591 0.3478 0.3448 0.3445 0.3530];
plot(rave,dEdT_CdSe,'ro');
```

```
% To calculate the expected d%Econf/dT for different materials

temp = 0:1:300;

% Data for PbS from Olkhovets
PbSdat = [     1          494.591158      373.218673
     2          558.112384      283.292383
     3          648.576538      250.859951
     4          783.826297      163.882064
     5          812.494814      172.727273
     6          878.736442      157.985258
     7          825.870315      149.140049
     8          633.918568      131.449631
     9          786.390179      138.820639
    10          1027.861776      128.501229
    11          850.503530      115.233415
    12          820.493893      107.862408
    13          817.818821      82.800983
    14          919.843958      56.265356
    15          1115.298215      78.378378
    16          1014.522561      62.162162
    17          988.361219      51.842752
    18          648.576538      228.746929
    19          1031.223895      23.832924
    20          1048.200170      0.245700
    21          1141.087029      -15.970516
    22          1097.235244      -60.196560
    23          1343.480449      -35.135135
    24          1330.382721      3.194103
    25          1352.283827      7.616708
    26          1506.156700      -69.041769
    27          1576.615098      -85.257985
    28          2047.320394      -79.361179
    29          2157.137550      -60.196560
```

```
   30          2094.660167      -18.918919
   31          3181.630815      -10.073710
   32          4282.631270      -10.073710];

E_PbS = PbSdat(:,2); % meV
dEdT_PbS = PbSdat(:,3); %meV/K

% ---------- PbS ------------------
Ebulk = 263 + sqrt(400 + 0.265*temp.^2); %meV
Ebulk0 = 263 + sqrt(400 + 0.265*0.^2);

% From Landolt Bornstein
mnperp = (10.6*(Ebulk0./Ebulk) + 1.9).^-1;
mnpara = (5.8*(Ebulk0./Ebulk) + 3.7).^-1;
mpperp = (10.6*(Ebulk0./Ebulk) + 2.7).^-1;
mppara = (5.8*(Ebulk0./Ebulk) + 3.7).^-1;

% This is the mass that should be used for exciton confinement energy -
see
% journal p 56  5/10/06
% para and perp relative to major axis
mPbS = 1./((2./mnperp) + (1./mnpara) + (2./mpperp) + (1./mppara));

for I=1:(length(temp) - 1),
    % This is the percentage change in mPbS per Kelvin
   dmPbSdT(I) = (mPbS(I+1) - mPbS(I))/((temp(I+1)-temp(I)) *
mPbS(I+1));
   dEdT_bulk_PbS(I) = (Ebulk(I+1) - Ebulk(I))/(temp(I+1)-temp(I));
end

if (0)
figure(1);
plot(temp(2:end),dmPbSdT);
xlabel('Temperature (K)');
ylabel('Percentage change in mass per K');
title('PbS');

figure(11);
plot(temp(2:end),dEdT_bulk_PbS);
xlabel('Temperature (K)');
ylabel('dE/dT (meV/K)');
title('PbS');

dEdT_bulk_PbS(end)
end
% ------------------------------------

% &&&&&&&&&& PbSe &&&&&&&&&&&&&&&&&&&&
Ebulk = 125 + sqrt(400 + 0.256*temp.^2); %meV
Ebulk0 = 125 + sqrt(400 + 0.256*0.^2);

% From Landolt Bornstein
mnperp = (20.7*(Ebulk0./Ebulk) + 4.3).^-1;
mnpara = (11.4*(Ebulk0./Ebulk) + 2.9).^-1;
mpperp = (20.7*(Ebulk0./Ebulk) + 8.7).^-1;
```

```
mppara = (11.4*(Ebulk0./Ebulk) + 3.3).^-1;

% This is the mass that should be used for exciton confinement energy -
see
% journal p 56  5/10/06
mPbSe = 1./((2./mnperp) + (1./mnpara) + (2./mpperp) + (1./mppara));

for I=1:(length(temp) - 1),
    % This is the percentage change in mPbS per Kelvin
   dmPbSedT(I) = (mPbSe(I+1) - mPbSe(I))/((temp(I+1)-temp(I)) *
mPbSe(I+1));
   dEdT_bulk_PbSe(I) = (Ebulk(I+1) - Ebulk(I))/(temp(I+1)-temp(I));
end

if (0)
figure(2);
plot(temp(2:end),dmPbSedT);
xlabel('Temperature (K)');
ylabel('Percentage change in mass per K');
title('PbSe');

figure(12);
plot(temp(2:end),dEdT_bulk_PbSe);
xlabel('Temperature (K)');
ylabel('dE/dT (meV/K)');
title('PbSe');

dEdT_bulk_PbSe(end)
end

% &&&&&&&&&&&&&&&&&&&&&&&&&&&&&&&&&&&&&&&&&&&&

% Wise's data for PbS and PbSe
% Cet size <--> energy conversion for PbSe from APL 71 (1997) p3406
% The weird energy dependence is from this paper.
E_PbSe = [600 750 700 1000 1200]; % meV
R_PbSe = [8 7 5.5 3.5 1.8]/2; % nm
dEdT_PbSe = [140 115 50 -5 -55]; % ueV/K
dEdT_PbSe_bulk = 500; % ueV/K
dmdT_PbSe300 = 1200e-6; % /K
Ebulk_PbSe300 = 278; %meV
Econf_PbSe = E_PbSe - Ebulk_PbSe300;
dEdTcorrection_PbSe = 1000*Econf_PbSe.*dmdT_PbSe300;  % ueV/K

% use values from beginning of program
%E_PbS = [500 550 650 800 840 910 1030 1060 1100 2100]; % meV
%dEdT_PbS = [375 280 250 170 160 50 130 0 -60 -70]; % ueV/K
dEdT_PbS_bulk = 510; % ueV/K
dmdT_PbS300 = 850e-6; % /K
Ebulk_PbS300 = 410; %meV
Econf_PbS = E_PbS - Ebulk_PbS300;
dEdTcorrection_PbS = 1000*Econf_PbS.*dmdT_PbS300;  % ueV/K

% My experiment - from data/qdot/data_plot
dEdT_CdSe = [0.3591 0.3478 0.3448 0.3445 0.3530];
```

```
Econf_CdSe = [186.1261  317.7040  435.4482  515.6562  597.1329];
dEdT_CdSe_bulk = 0.36;

if (0)

% -------------- Try presenting d%Econf/dT ----------

figure(6);
h = plot(Econf_InAs,1,'k<');
hold on;
set(h,'MarkerFaceColor','k');
h = plot(Econf_InGaAs,1,'k>');
set(h,'MarkerFaceColor','k');
h = plot(Econf_GaAs,ones(1,3),'k^');
set(h,'MarkerFaceColor','k');

h = plot(Econf_CdSe,dEdT_CdSe./dEdT_CdSe_bulk,'ko');
set(h,'MarkerFaceColor','k');

% This is to make the legend work out correctly
h = plot(E_PbS(1)-Ebulk_PbS300,dEdT_PbS(1)/dEdT_PbS_bulk,'ks');
set(h,'MarkerFaceColor','k');
h = plot(E_PbS(1)-
Ebulk_PbS300,(dEdT_PbS(1)+dEdTcorrection_PbS(1))/dEdT_PbS_bulk,'ks');
set(h,'MarkerFaceColor','w');
h = plot(E_PbSe(1)-Ebulk_PbSe300,dEdT_PbSe(1)/dEdT_PbSe_bulk,'kd');
set(h,'MarkerFaceColor','k');
h = plot(E_PbSe(1)-
Ebulk_PbSe300,(dEdT_PbSe(1)+dEdTcorrection_PbSe(1))/dEdT_PbSe_bulk,'kd'
);
set(h,'MarkerFaceColor','w');

for I = 1:length(E_PbS),
    if (E_PbS(I)<1200)
h = plot(E_PbS(I)-Ebulk_PbS300,dEdT_PbS(I)/dEdT_PbS_bulk,'ks');
set(h,'MarkerFaceColor','k');
h = plot(E_PbS(I)-
Ebulk_PbS300,(dEdT_PbS(I)+dEdTcorrection_PbS(I))/dEdT_PbS_bulk,'ks');
set(h,'MarkerFaceColor','w');
    end
end

for I = 1:length(E_PbSe),
    if (E_PbSe(I)<1000)
h = plot(E_PbSe(I)-Ebulk_PbSe300,dEdT_PbSe(I)/dEdT_PbSe_bulk,'kd');
set(h,'MarkerFaceColor','k');
h = plot(E_PbSe(I)-
Ebulk_PbSe300,(dEdT_PbSe(I)+dEdTcorrection_PbSe(I))/dEdT_PbSe_bulk,'kd'
);
set(h,'MarkerFaceColor','w');
    end
end

h = plot(Econf_CdSe,dEdT_CdSe./dEdT_CdSe_bulk,'ko');
set(h,'MarkerFaceColor','k');
```

```
plot((1:5000),ones(1,5000));
xlabel('Confinement Energy (meV)');
ylabel('(dE_N_C/dT)/(dE_b_u_l_k/dT)');
axis([0 1000 -0.5 2.5]);
legend('InAs','InGaAs','GaAs','CdSe','PbS','modified
PbS','PbSe','modified PbSe','Location','NorthWest');
```

D.2 Chapter 3 code

```
% To calculate the Stokes shift for Gaussian distribution

clear all;

load pl_center.mat;
load abs_center.mat;

% Fundamental Constants
k = 0.0863; %meV/K

colors = {
    'r'; 'm'; 'g'; 'b'; 'k'; 'r'; 'm'; 'g'; 'c'; 'b'; 'k'; 'r'; 'm';
'g'; 'c'; 'b'; 'k'; };
num_replicas=10;
Eo = 26; % meV
Se = 0.45;
Sa = 0.14;
temp = [5 20 30 40 50 60 80 100 120 140 170 200 230 260 300];
temp_rev = [300 260 230 200 170 140 120 100 80 60 50 40 30 20 5];

%From NC_radius program

r = [4.10 2.41 1.99 1.69 1.47];

    % CALCULATION OF BROADENING/STOKES SHIFT DUE TO OPTICAL PHONON
REPLICAS
    n = 1./(exp(Eo./(k.*temp))-1);

    emi_replica_shift = zeros(1,length(temp));
    abs_replica_shift = zeros(1,length(temp));

    % This will give the shift from the ZPL due to phonon replicas
    for I = (-1*num_replicas):num_replicas,
        emi_replica_shift = emi_replica_shift + Eo*I*exp(-1*Se*(2*n +
1)).*besseli(I,2*Se*sqrt(n.*(n+1))).*exp(I*Eo./(2*k*temp));
        abs_replica_shift = abs_replica_shift + Eo*I*exp(-1*Sa*(2*n +
1)).*besseli(I,2*Sa*sqrt(n.*(n+1))).*exp(I*Eo./(2*k*temp));
    end;
```

```
    stokes_replica_shift = abs_replica_shift + emi_replica_shift;

for rad=1:length(r),

    % CALCULATION OF BROADENING/STOKES SHIFT DUE TO ENERGY SUBLEVELS
   d = level0(r(rad));
   ol0=d(1);
   el0=d(2);
   d = level1u(r(rad));
   ol1u=d(1);
   el1u=d(2);
   d = level1l(r(rad));
   ol1l=d(1);
   el1l=d(2);
   d = level2(r(rad));
   ol2=d(1);
   el2=d(2);

   % in order to compare to my 2level fits, I combine levels and drop
dark
   d = levelu_2lev(r(rad));
   ou_2lev = d(1);
   eu_2lev = d(2);
   d = levell_2lev(r(rad));
   ol_2lev = d(1);
   el_2lev = d(2);

   % For presentation plot - This is made up
   edark_3lev = -3;
   odark_3lev = 0.005;

     % Calculate the probability of energy level occupation
     Ptot = exp(-el0./(k.*temp)) + exp(-el1u./(k.*temp)) + exp(-
el1l./(k.*temp)) + exp(-el2./(k.*temp));
     Pl0 = exp(-el0./(k.*temp))./Ptot;
     Pl1l = exp(-el1l./(k.*temp))./Ptot;
     Pl1u = exp(-el1u./(k.*temp))./Ptot;
     Pl2 = exp(-el2./(k.*temp))./Ptot;

     Ptot_2lev = exp(-el_2lev./(k.*temp)) + exp(-eu_2lev./(k.*temp));
     Pl_2lev = exp(-el_2lev./(k.*temp))./Ptot_2lev;
     Pu_2lev = exp(-eu_2lev./(k.*temp))./Ptot_2lev;

     % Probabilities of emission from sublevels states
     % equals probability of occupation times oscillator strength
     Petot = ol0*Pl0 + ol1l*Pl1l + ol1u*Pl1u + ol2*Pl2;
     Pel0 = ol0*Pl0./Petot;
     Pel1u = ol1u*Pl1u./Petot;
     Pel1l = ol1l*Pl1l./Petot;
     Pel2 = ol2*Pl2./Petot;

     Petot_2lev = ol_2lev*Pl_2lev + ou_2lev*Pu_2lev;
     Pel_2lev = ol_2lev*Pl_2lev./Petot_2lev;
     Peu_2lev = ou_2lev*Pu_2lev./Petot_2lev;
```

```
% Relative oscillator strength
otot = ol0 + ol1u + ol1l + ol2;
rol0 = ol0/otot;
rol1u = ol1u/otot;
rol1l = ol1l/otot;
rol2 = ol2/otot;

otot_2lev = ou_2lev + ol_2lev;
rol_2lev = ol_2lev/otot_2lev;
rou_2lev = ou_2lev/otot_2lev;


plcenter = Pel0*el0 + Pel1u*el1u + Pel1l*el1l + Pel2*el2;
abscenter = el0*rol0 + el1u*rol1u + el1l*rol1l + el2*rol2;
stoke = abscenter - plcenter + stokes_replica_shift;
Stokes_levels = abscenter - plcenter;

plvar = Pel0.*(plcenter-el0).^2 + Pel1u.*(plcenter-el1u).^2 +
Pel1l.*(plcenter-el1l).^2 + Pel2.*(plcenter-el2).^2;
plwidth = sqrt(plvar);

stoke300(rad) = stoke(end);
stoke10(rad) = stoke(1);

Stokes_levels300(rad) = Stokes_levels(end);

if (0)
Stokes_levels_rad = r;
save Stokes_levels300 Stokes_levels300;
save Stokes_levels_rad Stokes_levels_rad;
end

if (1)
figure(1);

plot(temp,plcenter,[colors{rad} '--']);
hold on;
plot(temp,plwidth,colors{rad});
xlabel('Temperature (K)');
ylabel('PL center / Width (meV)');

figure(2);
hold on;
plot(temp,sqrt(30^2+plwidth.^2),colors{rad});
xlabel('Temperature (K)');
ylabel('Linewidth (meV)');

figure(9);
subplot(1,3,3);
plot(temp,plcenter,'k--');
hold on;
plot(temp,abscenter*ones(1, length(temp)),'k:');
plot(300, el0, 'b>');
```

```
 plot(300, el1u, 'g>');
 plot(300, el1l, 'r>');
 plot(300, el2, 'k>');
 xlabel('Temperature (K)');
 ylabel('Emission Energy (meV)');
 axis([0 300 -15 20]);

 subplot(1,3,1);
 plot(temp,Pl0,'b');
 hold on;
 plot(temp,Pl1u,'g');
 plot(temp,Pl1l,'r');
 plot(temp,Pl2,'k');
 xlabel('Temperature (K)');
 ylabel('Probability of Occupation');
 axis([0 300 0 1]);

 subplot(1,3,2);
 plot(temp,Pel0,'b');
 hold on;
 plot(temp,Pel1u,'g');
 plot(temp,Pel1l,'r');
 plot(temp,Pel2,'k');
 plot(300, rol0, 'b>');
 plot(300, rol1u, 'g>');
 plot(300, rol1l, 'r>');
 plot(300, rol2, 'k>');
 xlabel('Temperature (K)');
 ylabel('Probability of Emission');
 axis([0 300 0 1]);

 if (1)
 figure(11);
 plot(temp,Stokes_levels,[colors{rad} '--']);
 hold on;
 stokes_expt_blue = abs_center(5,:)-pl_center(5,:);
 plot(temp_rev,stokes_expt_blue);
xlabel('Temperature (K)');
ylabel('Absolute Stokes Shift (meV)');
title('Only Fine Structure');
 end

 figure(12);
 plot(temp,stoke,colors{rad});
 hold on;
 plot(temp_rev,stokes_expt_blue, 'o-');
xlabel('Temperature (K)');
ylabel('Stokes Shift with Offset(meV)');
title('Qdot545');

figure(13)
subplot(1,3,1);
plot(temp,stoke_2lev,[colors{rad}],'LineWidth',1.5);
hold on;
xlabel('Temperature (K)');
ylabel('Stokes Shift (meV)');
```

```
    title('Fine Structure Theory');
    axis([0 300 0 100]);

    subplot(1,3,2);
    load pl_center;
    load abs_center;
    plot(temp_rev,abs_center(rad,:)-pl_center(rad,:),[colors{rad}
shapes{rad} '-'],'LineWidth',1.5);
    hold on;
    xlabel('Temperature (K)');
    title('Experiment');
    axis([0 300 0 100]);

    % see stokes_2level - These values are using a lsqcurvefit
    osc_2level =  1 - [0.4104
                       0.2055
                       0.5331
                       0.7217
                       0.7484]';
    ene_2level = [53.7167
                  58.4974
                  83.6353
                  89.5679
                  96.4719]';
    stokes_other = 15;
    subplot(1,3,1);
    for I = 1:5,
        hold on;
        % Calculate the probability of energy level occupation
        Ptot = exp(0) + exp(-ene_2level(I)./(k.*temp));
        ProbL = exp(0)./Ptot;
        ProbU = exp(-ene_2level(I)./(k.*temp))./Ptot;

        % Relative oscillator strength
        roscL = osc_2level(I);
        roscU = 1 - osc_2level(I);

        % Probabilities of emission from sublevels states
        % equals probability of occupation times oscillator strength
        Petot = roscL*ProbL + roscU*ProbU;
        PemisL = roscL*ProbL./Petot;
        PemisU = roscU*ProbU./Petot;

        plcenter = PemisU*ene_2level(I);
        abscenter = ene_2level(I)*roscU;
        Stokes_2level = abscenter - plcenter;

        plot(temp, stokes_other + Stokes_2level, [colors{I} '--
'],'LineWidth',1.5);
    end

    subplot(1,3,3);
    % see simulation\citrin for how I got these
    Stokes_ac = [157.6014   64.7394   28.1293   13.9391    7.5704
3.4880    1.8942    0.9665];
```

```
    r_citrin = [11    15    20    25    30    40    50    60]/10;
    Stokes_citrin = interp1(r_citrin,Stokes_ac,r);
    for I = 1:length(r),
        plot(temp,stokes_other +
Stokes_citrin(I)*ones(1,length(temp)),colors{I},'LineWidth',1.5);
        hold on;
    end
    xlabel('Temperature (K)');
    %ylabel('Stokes Shift (meV)');
    title('Acoustic Phonon Scattering');
    axis([0 300 0 100]);

    figure(14);
    subplot(1,3,1);

    % results from stokes_2level using lsqcurvefit
    fw = [62.1000   62.1000   62.2000   62.4000   62.9000   63.8000
64.7000
   78.1000   78.1000   78.1000   78.2000   78.5000   78.8000   79.2000
   91.1000   91.1000   91.1000   91.2000   91.5000   92.1000   92.8000
   89.1000   89.1000   89.1000   89.2000   89.6000   90.4000   91.7000
   89.7000   89.7000   89.7000   89.7000   90.0000   90.5000
91.5000];

    fw_temp = [5    50   100   150   200   250   300];
    plot(fw_temp,fw(1,:),'r','LineWidth',1.5);
    hold on;
    plot(fw_temp,fw(2,:),'m','LineWidth',1.5);
    plot(fw_temp,fw(3,:),'g','LineWidth',1.5);
    plot(fw_temp,fw(4,:),'b','LineWidth',1.5);
    plot(fw_temp,fw(5,:),'k','LineWidth',1.5);
    xlabel('Temperature (K)');
    ylabel('Linewidth FWHM (meV)')
    title('Fine Structure');
    axis([0 300 60 120]);

    subplot(1,3,2);
    load pl_width;
    for rad = 1:length(r),
        plot(temp_rev,pl_width(rad,:),[colors{rad} shapes{rad} '-
'],'LineWidth',1.5);
        hold on;
    end
    xlabel('Temperature (K)');
    %ylabel('Linewidth FWHM (meV)');
    title('Experiment');
    axis([0 300 60 120]);

    subplot(1,3,3);
    % these parameters are from simulation\citrin
    A = [25.3209   13.6170    7.6596    4.9021    3.4043    1.9149
1.2255    0.8511];
    hw = [8.1363    5.7283    4.1714    3.4480    3.0616    2.1025
1.5858    1.4989];
    r_citrin = [11    15    20    25    30    40    50    60]/10;
    inhomo = [61 76 90 85 83]/2.35;
```

```
    for num = 1:length(r),
        Ao = interp1(r_citrin,A,r(num));
        hwo = interp1(r_citrin,hw,r(num));
        plot(temp,2.35*sqrt((Ao*sqrt(coth(hwo./(2*k*temp)))).^2 +
inhomo(num)^2),colors{num},'LineWidth',1.5);
        hold on;
    end;
    xlabel('Temperature (K)');
    %ylabel('Linewidth FWHM (meV)');
    title('Acoustic Phonon');
    axis([0 300 60 120]);

    end
end

figure(30)
plot(r,stoke300,'r');
hold on;
plot(r,stoke10,'b');
xlabel('Radius (nm)');
ylabel('Stokes Shift (meV)');
title('At T=10,300K');
```

```
data_plot.m

clear all;
clf;

colors = {'r'; 'm'; 'g'; 'b'; 'k'; 'r'; 'm'; 'g'; 'c'; 'b'; 'k'; 'r';
'm'; 'g'; 'c'; 'b'; 'k'};
shapes = {'o'; 'x'; '+'; '*'; 's'};
colorstring = {'qdot655'; 'qdot605'; 'qdot585'; 'qdot565'; 'qdot545'};
tempstr = {'300'; '260'; '230'; '200'; '170'; '140'; '120'; '100';
'80'; '60'; '50'; '40'; '30'; '20'; '5'};
condstr = {'p'; 'a'};

% LOADING DATA

load data_temp data_temp;
temp = data_temp;
temp = [300 260 230 200 170 140 120 100 80 60 50 40 30 20 5];

load  pl_lam_width pl_lam_width;
load  pl_lam_center pl_lam_center;

load  lambda lambda;
load  ldat ldat; % data in lambda

load  energy energy;
load  edat edat;

load  pl_width pl_width;
load  pl_center pl_center;
```

```
load  abs_width abs_width;
load  abs_center abs_center;
load  abs_center2 abs_center2;

% PLOTTING DATA

if (0)
for I=1:length(colorstring),
   for J=1:length(condstr),
      for K=1:length(tempstr),
         if (condstr{J}=='p'),
          figure(I);
           splot(energy(I,:),ene_emi/(max(ene_emi))-0.5*K,'g');
           xlabel('Energy (meV)');
         end
         if (condstr{J}=='a'),

           figure(I);
           hold on;
          plot(energy(I,:),ab/max(ab)-0.5*K,'b');
          plot(energy(I,:),afun2(pfit,energy(I,:)')/max(ab)-0.5*K,'r');
         end
      end
   end
end
end

if (1)
    figure(13);
    for I=1:length(colorstring),
%        splot(temp,abs_width(I,:),[colors{I} 'x-']);
        splot(temp,pl_width(I,:),[colors{I} 'o-']);
    end
    xlabel('Temperature (K)');
    ylabel('Linewidth (meV)');
end

if (1)
    figure(53);
    for I=1:length(colorstring),
%        splot(temp,abs_width(I,:),[colors{I} 'x-']);
        splot(temp,-pl_lam_width(I,:)+pl_lam_width(I,1),[colors{I} 'o-
']);
    end
    xlabel('Temperature (K)');
    ylabel('Linewidth FWHM (nm)');
end

if (1)
    figure(63);
    for I=1:length(colorstring),
%        splot(temp,abs_width(I,:),[colors{I} 'x-']);
        splot(temp,-pl_lam_width(I,:),[colors{I} shapes{I} '-
'],'LineWidth',1.5);
    end
    xlabel('Temperature (K)');
```

```
    ylabel('Linewidth FWHM (nm)');
end

if (1)
    figure(73);
    for I=1:length(colorstring),
%        splot(temp,abs_width(I,:),[colors{I} 'x-']);
        splot(temp,pl_lam_center(I,:)-pl_lam_center(I,1),[colors{I}
shapes{I} '-'],'LineWidth',1.5);
    end
    xlabel('Temperature (K)');
    ylabel('Emission Wavlength (nm)');
end

if (0)
    figure(23);
    errorbar(temp,abs_width(1,:),-1,1,'rx-');
    xlabel('Temperature (K)');
    ylabel('Linewidth (meV)');
end

% from "Properties of Wide Bandgap II-VI Semiconductors p 33-36
Eo=1849; %meV CdSe(cubic) at T=0K
hw=25.4; %meV
S=2.94;
kB=8.617e-2; %meV/K
Eg=Eo-S*hw*(coth(hw./(temp.*2*kB))-1); %meV

if (1)
    figure(14);
    for I=1:length(colorstring),
        splot(temp,abs_center(I,:),[colors{I} 'x-']);
        splot(temp,pl_center(I,:),[colors{I} 'o-']);
    end
%    splot(temp,Eg,'kx-');
    xlabel('Temperature (K)');
    ylabel('Center (meV)');
end

if (1)
    figure(15);
    subplot(1,3,1);
    for I=1:length(colorstring),
        splot(temp,abs_center(I,:)-pl_center(I,:),[colors{I} shapes{I}
'-'],'LineWidth',1.5);
    end
    xlabel('Temperature (K)');
    ylabel('Stokes Shift (meV)');
    axis([0 300 0 100]);

    subplot(1,3,2);
    for I=1:length(colorstring),
        splot(temp,pl_width(I,:),[colors{I} shapes{I} '-
'],'LineWidth',1.5);
    end
    xlabel('Temperature (K)');
```

```
    ylabel('Linewidth FWHM (meV)');
    axis([0 300 60 120]);

    subplot(1,3,3);
    for I=1:length(colorstring),
        splot(temp,pl_center(I,:)-pl_center(I,1),[colors{I} shapes{I}
'-'],'LineWidth',1.5);
    end
    xlabel('Temperature (K)');
    ylabel('PL center (meV)');
    axis([0 80 66 82]);

    figure(35);
    for I=1:length(colorstring),
        splot(temp,abs_center(I,:)-pl_center(I,:)-(abs_center(I,end)-
pl_center(I,end)),[colors{I} shapes{I} '-'],'LineWidth',1.5);
    end
    xlabel('Temperature (K)');
    ylabel('Stokes Shift (meV)');
    axis([0 300 -20 0]);

end

if (1)
    figure(25);
    subplot(1,3,2);
    for I=1:length(colorstring),
        splot(temp,abs_center(I,:)-pl_center(I,:),[colors{I} shapes{I}
'-'],'LineWidth',1.5);
    end
    xlabel('Temperature (K)');
    ylabel('Stokes Shift (meV)');
    axis([0 300 0 100]);

    subplot(1,3,1);
    splot(temp,0.5*(abs_center(1,:)-abs_center(1,1) + abs_center2(1,:)-
abs_center2(1,1)),[colors{1} shapes{1} '-'],'LineWidth',1.5);
    for I=2:5,
        splot(temp,abs_center(I,:)-abs_center(I,1),[colors{I} shapes{I}
'-'],'LineWidth',1.5);
    end
    xlabel('Temperature (K)');
    ylabel('Absorption Center (meV)');
    axis([0 300 0 90]);

    subplot(1,3,3);
    for I=1:length(colorstring),
        splot(temp,pl_center(I,:)-pl_center(I,1),[colors{I} shapes{I}
'-'],'LineWidth',1.5);
    end
    xlabel('Temperature (K)');
    ylabel('PL center (meV)');
    axis([0 80 66 82]);

end
```

```
if (1)
    figure(16);
    for I=1:length(colorstring),
        splot(temp,abs_center(I,:)-abs_center(I,1),[colors{I} 'x-']);
    end
%    splot(temp,Eg-Eg(1),'kx-');
    xlabel('Temperature (K)');
    ylabel('Abs Center (meV)');
end

if (1)
    figure(26);
    for I=1:length(colorstring),
        splot(temp,pl_center(I,:)-pl_center(I,1),[colors{I} 'o-']);
    end
%    splot(temp,Eg-Eg(1),'kx-');
    xlabel('Temperature (K)');
    ylabel('PL Center (meV)');
end

if (0)
    figure(17);
    for I=1:length(colorstring),
        splot(temp,pl_3qcenter(I,:)-pl_qcenter(I,:),[colors{I} 'o-']);
    end
    xlabel('Temperature (K)');
    ylabel('Skewness (meV)');
end

if (0)
    figure(18);
    for I=1:length(colorstring),
        splot(temp,pl_1twidth(I,:),[colors{I} 'o-']);
    end
    xlabel('Temperature (K)');
    ylabel('Full Width 1/10 Max (meV)');
end

if (0)
figure(3);
plot(temp,2.355*pfit_save(1,:,3),'go-');
hold on;
plot(temp,2.355*pfit_save(2,:,3),'bo-');
xlabel('Temperature (K)');
ylabel('FWHM (meV)');
end

% For PL and absorption
if (0)
for I=1:length(colorstr),
   figure(60);
   subplot(2,2,1);
    for J=1:length(tempstr),
```

```
    splot(energy(I,:),convertdat(I,J,2,edat));
    end
    xlabel('Energy (meV)');
   ylabel('Normalized Absorption');
   axis([1750 2200 -0.2 1.2]);
    subplot(2,2,2);
    for J=1:length(tempstr),

splot(energy(I,:),convertdat(I,J,1,edat)/max(convertdat(I,J,1,edat)));
    end
    xlabel('Energy (meV)');
   ylabel('Normalized PL');
   axis([1750 2200 -0.2 1.2]);
    subplot(2,2,3);
    splot(temp,fw_pl(I,:),'b-');
%   splot(temp,fw_abs(I,:),'g-');
   xlabel('Temperature (K)');
    ylabel('FWHM Linewidth (meV)');
    subplot(2,2,4);
    splot(temp,cen_pl(I,:),'b-');
%   splot(temp,cen_abs(I,:),'g-');
   xlabel('Temperature (K)');
    ylabel('Peak Center (meV)');
end
end

if (0)
for I=1:length(colorstr),
   figure(I);
   subplot(2,2,1);
    xlabel('Energy (meV)');
    ylabel('Absorption (au)');
    subplot(2,2,2);
    for J=1:length(tempstr),

splot(energy(I,:),convertdat(I,J,1,edat)/max(convertdat(I,J,1,edat)));
    end
    xlabel('Energy (meV)');
    ylabel('PL (au)');
    subplot(2,2,3);
    splot(temp,fw_pl(I,:),'b-');
%   splot(temp,fw_abs(I,:),'g-');
   xlabel('Temperature (K)');
    ylabel('FWHM Linewidth (meV)');
    subplot(2,2,4);
    splot(temp,cen_pl(I,:),'b-');
%   splot(temp,cen_abs(I,:),'g-');
   xlabel('Temperature (K)');
    ylabel('Peak Center (meV)');
end
end

if (1)
    figure(36);
    for I=2:5,
        splot(temp,abs_center(I,:)-abs_center(I,1),[colors{I} 'x-']);
```

```
    end
    splot(temp,0.5*(abs_center(1,:)-abs_center(1,1)+abs_center2(1,:)-
abs_center2(1,1)),'kx-');
    xlabel('Temperature (K)');
    ylabel('Abs Center (meV)');
end
```

```
% This is a simulation of the Stokes shift given a 2 level model

clear all;

colors = {'r' 'm' 'g' 'b' 'k'};

% The Stokes shift for my smallest NC sample is 88meV at T=40K.
% About 20 meV of this is expected to be from optical phonons (15 meV)
and
% inhomogeneous size distribution (5 meV), so need to explain 68meV.

% Assuming only 2 levels, try to find the energy level spacing and
% oscillator strength that maximize the Stokes shift at RT

%r = [1.47 1.69 1.99 2.41 4.10]; %nm
r = [4.10 2.41 1.99 1.69 1.47]; %nm
Stokes_300 = [  32.5842
                25.6220
                55.4230
                73.9551
                81.6467]'; %meV

Stokes_40 =    [ 36.9699
                 28.3386
                 59.9279
                 80.5875
                 87.8841]';

Stokes_change = Stokes_40 - Stokes_300;
%Stokes_change = 6*ones(1,5); %meV from T=40K -> T=300K

Stokes_other = 15; %meV due to inhomo and optical phonons, etc
Stokes_fine40 = Stokes_40 - Stokes_other;

% Fundamental Constants
k = 0.0863; %meV/K


temp = 10:10:300;


if (0)

for K=1:length(r),
```

```
    Stokes_best = zeros(1,length(temp));
    Energy_best = 0;
    Osc_best = 0;

    for I=5:1:150,
        for J=0.01:0.01:0.8,

            % ENERGY SUBLEVELS
            % lower
            energyL = 0;
            oscL = J;
            % uppper
            energyU = I; %meV
            oscU = (1-J);

            % Calculate the probability of energy level occupation
            Ptot = exp(-energyL./(k.*temp)) + exp(-energyU./(k.*temp));
            ProbL = exp(-energyL./(k.*temp))./Ptot;
            ProbU = exp(-energyU./(k.*temp))./Ptot;

            % Relative oscillator strength
            otot = oscL + oscU;
            roscL = oscL/otot;
            roscU = oscU/otot;

            % Probabilities of emission from sublevels states
            % equals probability of occupation times oscillator
strength
            Petot = roscL*ProbL + roscU*ProbU;
            PemisL = roscL*ProbL./Petot;
            PemisU = roscU*ProbU./Petot;


            plcenter = PemisL*energyL + PemisU*energyU;
            abscenter = energyL*roscL + energyU*roscU;
            Stokes_levels = abscenter - plcenter;


            if ((Stokes_levels(4) < Stokes_fine40(K)+0.5) &&
(Stokes_levels(4) > Stokes_fine40(K)-0.5))
                if ((Stokes_levels(1)-Stokes_levels(end) >
Stokes_change(K)-0.5) && (Stokes_levels(1)-Stokes_levels(end) <
Stokes_change(K)+0.5))
                    Stokes_best = Stokes_levels;
                    Energy_best = I;
                    Osc_best = J;
                end
            end

        end
    end

    energy(K) = Energy_best
```

```
    osc(K) = Osc_best

    if (1)
    figure(20)
    hold on;
    plot(temp, Stokes_best + Stokes_other);
    xlabel('Temperature (K)');
    ylabel('Stokes shift due to levels (meV)');
    end

end


figure(1)
subplot(1,2,1)
plot(r,energy,'bo-', 'LineWidth', 1.5);
xlabel('Radius (nm)');
ylabel('Energy (meV)');

subplot(1,2,2)
plot(r,osc,'ro-', 'LineWidth', 1.5);
hold on;
plot(r,1-osc,'bo-', 'LineWidth', 1.5);
xlabel('Radius (nm)');
ylabel('Oscillator Strength');


end



% First plot the theoretical predictions

r = (12:50)/10; % NC radius in angstroms

for I=1:length(r),
   d = levelu_2lev(r(I));
   ou_2lev(I) = d(1);
   eu_2lev(I) = d(2);
   d = levell_2lev(r(I));
   ol_2lev(I) = d(1);
   el_2lev(I) = d(2);
end

otot = ol_2lev + ou_2lev;

if (0)
figure(1);
subplot(1,2,2);
hold on;
splot(r,ol_2lev./otot,'r', 'LineWidth', 1.5);
splot(r,ou_2lev./otot,'b', 'LineWidth', 1.5);
xlabel('Radius (nm)');
ylabel('Oscillator Strength');
```

```
subplot(1,2,1);
hold on;
splot(r,el_2lev,'r', 'LineWidth', 1.5);
splot(r,eu_2lev,'b', 'LineWidth', 1.5);
xlabel('Radius (nm)');
ylabel('Energy (meV)');
axis([1 5 -10 110]);
end;


if (0)
    % Try to figure out what the linewidth broadening is

   dE = 0.1;
   ene = -150:dE:150; %meV
   width = [62 78 91 89 89.5];

   temp = [5 50 100 150 200 250 300];

   for I=1:5,
    for J = 1:length(temp),
        % ENERGY SUBLEVELS
        % lower
        energyL = 0;
        oscL = osc(I);
        % uppper
        energyU = energy(I); %meV
        oscU = 1-osc(I);

        % Calculate the probability of energy level occupation
        Ptot = exp(-energyL./(k.*temp(J))) + exp(-
energyU./(k.*temp(J)));
        ProbL = exp(-energyL./(k.*temp(J)))./Ptot;
        ProbU = exp(-energyU./(k.*temp(J)))./Ptot;

        % Relative oscillator strength
        otot = oscL + oscU;
        roscL = oscL/otot;
        roscU = oscU/otot;

        % Probabilities of emission from sublevels states
        % equals probability of occupation times oscillator strength
        Petot = roscL*ProbL + roscU*ProbU;
        PemisL = roscL*ProbL./Petot;
        PemisU = roscU*ProbU./Petot;

        pl = gauss(PemisL(end),ene',width(I)/2.35,energyL) +
gauss(PemisU(end),ene',width(I)/2.35,energyU);

        if (temp(J) == 300)
            pl300(I,:) = pl;
        end
```

```
        if (temp(J) == 5)
            pl5(I,:) = pl;
        end



        if (0)
        figure(11);
        splot(ene,pl);
        xlabel('Energy (meV)');
        ylabel('Emission');
        title('T=300K');
        end

        dum=fwhm(pl);
        fw(I,J) = dum(1)*dE;

        if (J==length(temp))
            figure(22);
            splot(ene,pl,[colors{I}],'Linewidth',1.5);
            xlabel('Energy (meV)');
            ylabel('Emission');
            title('T=300K');
        end

    end
   end
   fwhm(gauss(1,ene',width(1)/2.35,0))
end



if (0)

figure(12);
plot(temp,fw(1,:),'r','Linewidth',1.5);
hold on;
plot(temp,fw(2,:),'m','Linewidth',1.5);
plot(temp,fw(3,:),'g','Linewidth',1.5);
plot(temp,fw(4,:),'b','Linewidth',1.5);
plot(temp,fw(5,:),'k','Linewidth',1.5);
xlabel('Temperature (K)');
ylabel('linewidth FWHM (meV)')
title('Broadening due to Fine Structure');
axis([0 300 60 120]);

% Try to figure out what the absorption would look like

ene = -200:1:200; %meV

figure(15);
hold on;
for I=1:5,
```

```
    abs = gauss(osc(I),ene',width(I)/2.35,0) + gauss((1-
osc(I)),ene',width(I)/2.35,energy(I));
    plot(ene,abs,[colors{I}],'Linewidth',1.5);
    dum = fwhm(abs);
    fw_abs = dum(1)*dE;
end
xlabel('Energy (meV)');
ylabel('Absorption');
title('Absorption assuming only fine structure');
axis([-100 200 0 0.012]);

figure(16);
load qdot545abs300;
load qdot545pl300;
load qdot545energy;
plot(qdot545energy,1.25*qdot545abs300./max(qdot545abs300),'b','Linewidt
h',1);
hold on;
plot(qdot545energy,qdot545pl300./max(qdot545pl300),'g','Linewidth',1.5)
;
I = 5;
abs = gauss(osc(I),ene',width(I)/2.35,0) + gauss((1-
osc(I)),ene',width(I)/2.35,energy(I));
plot(2261+ene,abs./max(abs),'r--','Linewidth',1.5);
plot(2261 + (-150:dE:150),pl300(I,:)./max(pl300(I,:)),'k--
','Linewidth',1.5);
xlabel('Energy (meV)');
ylabel('Absorption & Emission');
title('T=300K');
axis([2100 2600 -0.2 1.2]);

figure(17);
load qdot545abs5;
load qdot545pl5;
load qdot545energy;
plot(qdot545energy,1.2*qdot545abs5./max(qdot545abs5),'b','Linewidth',1)
;
hold on;
plot(qdot545energy,qdot545pl5./max(qdot545pl5),'g','Linewidth',1.5);
I = 5;
abs = gauss(osc(I),ene',width(I)/2.35,0) + gauss((1-
osc(I)),ene',width(I)/2.35,energy(I));
plot(2341 + ene,abs./max(abs),'r--','Linewidth',1.5);
plot(2341 + (-150:dE:150),pl5(I,:)./max(pl5(I,:)),'k--
','Linewidth',1.5);
xlabel('Energy (meV)');
ylabel('Absorption & Emission');
title('T=5K');
axis([2100 2600 -0.2 1.2]);

figure(18);
subplot(1,2,1);
plot(qdot545energy,1.2*qdot545abs5./max(qdot545abs5),'b','Linewidth',1)
;
hold on;
plot(qdot545energy,qdot545pl5./max(qdot545pl5),'g','Linewidth',1.5);
```

```
I = 5;
abs = gauss(osc(I),ene',width(I)/2.35,0) + gauss((1-
osc(I)),ene',width(I)/2.35,energy(I));
plot(2341 + ene,abs./max(abs),'r--','Linewidth',1.5);
plot(2341 + (-150:dE:150),pl5(I,:)./max(pl5(I,:)),'k--
','Linewidth',1.5);
xlabel('Energy (meV)');
ylabel('Absorption & Emission');
title('T=5K');
axis([2100 2600 -0.2 1.2]);

subplot(1,2,2);
plot(qdot545energy,1.25*qdot545abs300./max(qdot545abs300),'b','Linewidt
h',1);
hold on;
plot(qdot545energy,qdot545pl300./max(qdot545pl300),'g','Linewidth',1.5)
;
I = 5;
abs = gauss(osc(I),ene',width(I)/2.35,0) + gauss((1-
osc(I)),ene',width(I)/2.35,energy(I));
plot(2261+ene,abs./max(abs),'r--','Linewidth',1.5);
plot(2261 + (-150:dE:150),pl300(I,:)./max(pl300(I,:)),'k--
','Linewidth',1.5);
xlabel('Energy (meV)');
ylabel('Absorption & Emission');
title('T=300K');
axis([2100 2600 -0.2 1.2]);

figure(19);
plot(qdot545energy, 1.2 +
1.2*qdot545abs5./max(qdot545abs5),'b','Linewidth',1);
hold on;
plot(qdot545energy, 1.2 +
qdot545pl5./max(qdot545pl5),'g','Linewidth',1.5);
I = 5;
abs = gauss(osc(I),ene',width(I)/2.35,0) + gauss((1-
osc(I)),ene',width(I)/2.35,energy(I));
plot(2340 + ene, 1.2 + abs./max(abs),'r--','Linewidth',1.5);
plot(2340 + (-150:dE:150), 1.2 + pl5(I,:)./max(pl5(I,:)),'k--
','Linewidth',1.5);


plot(qdot545energy,1.25*qdot545abs300./max(qdot545abs300),'b','Linewidt
h',1);
hold on;
plot(qdot545energy,qdot545pl300./max(qdot545pl300),'g','Linewidth',1.5)
;
I = 5;
abs = gauss(osc(I),ene',width(I)/2.35,0) + gauss((1-
osc(I)),ene',width(I)/2.35,energy(I));
plot(2263+ene,abs./max(abs),'r--','Linewidth',1.5);
plot(2263 + (-150:dE:150),pl300(I,:)./max(pl300(I,:)),'k--
','Linewidth',1.5);
xlabel('Energy (meV)');
ylabel('Absorption & Emission');
axis([2100 2600 -0.2 2.4]);
```

```
title('R=1.5nm');


end

if (1)
% LEAST SQUARES CURVE FIT

OPTIONS = optimset('MaxFunEvals',1e4,'MaxIter',2000,'TolFun',1e-7);
Stokes_offset = 15;
temp = [300 260 230 200 170 140 120 100 80 60 50 40 30 20 5];
rad = [4.10 2.41 1.99 1.69 1.47]; %nm
load ../data/qdot/pl_center pl_center;
load ../data/qdot/abs_center abs_center;

stokes_data = abs_center - pl_center;
stokes_40to300 = stokes_data(:,1:end-3) - Stokes_offset;
temp_40to300 = temp(1:end-3);

pguess = [80 0.4];

for I=1:5,
    pfit(I,:) =
lsqcurvefit('stoke2lev',pguess,temp_40to300,stokes_40to300(I,:),[],[],O
PTIONS);
    energyU_fit(I) = pfit(I,1);
    oscU_fit(I) = pfit(I,2);
    energyL_fit(I) = 0;
    oscL_fit(I) = 1-pfit(I,2);

end



figure(15);
hold on;
for I=1:5,
    plot(temp_40to300,stokes_40to300(I,:) + Stokes_offset,'o');
    plot(temp,stoke2lev(pfit(I,:),temp) + Stokes_offset,'-');
end
xlabel('Temperature (K)');
ylabel('Stokes Shift (meV)');
axis([0 300 0 100]);

figure(16);
subplot(1,2,2);
hold on;
splot(rad,oscL_fit,'ro-', 'LineWidth', 1.5);
splot(rad,oscU_fit,'bo-', 'LineWidth', 1.5);
splot(r,ol_2lev./otot,'r', 'LineWidth', 1.5);
splot(r,ou_2lev./otot,'b', 'LineWidth', 1.5);
xlabel('Radius (nm)');
ylabel('Oscillator Strength');
```

```
subplot(1,2,1);
hold on;
%splot(rad,energyL_fit,'r-', 'LineWidth', 1.5);
splot(rad,energyU_fit,'bo-', 'LineWidth', 1.5);
splot(r,el_2lev,'r', 'LineWidth', 1.5);
splot(r,eu_2lev,'b', 'LineWidth', 1.5);
xlabel('Radius (nm)');
ylabel('Energy (meV)');
axis([1 5 -10 110]);

figure(17);
subplot(1,2,2);
hold on;
splot([rad(1) rad(3:5)],[oscL_fit(1) oscL_fit(3:5)],'ro-', 'LineWidth',
1.5);
splot([rad(1) rad(3:5)],[oscU_fit(1) oscU_fit(3:5)],'bo-', 'LineWidth',
1.5);
%splot(rad(2),oscL_fit(2),'ro', 'LineWidth', 1.5);
%splot(rad(2),oscU_fit(2),'bo', 'LineWidth', 1.5);
splot(r,ol_2lev./otot,'r', 'LineWidth', 1.5);
splot(r,ou_2lev./otot,'b', 'LineWidth', 1.5);
xlabel('Radius (nm)');
ylabel('Oscillator Strength');

subplot(1,2,1);
hold on;
splot([rad(1) rad(3:5)],[energyL_fit(1) energyL_fit(3:5)],'r-',
'LineWidth', 1.5);
splot([rad(1) rad(3:5)],[energyU_fit(1) energyU_fit(3:5)],'bo-',
'LineWidth', 1.5);
%splot(rad(2),energyU_fit(2),'bo', 'LineWidth', 1.5);
splot(r,el_2lev,'r', 'LineWidth', 1.5);
splot(r,eu_2lev,'b', 'LineWidth', 1.5);
xlabel('Radius (nm)');
ylabel('Energy (meV)');
axis([1 5 -10 110]);
figure(17);



% LINEWIDTH TEMPERATURE DEPENDENCE OF FINE STRUCTURE THEORY

%   d = levelu_2lev(r(I));
%   ou_2lev(I) = d(1);
%   eu_2lev(I) = d(2);
%   d = levell_2lev(r(I));
%   ol_2lev(I) = d(1);
%   el_2lev(I) = d(2);


if (1)
    % Try to figure out what the linewidth broadening is

    colors = {'r' 'm' 'g' 'b' 'k'};
```

```
dE = 0.1;
ene = -100:dE:100; %meV
rad = [4.10 2.41 1.99 1.69 1.47]; %nm

temp = [5 50 100 150 200 250 300];
width = [62 78 91 89 89.5];

for I=1:5,
 for J = 1:length(temp),

      % lower
      energyL = energyL_fit(I);
      oscL = oscL_fit(I);
      % uppper
      energyU = energyU_fit(I);
      oscU = oscU_fit(I);

      % Calculate the probability of energy level occupation
      Ptot = exp(-energyL./(k.*temp(J))) + exp(-
energyU./(k.*temp(J)));
      ProbL = exp(-energyL./(k.*temp(J)))./Ptot;
      ProbU = exp(-energyU./(k.*temp(J)))./Ptot;

      % Relative oscillator strength
      otot = oscL + oscU;
      roscL = oscL/otot;
      roscU = oscU/otot;

      % Probabilities of emission from sublevels states
      % equals probability of occupation times oscillator strength
      Petot = roscL*ProbL + roscU*ProbU;
      PemisL = roscL*ProbL./Petot;
      PemisU = roscU*ProbU./Petot;

      pl =
gauss(PemisL(end),ene',width(I)/2.35,energyL)+gauss(PemisU(end),ene',wi
dth(I)/2.35,energyU);

      if (temp(J) == 300)
          pl300_fit(I,:) = pl;
      end

      if (temp(J) == 5)
          pl5_fit(I,:) = pl;
      end


      figure(11);
      hold on;
      plot(ene,pl,colors{I});
      xlabel('Energy (meV)');
      ylabel('Emission');
      dum=fwhm(pl);
      fw_fit(I,J) = dum(1)*dE;
```

```
    end
   end
end


figure(72);

for I=1:5,
    plot(temp,fw_fit(I,:),[colors{I}],'Linewidth',1.5);
    hold on;
end
xlabel('Temperature (K)');
ylabel('linewidth FWHM (meV)')
title('Broadening due to Fine Structure');
axis([0 300 60 120]);

dE = 1;
ene = -200:dE:200; %meV

figure(15);
hold on;
for I=1:5,
    abs_fit = gauss(oscL_fit(I),ene',width(I)/2.35,energyL_fit(I)) +
gauss(oscU_fit(I),ene',width(I)/2.35,energyU_fit(I));
    plot(ene,abs_fit,[colors{I}],'Linewidth',1.5);
    dum = fwhm(abs_fit);
    fw_abs = dum(1)*dE;
end
xlabel('Energy (meV)');
ylabel('Absorption');
title('Absorption assuming only fine structure');
axis([-100 200 0 0.012]);

figure(96);
load qdot545abs300;
load qdot545pl300;
load qdot545energy;
plot(qdot545energy,1.25*qdot545abs300./max(qdot545abs300),'b','Linewidt
h',1);
hold on;
plot(qdot545energy,qdot545pl300./max(qdot545pl300),'g','Linewidth',1.5)
;
abs_fit = gauss(oscL_fit(5),ene',width(5)/2.35,energyL_fit(5)) +
gauss(oscU_fit(5),ene',width(5)/2.35,energyU_fit(5));
plot(2261 + ene,abs_fit./max(abs_fit),'r--','Linewidth',1.5);
plot(2261 + (-100:0.1:100),pl300_fit(5,:)./max(pl300_fit(5,:)),'k--
','Linewidth',1.5);
xlabel('Energy (meV)');
ylabel('Absorption & Emission');
title('T=300K');
axis([2100 2600 -0.2 1.2]);

figure(97);
load qdot545abs5;
```

```
load qdot545pl5;
load qdot545energy;
plot(qdot545energy,1.2*qdot545abs5./max(qdot545abs5),'b','Linewidth',1)
;
hold on;
plot(qdot545energy,qdot545pl5./max(qdot545pl5),'g','Linewidth',1.5);
plot(2341 + ene,abs_fit./max(abs_fit),'r--','Linewidth',1.5);
plot(2341 + (-100:0.1:100),pl5_fit(5,:)./max(pl5_fit(5,:)),'k--
','Linewidth',1.5);
xlabel('Energy (meV)');
ylabel('Absorption & Emission');
title('T=5K');
axis([2100 2600 -0.2 1.2]);

figure(98);
plot(qdot545energy, 1.2 +
1.2*qdot545abs5./max(qdot545abs5),'b','Linewidth',1);
hold on;
plot(qdot545energy, 1.2 +
qdot545pl5./max(qdot545pl5),'g','Linewidth',1.5);
plot(2340 + ene, 1.2 + abs_fit./max(abs_fit),'r--','Linewidth',1.5);
plot(2340 + (-100:0.1:100), 1.2 + pl5_fit(5,:)./max(pl5_fit(5,:)),'k--
','Linewidth',1.5);
xlabel('Energy (meV)');
ylabel('Absorption & Emission');
axis([2100 2600 -0.2 2.4]);

plot(qdot545energy,1.25*qdot545abs300./max(qdot545abs300),'b','Linewidt
h',1);
hold on;
plot(qdot545energy,qdot545pl300./max(qdot545pl300),'g','Linewidth',1.5)
;
abs_fit = gauss(oscL_fit(5),ene',width(5)/2.35,energyL_fit(5)) +
gauss(oscU_fit(5),ene',width(5)/2.35,energyU_fit(5));
plot(2264 + ene,abs_fit./max(abs_fit),'r--','Linewidth',1.5);
plot(2264 + (-100:0.1:100),pl300_fit(5,:)./max(pl300_fit(5,:)),'k--
','Linewidth',1.5);

end
```

---

citrin.m

```
% To come up with an estimate of the expected linewidth and Stoke's
shfit
% from the plots in Citrin/Goupalov paper - Nanotechnology 12 (2001)
p518

clear all;

kB = 0.0862; %meV/K

% Data points for CdSe NC in SiO2 matrix
```

```
% The T=0 linewidth scales like 1/R2 as Takagahara points out
fwhm_dac_r11_T0 = 64; %meV
fwhm_dac_r60_T0 = 2; %meV
fwhm_dac_r11_T0_GeO2 = 26.5; %meV
fwhm_dac_r60_T0_GeO2 = 0.94; %meV

% The T=300K linewidths
r = [11 15 20 25 30 40 50 60]; % Angstroms
dac_T300 = [(75/1.17) 41 27 19 14 9.5 7 5]; % meV
dac_T300_GeO2 = [(33/1.17) 18 11 8 6.4 4.2 2.6 1.9]; % meV
fwhm_dac_T300 = 2.35*dac_T300; % since Gaussian is assumed
fwhm_dac_T300_GeO2 = 2.35*dac_T300_GeO2; % since Gaussian is assumed

% Choosing something that fits the plots
fwhm_dac_T0 = 7200*r.^-2; %meV
fwhm_dac_T0_GeO2 = 3400*r.^-2; %meV

% Citrin's expression
% for dac^2 ~ Sum(Ai^2*coth(Bi/2)).  I can use data points at T=0 and
T=300
% and assume only 1 mode is relevant.  So fit to dac^2 =
A^2*coth(hw/2kT).

% At T=0, coth(B)=1 so I can solve for A
A = fwhm_dac_T0/2.35;
A_GeO2 = fwhm_dac_T0_GeO2/2.35;

% At non-zero T, hw = 2kT*acoth(dac(T)/A)
hw = 2*kB*300*acoth(fwhm_dac_T300.^2./fwhm_dac_T0.^2);
hw_GeO2 = 2*kB*300*acoth(fwhm_dac_T300_GeO2.^2./fwhm_dac_T0_GeO2.^2);

Stokes_ac = 2*A.^2./hw; %meV
Stokes_ac_GeO2 = 2*A_GeO2.^2./hw_GeO2; %meV

% ******************** LOAD DATA ************************
% Estimates from Norris PRB 53 (1996) p16347
rdat = [3.6 2.6 2.2 2.0 1.8];

% See stokes_figures for 3 papers used to calculate radius
% These are the upper and lower numbers from those papers
rlow = [3.5 2.2 1.7 1.5 1.35];
rhi = [4.3 2.6 2.2 2.0 1.8];
rave = 0.5*(rlow+rhi);
rdif = 0.5*(rhi-rlow);

load gfit_wid.mat;
load lfit_wid.mat;
load gfit_cen.mat;
load lfit_cen.mat;

load abs_center.mat;
load pl_center.mat;

Rguyot = 2.3; %nm - PRB 64 p245342
Wguyot = 18; % meV
```

```
% ***************************************************

temp = 1:1:300;

if (1)
    % OTHER STOKES SHIFT CONTRIBUTIONS ----------------
    Stokes_opt = 15*ones(1,length(r)); %meV - see stokes_theory for
calculation

    % Output from stokes_theory - contribution due to fine structure
    load Stokes_levels_rad.mat;
    load Stokes_levels300.mat;

    % Output from stokes_inhomo - due to inhomogeneous broadening
    load Stokes_inhomo_r.mat;
    load Stokes_inhomo.mat;

    Stokes_tot300 = Stokes_ac + Stokes_opt + Stokes_levels300 +
Stokes_inhomo;

    figure(14);
    plot(r/10,Stokes_ac,'r--');
    hold on;
    plot(r/10,Stokes_opt,'r:');
    plot(r/10,Stokes_levels300,'r-.');
    plot(r/10,Stokes_inhomo,'r-');
    plot(r/10,Stokes_tot300,'k-');
    xlabel('Radius (nm)');
    ylabel('Stokes Shift (meV)');
    axis([1 5 0 100]);
    herrorbar(rave,abs_center(:,1)-pl_center(:,1),rdif,rdif,'x');
    % ------------------------------------------------
end

if(0)
    % &&&&&&&&&&&&&&& PLOT spectra &&&&&&&&&&&&&&&&&&&&&&&&&
    for I = 1:length(r),
        wid = A(I)*sqrt(coth(hw(I)./(2*kB*temp)));

        figure(I);
        plot(temp,wid*1.17);
        xlabel('Temperature (K)');
        ylabel('dac HWHM (meV)');
    end
    % &&&&&&&&&&&&&&&&&&&&&&&&&&&&&&&&&&&&&&&&&&&&&&&&&&&&&&&
end

if (1)

    rx = [15 19 21 24 27 33 44 50];

    fwhm_dac_T0x = interp1(r,fwhm_dac_T0,rx);
    Stokes_acx = interp1(r,Stokes_ac,rx);
    fwhm_dac_T300x = interp1(r,fwhm_dac_T300,rx);
```

```
    for num = (1:length(rx)),

        en = -200:1:200;
        sig_ped = fwhm_dac_T0x(num)/2.35;
        ZPLcen = -0.5*Stokes_acx(num);
        ZPLsig = 1.2;
        ped = (1/(sig_ped*sqrt(2*pi)))*exp(-
((en+ZPLcen)./(sig_ped*sqrt(2))).^2);
        ZPL = (1/(ZPLsig*sqrt(2*pi)))*exp(-(en./(ZPLsig*sqrt(2))).^2);

        pruss = 0.9*ped + 0.1*ZPL;
        prussian_abs = pruss./max(pruss);
        sig = 100/2.35; %meV
        inhom = gauss(1,en',sig,0);
        inhomo = inhom./sum(inhom);
        prussian_c = convolution(prussian_abs,inhomo);
        prussian_conv = prussian_c/max(prussian_c);

        sig_ped300 = fwhm_dac_T300x(num)/2.35;
        ped300 = (1/(sig_ped300*sqrt(2*pi)))*exp(-
((en+ZPLcen)./(sig_ped300*sqrt(2))).^2);
        prussian_c = convolution(prussian_abs,inhomo);
        prussian_conv = prussian_c/max(prussian_c);

        if (0)
        figure(10*num + 1);
        plot(temp,2.35*A(num)*sqrt(coth(hw(num)./(2*kB*temp))));
        xlabel('Temperature (K)');
        ylabel('Linewidth FWHM (meV)');
        axis([0 300 0 70]);
        end

        figure(12);
        subplot(1,2,1);
        axis([-150 150 1 (1+length(rx))]);
        plot(en,0.7*prussian_abs + num);
        hold on;
        plot(en,0.9*prussian_conv + num);

        plot(-en,0.7*prussian_abs + num,'--');
        plot(-en,0.9*prussian_conv + num,'--');
        xlabel('Energy (meV)');
        ylabel('PL Intensity/Absorption (au)');
        title('T=0K');

        % AT T=300K
        subplot(1,2,2);
        axis([-150 150 1 (1+length(rx))]);

        figure(12);
        plot(en,0.7*prussian_abs + num);
        hold on;
        plot(en,0.9*prussian_conv + num);
```

```
        plot(-en,0.7*prussian_abs + num,'--');
        plot(-en,0.9*prussian_conv + num,'--');
        xlabel('Energy (meV)');
        title('T=300K');

        figure(13);
        if rx(num)<25,
            subplot(1,2,1);
            axis([-35 150 0.9 (2+length(rx))/2]);
            plot(en,0.9*prussian_abs - num + 5);
            hold on;
            xlabel('Energy (meV)');
            ylabel('Single Dot Absorption');
        else
            subplot(1,2,2);
            axis([-17.5 75 0.9 (2+length(rx))/2]);
            plot(en,0.9*prussian_abs - num + 9);
            hold on;
            xlabel('Energy (meV)');
        end

        figure(16);
        dum = prussian_abs(end:-1:1).*(1:length(prussian_abs));
        plot(dum);

        figure(17);
        plot(conv(dum,prussian_abs));

        figure(18);

plot(conv(dum,prussian_abs)./(1:length(conv(dum,prussian_abs))));

    end
end

if (0)
    % ^^^^^^^^^^^^^ CALCULATED LINEWIDTH ^^^^^^^^^^^^^^^^^^
% Since I only measure the temperature dependence of dac, and not the
% temperature constant part
figure(17);
plot(r/10,sqrt(fwhm_dac_T300.^2-fwhm_dac_T0.^2),'r--');
xlabel('Radius (nm)');
ylabel('Deconvolution Linewidth FWHM (meV)');
title('Room Temperature Implied Deconvolution Linewidth');

figure(18);
plot(r/10,sqrt(fwhm_dac_T300_GeO2.^2-fwhm_dac_T0_GeO2.^2),'r--');
xlabel('Radius (nm)');
ylabel('Deconvolution Linewidth FWHM (meV)');
title('Room Temperature Implied Deconvolution Linewidth - GeO2');

% Now for optical phonon contribution - dopt = B*sqrt(n(n+1)), B=Bopt*r
hw_opt = 26; %meV

% optical phonon occupation at T=300K
```

```
n300 = 1/(exp(hw_opt/(kB*300))-1);

% From figure 1 plot
Bopt = 4.2/(60*sqrt(n300*(n300+1))); %meV/ang

B = Bopt*r;

fwhm_B300 = B*sqrt(n300*(n300+1))*2.35;

fwhm_temp_tot = sqrt(fwhm_B300.^2+fwhm_dac_T300.^2-fwhm_dac_T0.^2);

figure(17);
hold on;
plot(r/10,fwhm_temp_tot,'k-');
plot(r/10,fwhm_B300,'r:');

if (0)
    herrorbar(rave,gfit_wid(:,1)*2.35,rdif,rdif,'bx');
    herrorbar(rave,lfit_wid(:,1),rdif,rdif,'go');
    axis([1 5 0 100]);
    % Bulk point
    plot(5,31,'k^');
  %  plot(Rguyot,Wguyot,'ks');
end
% ^^^^^^^^^^^^^^^^^^^^^^^^^^^^^^^^^^^^^^^^^^^^^^^^^^^^^^^^^^^^^^^^^^^^^^^^
end

% PLOT THE CONTRIBUTIONS TO LINEWIDTH AT RT
if (0)
    figure(27);
    plot(r/10,sqrt(fwhm_B300.^2+fwhm_dac_T300.^2));
    xlabel('Radius (nm)');
    ylabel('Linewidth FWHM (meV)');
    title('Contributions to Room Temperature Linewidth');
end
```

```
% To get a measure of dE/dT from Cardona paper
% See PRB 34, 2458 (1986)

clear all;

% first index is A exciton, second is B

Eo(1) = 1.834;
Eo(2) = 1.860;

alphaf(1) = 4.24e-4;
alphaf(2) = 4.17e-4;

betaf(1) = 118;
betaf(2) = 93;

temp = [77 200 300];
```

```
for I=1:2,
    Energy(I,:) = Eo(I) + alphaf(I)*temp.^2./(temp + betaf(I));
    dEdT = (Energy(I,1)-Energy(I,3))*1000/223;
end

% This part is to calculate the FWHM of the absorption given the
dielectric
% constant that Cardona measures and

Gamma = 1;
Amp = 0.7;
e0 = 8;

freq0 = 100;
freq = (1:0.1:200);

e2 = e0*Amp*(Gamma/2)^2./((Gamma/2)^2 + (freq - freq0).^2);
e1 = e0*(1 + Amp*(Gamma/2)*(freq-freq0)./((Gamma/2)^2 + (freq -
freq0).^2));

k = imag(sqrt(complex(e1,e2)));

figure(1);
plot(freq,e2);
hold on;
plot(freq,e1,'--');
plot(freq,6*k,'k');
xlabel('Frequency');
ylabel('Amplitude');
axis([80 120 -2 15]);
```

D.3 Chapter 4 code

Bubble_plot_PAM.m

```
% This is to create a bubble plot for 3 colors

clear all;

colors = {'b'; 'g'; 'r'; 'c'; 'm'; 'y'; 'k'};
num_colors = 3;

load (['codes\PAM_3_9']);
Random_codes = PAM_codes;

% NC/noise/microbead characteristics
```

```
small_lambda = 530;
big_lambda = 650;
linewidth = 13; % stdev in nm
cen_sig = 2; % nm
wid_sig = 0.5; % nm
amplitude_error_slope = 0.05; % this is the percentage uncertainty 100
nm away
white_noise_amp = 0.001; % this is the amplitude in a given dlambda bin

% spectrometer characteristics
min_lambda = 450;
max_lambda = 700;
dlambda = 5;
lambda = min_lambda:dlambda:max_lambda;
iter = 30;

% expected center wavelengths
cen = (small_lambda:(big_lambda-small_lambda)/(num_colors-
1):big_lambda)';
wid = linewidth*ones(num_colors,1);

options = optimset('Display','off');

for I=1:length(Random_codes),
    code = Random_codes(I,:)

    for J = 1:iter,
        % make white noise
        white_noise = white_noise_amp*randn(1,length(lambda))';

        % amplitude error
        amp_error_slope = amplitude_error_slope*randn;
        percent_amp_error = 1+(amp_error_slope*(cen-small_lambda)/100);
        amp_error = code'.*percent_amp_error;

        cen_error = cen_sig*(randn(length(cen),1));

        wid_error = wid_sig*(randn(length(cen),1));

        % make noisy photoluminescence
        pl_nn_error =
gauss(amp_error',lambda',(wid+wid_error)',(cen+cen_error)');
        pl_error = pl_nn_error./sum(pl_nn_error);
        pl = white_noise  + pl_error;

        amp_guess = ones(num_colors,1);
        amp_fit =
lsqcurvefit('gauss',amp_guess',lambda',pl./sum(pl),0,1e9,options,wid',c
en');
        normalized_amp = amp_fit/sum(amp_fit);

        if (1)
        figure(11);
        hold on;
        x = (sqrt(3)/2)*(-normalized_amp(1) + normalized_amp(3));
```

```
        y = normalized_amp(2) - 0.5*normalized_amp(1) -
0.5*normalized_amp(3);
        plot(x,y,['.' colors{1+mod(I,length(colors))}]);
        end

        if (0)
        figure(10);
        hold on;
        plot(normalized_amp(2),normalized_amp(3),['o'
colors{1+mod(I,length(colors))}]);
        end
    end
end
```

---

barcode_2level_b.m

```
% This is specifically designed to simulate 2 colors and number of
ratios
% that can be distinguiched for a given error rate.

clear all;

% NC/noise/microbead characteristics
small_lambda = 510;
big_lambda = 580; % NOTE THIS DIFFERENCE!!!
linewidth = 13; % stdev in nm
cen_sig = 0; % nm DIFFERENT
wid_sig = 0; % nm DIFFERENT
amplitude_error_slope = 0.05; % this is the percentage uncertainty 100
nm away
white_noise_amp = 0.001; % this is the amplitude in a given dlambda bin

% spectrometer characteristics
min_lambda = 400;
max_lambda = 750;
dlambda = 5;
lambda = min_lambda:dlambda:max_lambda;

% number of reps per particular barcode
N = 1000;

options = optimset('Display','off');
num_colors = 2;

% expected center wavelengths
cen = (small_lambda:(big_lambda-small_lambda)/(num_colors-
1):big_lambda)';
wid = linewidth*ones(num_colors,1);

level(1) = 2.5;
level_index = 1;

total_amp = dlambda;
```

```
while (level(level_index) > 0),

    for I=1:N,

        % generate code
        code = [level(level_index) (total_amp - level(level_index))]';

        % --------------- GENERATE PL ---------------------------------

        % make white noise
        white_noise = white_noise_amp*randn(1,length(lambda))';

        % amplitude error
        amp_error_slope = amplitude_error_slope*randn;
        percent_amp_error = 1+(amp_error_slope*(cen-small_lambda)/100);
        amp_error = code.*percent_amp_error;

        cen_error = cen_sig*(randn(length(cen),1));
        wid_error = wid_sig*(randn(length(cen),1));

        % make photoluminescence
        pl_nn = gauss(code',lambda',wid',cen');
        pl_no_noise = pl_nn./sum(pl_nn);
        pl_nn_error =
gauss(amp_error',lambda',(wid+wid_error)',(cen+cen_error)');
        pl_error = pl_nn_error./sum(pl_nn_error);
        pl = white_noise  + pl_error;
        noise = pl-pl_no_noise;

        % DECODING BARCODE

        amp_guess = ones(num_colors,1);
        amp_fit = lsqcurvefit('gauss',amp_guess',lambda',pl./sum(pl),-
1e9,1e9,options,wid',cen');
        normalized_amp = (total_amp/sum(amp_fit))*amp_fit;

        % Need to decode
        lev_fit(I) = normalized_amp(1);
    end

    % make next level
    lev_sort = sort(lev_fit);
    level_index = level_index + 1
    level(level_index) = level(level_index - 1) + 2*(lev_sort(5) -
level(level_index - 1))

    [pp,pp_cen] = hist(lev_sort);

    figure(2);
    plot(pp_cen./(5-pp_cen),pp./max(pp));
    hold on;
    xlabel('Ratio');
```

```
    ylabel('Normalized Probability');
    axis([0 1.2 0 1]);

    std(lev_sort)/mean(lev_sort)
end

total_levels = 2*(level_index - 1) - 1
```

---

channel_capacity.m

```
% To estimate the channel capacity of microbead barcodes

clear all;

% NC/noise/microbead characteristics
small_lambda = 530;
big_lambda = 650;
linewidth = 13; % stdev in nm
cen_sig = 2; % nm
wid_sig = 0.5; % nm
amplitude_error_slope = 0.05; % this is the percentage uncertainty 100
nm away
white_noise_amp = 0.001; % this is the amplitude in a given dlambda bin

% spectrometer characteristics
min_lambda = 350;
max_lambda = 700;
dlambda = 5;
lambda = min_lambda:dlambda:max_lambda;

% number of reps per particular barcode
N = 1000;
num_colors = 3;

options = optimset('Display','off');

% initialize variables
failed = 0;
success = 0;
no_code = 0;
total_mse = 0;
rejected = 0;
error_location(num_colors,:) = zeros(1,num_colors);
fft_code = zeros(length(lambda),1);
fft_noise = zeros(length(lambda),1);

% expected center wavelengths
cen = (small_lambda:(big_lambda-small_lambda)/(num_colors-
1):big_lambda)';
wid = linewidth*ones(num_colors,1);

psd_noise = zeros(1,length(lambda))';
psd_amp = zeros(1,length(lambda))';
```

```
psd_wid = zeros(1,length(lambda))';
psd_cen = zeros(1,length(lambda))';
psd_signal = zeros(1,length(lambda))';
psd_wn = zeros(1,length(lambda))';
psd_pl = zeros(1,length(lambda))';

for I=1:N,

    if (mod(I,1000) == 0)
        I
    end

    % generate code
    code = [1 0 0]';

    % --------------- GENERATE PL ------------------------------------

    % make white noise
    white_noise = white_noise_amp*randn(1,length(lambda))';
    psd_wn = psd_wn + abs(fft(white_noise)).^2;

    % amplitude error
    amp_error_slope = amplitude_error_slope*randn;
    percent_amp_error = 1+(amp_error_slope*(cen-small_lambda)/100);
    amp_error = code.*percent_amp_error;

    cen_error = cen_sig*(randn(length(cen),1));
    wid_error = wid_sig*(randn(length(cen),1));

    % make photoluminescence
    pl_nn = gauss(code',lambda',wid',cen');
    pl_no_noise = pl_nn./sum(pl_nn);
    psd_signal = psd_signal + abs(fft(pl_no_noise)).^2;

    pl_nn_error =
gauss(amp_error',lambda',(wid+wid_error)',(cen+cen_error)');
    pl_error = pl_nn_error./sum(pl_nn_error);
    pl = white_noise  + pl_error;
    psd_pl = psd_pl + abs(fft(pl)).^2;
    noise = pl-pl_no_noise;
    psd_noise = psd_noise + abs(fft(noise)).^2;

    pl_nn_amp = gauss(amp_error',lambda',wid',cen');
    pl_amp = pl_nn_amp./sum(pl_nn_amp);
    noise_amp = pl_amp - pl_no_noise;
    psd_amp = psd_amp + abs(fft(noise_amp)).^2;

    pl_nn_cen = gauss(code',lambda',wid',(cen+cen_error)');
    pl_cen = pl_nn_cen./sum(pl_nn_cen);
    noise_cen = pl_cen - pl_no_noise;
    psd_cen = psd_cen + abs(fft(noise_cen)).^2;

    pl_nn_wid = gauss(code',lambda',(wid+wid_error)',cen');
    pl_wid = pl_nn_wid./sum(pl_nn_wid);
```

```
    noise_wid = pl_wid - pl_no_noise;
    psd_wid = psd_wid + abs(fft(noise_wid)).^2;

end

figure(2)
freq = (0:0.04:1);
oscil = (0:25);
semilogy(oscil(2:26),psd_signal(2:26)/N,'b.-');
hold on;
%semilogy(oscil(1:26),psd_pl(1:26)/N,'b:');
%semilogy(oscil(2:26),psd_noise(2:26)/N,'k.-')
%semilogy(oscil(2:26),psd_amp(2:26)/N,'r.-')
%semilogy(oscil(2:26),psd_cen(2:26)/N,'g.-')
%semilogy(oscil(2:26),psd_wid(2:26)/N,'m.-')
semilogy(oscil(2:26),psd_wn(2:26)/N,'c.-')
axis([0 25 1e-6 1]);
xlabel('Frequency (oscillations/spectrometer range)');
ylabel('Average Power Spectrum');

% Calculate channel capacity - the first factor is because I only
transmit
% for a fraction of the time.

capacity = ((big_lambda-small_lambda)/(max_lambda-
min_lambda))*sum(log2(1+(psd_signal(2:26)./psd_noise(2:26))))

wn_capacity = ((big_lambda-small_lambda)/(max_lambda-
min_lambda))*sum(log2(1+(psd_signal(2:26)./psd_wn(2:26))))
```

This is the matlab code to generate the regular PAM codes. The only trick is to make sure that all of the codewords are linearly independent, ie not a multiple of any other code.

Create_PAMnn_files.m

```
% This program is to create the PAM code files for later access

max_num_colors = 16;
max_codes = 5e5;
max_prod = 100;

for colors=12:max_num_colors,
    max_level = 1;
    while(((max_level)^colors < max_codes) && (max_level*colors <
max_prod)),
        [colors, max_level]
        PAMnn_codes = create_PAMnn(colors,max_level);
        length(PAMnn_codes(:,1))
        code_name = ['codes\PAMnn_' int2str(colors) '_'
int2str(max_level)];
        save(code_name, 'PAMnn_codes');
        max_level = max_level + 1;
    end
```

```
end
```

```
function c = create_PAMnn(colors, max_level)

clear PAM_MATRIX;
clear PAM_INDEX;

global PAM_MATRIX;
global PAM_INDEX;

PAM_MATRIX = zeros((max_level+1)^colors,colors);
PAM_INDEX = 1;

make_PAMnn(colors, max_level);

for I=1:(max_level+1)^colors,
    if (sum(PAM_MATRIX(I,:)) ~= 0)
        last_nonzero = I;
    end
end

c = PAM_MATRIX(1:last_nonzero,:);
```

```
function g = make_PAMnn(colors, max_level)

% make PAM with no normalization, so eliminate entries with greatest
common
% factor not equal to one

global PAM_MATRIX;
global PAM_INDEX;

if (colors == 1)
    for J=max_level:-1:0,
        PAM_MATRIX(PAM_INDEX,end) = [J];
        % if the biggest common factor is 0 or 1, then keep it, else
reject
        if (bcf(PAM_MATRIX(PAM_INDEX,1:end)) <= 1)
            PAM_INDEX = PAM_INDEX + 1;
        end
    end
else
    for I = max_level:-1:0,
        PAM_MATRIX((PAM_INDEX:end),(end + 1 - colors)) = I;
        make_PAMnn(colors-1, max_level);
    end
end

g = 1;
```

```
function g = bcf(vec)

% finds the least biggest common factor of a vector of positive
integers

% just to take care of the zero vector
if (sum(abs(vec)) == 0)
    g = 0;
    return
end

sort_vec = sort(vec);

low_ind = 1;
for I=1:length(vec),
    if (sort_vec(I) == 0)
        low_ind = I+1;
    end
end

low = sort_vec(low_ind);
low_factors = sort(factors(low),'ascend');

f = [];

bcf_sofar = 1;
for I = 1:length(low_factors),
    if (sum(mod(vec,low_factors(I))) == 0)
        bcf_sofar = low_factors(I);
    end
end;

g = bcf_sofar;
```

This is the matlab code that generates the codes that have the equal weight and return to 2 zeros constraint. The key point is that I am NOT just inserting 2 zeros between the PAM symbols. I recursively generate all PAM codes that have equal weight AND have <u>at least</u> 2 zeros between non-zero symbols. There is a big difference. The other cases that I presented are easier than this.

```
create_PAM2rtz_files.m

% To create a range of PAM2rtz codes

global PAM_MATRIX;

max_num_colors = 24;
max_codes = 15000;
max_prod = 200;

for colors=14:max_num_colors,
    counts = 1;
```

```
    while((counts*colors < max_prod) && (count_PAM2rtz(colors,counts) <
max_codes)),
        PAM2rtz_codes = create_PAM2rtz(colors,counts);
        code_name = ['codes\PAM2rtz_' int2str(colors) '_'
int2str(counts)];
        save(code_name, 'PAM2rtz_codes');
        counts = counts + 1;
    end
end
```

```
% to recursively calculate the size of a PAM2rtz code

function g = count_PAM2rtz(colors, counts)

if (colors == 1)
    num_codes = 1;
elseif (colors == 2)
    if (counts == 0)
        num_codes = 1;
    else
        num_codes = 2;
    end
elseif (colors == 3)
    if (counts == 0)
        num_codes = 1;
    else
        num_codes = 3;
    end
else
    num_codes = 0;
    for I = counts:-1:0,
        if (I ~= 0)
            num_codes = num_codes + count_PAM2rtz(colors-3, counts-I);
        else
            num_codes = num_codes + count_PAM2rtz(colors-1, counts);
        end
    end
end

g = num_codes;
```

```
function c = create_PAM2rtz(colors, counts)

clear PAM_MATRIX;
clear PAM_INDEX;

global PAM_MATRIX;
global PAM_INDEX;

count_PAM2rtz(colors,counts)

PAM_MATRIX = zeros(count_PAM2rtz(colors,counts),colors);
```

```
PAM_INDEX = 1;

make_PAM2rtz(colors, counts);

c = PAM_MATRIX;
```

```
function g = make_PAM2rtz(colors, counts)

global PAM_MATRIX;
global PAM_INDEX;

if (colors == 1)
    PAM_MATRIX(PAM_INDEX,end) = [counts];
    PAM_INDEX = PAM_INDEX + 1;
elseif (colors == 2)
    if (counts == 0)
        PAM_MATRIX(PAM_INDEX,(end-1:end)) = [0 0];
        PAM_INDEX = PAM_INDEX + 1;
    else
        PAM_MATRIX(PAM_INDEX,(end-1:end)) = [counts 0];
        PAM_INDEX = PAM_INDEX + 1;
        PAM_MATRIX(PAM_INDEX,(end-1:end)) = [0 counts];
        PAM_INDEX = PAM_INDEX + 1;
    end
elseif (colors == 3)
    if (counts == 0)
        PAM_MATRIX(PAM_INDEX,(end-2:end)) = [0 0 0];
        PAM_INDEX = PAM_INDEX + 1;
    else
        PAM_MATRIX(PAM_INDEX,(end-2:end)) = [counts 0 0];
        PAM_INDEX = PAM_INDEX + 1;
        PAM_MATRIX(PAM_INDEX,(end-2:end)) = [0 counts 0];
        PAM_INDEX = PAM_INDEX + 1;
        PAM_MATRIX(PAM_INDEX,(end-2:end)) = [0 0 counts];
        PAM_INDEX = PAM_INDEX + 1;
    end
else
    for I = counts:-1:0,
        if (I ~= 0)
            PAM_MATRIX((PAM_INDEX:end),(end + 1 - colors)) = I;
            PAM_MATRIX((PAM_INDEX:end),(end + 2 - colors)) = 0;
            PAM_MATRIX((PAM_INDEX:end),(end + 3 - colors)) = 0;
            make_PAM2rtz(colors-3, (counts-I));
        else
            PAM_MATRIX((PAM_INDEX:end),(end + 1 - colors)) = 0;
            make_PAM2rtz(colors-1, (counts-I));
        end
    end
end

g = 1;
```

This is the Monte Carlo code generation program.

random_systematic.m

```
% This simulation assumes a variety of noises - white noise, amp, cen,
and
% wid noise and attempts to estimate the number of possible codes

clear all;

% NC/noise/microbead characteristics
small_lambda = 530;
big_lambda = 650;
linewidth = 13; % stdev in nm
cen_sig = 2; % nm
wid_sig = 0.5; % nm
amplitude_error_slope = 0.05; % this is the percentage uncertainty 100
nm away
white_noise_amp = 0.001; % this is the amplitude in a given dlambda bin

% spectrometer characteristics
min_lambda = 450;
max_lambda = 700;
dlambda = 5;
lambda = min_lambda:dlambda:max_lambda;

num_colors = 50;
num_levels = 100;
num_failures = 10000;
mod_num = 7;
iter = 100;

code_name = ['codes\Random_' int2str(small_lambda) 'to'
int2str(big_lambda) '_iter' int2str(iter) '_colors' int2str(num_colors)
'_levels' int2str(num_levels) '_failures' int2str(num_failures)];

% expected center wavelengths
cen = (small_lambda:(big_lambda-small_lambda)/(num_colors-
1):big_lambda)';
wid = linewidth*ones(num_colors,1);

number_failures = 0;
max_number_codes = 1e4;
max_number_attempts = 1e4;

code_matrix = zeros(max_number_codes,num_colors);
pl_matrix = zeros(max_number_codes,length(lambda));
noisy_instances = zeros(iter,length(lambda));
code_index = 1;

failure_tally = zeros(num_failures,1);
attempts_power = ones(mod_num,1);
success_power = ones(mod_num,1);
mse = zeros(iter,1);
```

```
% these are for recording the history of the success rates
hitrate_power = zeros(max_number_attempts,mod_num);
trys_power = zeros(max_number_attempts,mod_num);
index_power = 1;

while (number_failures < num_failures),

    % save as I go
    if (mod(code_index,100) == 0)
        Random_codes = code_matrix(1:code_index-1,:);
        hsuc_power = hsuccess_power(1:index_power-1,:);
        hatt_power = hattempts_power(1:index_power-1,:);
        save(code_name, 'Random_codes', 'hsuc_power', 'hatt_power');
    end

    % record strategy success rates as I go.
    if (mod(sum(attempts_power),100) == 0)
        hsuccess_power(index_power,:) = success_power;
        hattempts_power(index_power,:) = attempts_power;
        index_power = index_power + 1;

        figure(6);
%        plot(hattempts_power(1:index_power-
1,:),hsuccess_power(1:index_power-1,:),'.-');
        plot(hattempts_power(1:index_power-
1,4),hsuccess_power(1:index_power-1,4),'.-');
        xlabel('Attempts');
        ylabel('Successes');
        title('All strategies');

        figure(7);
%        plot(sum(hattempts_power(1:index_power-
1,:),2),sum(hsuccess_power(1:index_power-1,:),2),'.-');
        plot(sum(hattempts_power(1:index_power-
1,4),2),sum(hsuccess_power(1:index_power-1,4),2),'.-');
        xlabel('Attempts');
        ylabel('Successes');
        title('Sum of All strategies');
    end

    % generate code - slightly more complicated, but better way
    nnprob_power = success_power./attempts_power;
    % this is the real probability that I use to choose power
    prob_power = nnprob_power./sum(nnprob_power);
    dum = rand;
    power = 1;
    for I = 1:mod_num,
        if (dum > sum(prob_power(1:I)))
            power = I+1;
        end
    end

    code = floor(num_levels*rand(1,num_colors).^(2^(power-1)));
    while (sum(code) == 0)
```

```
        code = floor(num_levels*rand(1,num_colors).^(2^(power-1)));
    end

    % --------------- GENERATE PL -----------------------------------

    % make no noise pl
    pl_nn = gauss(code,lambda',wid',cen');
    pl_no_noise = pl_nn./sum(pl_nn);

    for I=1:iter,

        % make white noise
        white_noise = white_noise_amp*randn(1,length(lambda))';

        % amplitude error
        amp_error_slope = amplitude_error_slope*randn;
        percent_amp_error = 1+(amp_error_slope*(cen-small_lambda)/100);
        amp_error = code'.*percent_amp_error;

        cen_error = cen_sig*(randn(length(cen),1));

        wid_error = wid_sig*(randn(length(cen),1));

        % make noisy photoluminescence
        pl_nn_error =
gauss(amp_error',lambda',(wid+wid_error)',(cen+cen_error)');
        pl_error = pl_nn_error./sum(pl_nn_error);
        pl = white_noise  + pl_error;

        noisy_instances(I,:) = pl;

    end

    % CHECK IF THIS CODE IS SPACED FAR ENOUGH AWAY
    if (code_index == 1)
        code_matrix(1,:) = code;
        pl_matrix(1,:) = pl_no_noise';
        code_index = code_index + 1;
        code

    else
        I = 1;
        failed = 0;
        mse = sum((noisy_instances - ones(iter,1)*pl_no_noise').^2,2);
        while ((I < code_index) && (failed == 0)),
            % keep going til fail
            code_mse = sum((noisy_instances -
ones(iter,1)*pl_matrix(I,:)).^2,2);
            if (max(mse - code_mse) >= 0)
                failed = 1;
            else
                I = I + 1;
            end
        end
```

```
        if (I == code_index)
            % then this is a good code
            code_matrix(code_index,:) = code;
            pl_matrix(code_index,:) = pl_no_noise';
            code_index = code_index + 1
            failure_tally(number_failures+1) =
failure_tally(number_failures+1) + 1;
            number_failures = 0;
            success_power(power) = success_power(power) + 1;
            %code
        else
            number_failures = number_failures + 1;
        end
    end

end
```

Bibliography

[1] www.evidenttech.com

[2] *Semiconductor and Metal Nanoparticles*. New York: Marcel Dekker, 2004.

[3] A. L. Efros, M. Rosen, M. Kuno, M. Nirmal, D. J. Norris, and M. Bawendi, "Band-edge exciton in quantum dots of semiconductors with a degenerate valence band: Dark and bright exciton states," *Phys. Rev. B*, vol. 54, pp. 4843, 1996.

[4] A. Beveratos, R. Brouri, T. Gacoin, J.-P. Poizat, and P. Grangier, "Nonclassical radiation from diamond nanocrystals," *Phys. Rev. A*, vol. 64, pp. 061802, 2001.

[5] S. Coe-Sullivan, W.-K. Woo, J. S. Steckel, M. Bawendi, and V. Bulovic, "Tuning the performance of hybrid organic/inorganic quantum dot light-emitting devices," *Organic Electronics*, vol. 4, pp. 123, 2003.

[6] D. Loss, G. Burkard, and D. P. D. Vincenzo, "Electron spins in quantum dots as quantum bits," *Journal of Nanoparticle Research*, vol. 2, pp. 401, 2000.

[7], pp. Invensys Westinghouse Rail Systems.

[8] http://ocw.mit.edu/NR/rdonlyres/Electrical-Engineering-and-Computer-Science/6-973Organic-OptoelectronicsSpring2003/, "http://ocw.mit.edu/NR/rdonlyres/Electrical-Engineering-and-Computer-Science/6-973Organic-OptoelectronicsSpring2003/."

[9] Y. Arakawa and H. Sakaki, "Multidimensional quantum well laser and temperature dependence of its threshold current," *Appl. Phys. Lett.*, vol. 40, pp. 939, 1982.

[10] Y. Chan, J.-M. Caruge, P. T. Snee, and M. G. Bawendi, "Multiexcitonic two-state lasing in a CdSe nanocrystal laser," *Appl. Phys. Lett.*, vol. 85, pp. 2460, 2004.

[11] H.-J. Eisler, V. C. Sundar, M. G. Bawendi, M. Walsh, H. Smith, and V. Klimov, "Color-selective semiconductor nanocrystal laser," *App. Phys. Lett.*, vol. 80, pp. 4614, 2002.

[12] A. V. Malko, A. A. Mikhailovsky, M. A. Petruska, J. A. Hollingsworth, H. Htoon, M. G. Bawendi, and V. I. Klimov, "From amplified spontaneous emission to microring lasing using nanocrystal quantum dot solids," *Appl. Phys. Lett.*, vol. 81, pp. 1303, 2002.

[13] M. Arzberger and M. C. Amann, "Homogeneous line broadening in individual semiconductor quantum dots by temperature fluctuations," *Phys. Rev. B*, vol. 62, pp. 11029, 2000.

[14] www.qdots.com

[15] H. Y. Fan, "Temperature Dependence of the Energy Gap in Semiconductors," *Phys. Rev.*, vol. 82, pp. 900, 1951.

[16] S. Nomura and T. Kobayashi, "Exciton-LO-phonon couplings in spherical semiconductor microcrystllites," *Phys. Rev. B*, vol. 45, pp. 1305, 1992.

[17] A. Olkhovets, R.-C. Hsu, A. Lipovskii, and F. W. Wise, "Size-Dependent Temperature Variation of the Energy Gap in Lead-Salt Quantum Dots," *Phys. Rev. Lett.*, vol. 81, pp. 3539, 1998.

[18] G. Ortner, M. Schwab, M. Bayer, R. Passler, S. Fafard, Z. Wasilewski, P. Hawrylak, and A. Forchel, "Temperature dependence of the excitonic band gap in $In_xGa_{1-x}As/GaAs$ self-assembled quantum dots," *Phys. Rev. B*, vol. 72, pp. 085328, 2005.

[19] M. R. Salvador, M. A. Hines, and G. D. Scholes, "Exciton-bath coupling and inhomogeneous broadening in the optical spectroscopy of semiconductor quantum dots," *J. Chem. Phys.*, vol. 118, pp. 9380, 2003.

[20] S. Sanguinetti, E. Poliani, M. Bonfanti, M. Guzzi, E. Grilli, M. Gurioli, and N. Koguchi, "Electron-phonon interaction in individual strain-free $GaAs/Al_{0.3}Ga_{0.7}As$ quantum dots," *Phys. Rev. B*, vol. 73, pp. 125342, 2006.

[21] T. Vossmeyer, L. Katsikas, M. Giersig, I. G. Popovic, K. Diesner, A. Chemseddine, A. Eychmuller, and H. Weller, "CdS Nanoclusters: Synthesis, Characterization, Size Dependent Oscillator Strength, Temperature Shift of the Excitonic Transition Energy, and Reversible Absorbance Shift," *J. Chem. Phys.*, vol. 98, pp. 7665, 1994.

[22] I. I. Zasavitski, E. V. Bushuev, E. A. Andrada-e-Silva, and E. Abramof, "Energy Spectrum of Quantum Wells in PbTe/PbEuTe-Based Structures from Photoluminescence Data," *JETP Letters*, vol. 75, pp. 559, 2002.

[23] T. Liptay and R. Ram, "Temperature dependence of the exciton transition in semiconductor

quantum dots," *App. Phys. Lett.*, vol. 89, pp. 223132, 2006.
[24] D. J. Norris, A. L. Efros, M. Rosen, and M. G. Bawendi, "Size dependence of exciton fine structure in CdSe quantum dots," *Phys. Rev. B*, vol. 53, pp. 16347, 1996.
[25] S. A. Empedocles, D. J. Norris, and M. G. Bawendi, "Photoluminescence Spectroscopy of Single Nanocrystallite Quantum Dots," *Phys. Rev. Lett.*, vol. 77, pp. 3873, 1996.
[26] S. A. Empedocles, R. Neuhauser, K. Shimizu, and M. Bawendi, "Photoluminescence from Single Semiconductor Nanocrystals," *Adv. Mater.*, vol. 11, pp. 1243, 1999.
[27] T. Takagahara, "Electron-phonon interactions in semiconductor nanocrystals," *J. Lumin.*, vol. 70, pp. 129, 1996.
[28] D. M. Mittleman, R. W. Schoenlein, J. J. Shiang, V. L. Colvin, A. P. Alivisatos, and C. V. Shank, "Quantum size dependence of femtosecond electronic dephasing and vibrational dynamics in CdSe nanocrystals," *Phys. Rev. B*, vol. 49, pp. 14435, 1994.
[29] P. Palinginis, S. Tavenner, M. Lonergan, and H. Wang, "Spectral hole burning and zero phonon linewidth in semiconductor nanocrystals," *Phys. Rev. B*, vol. 67, pp. 201307, 2003.
[30] S. V. Goupalov, R. A. Suris, P. Lavallard, and D. S. Citrin, "Exciton Dephasing and Absorption Line Shape in Semiconductor Quantum Dots," *IEEE J. Sel. Top. Quantum Electron.*, vol. 8, pp. 1009, 2002.
[31] M. Han, X. Gao, J. Z. Su, and S. Nie, "Quantum-dot-tagged microbeads for multiplexed optical coding of biomolecules," *nat. biotechnol.*, vol. 19, pp. 631, 2001.
[32] J. Lee, V. C. Sundar, J. R. Heine, M. Bawendi, and K. Jensen, "Full Color Emission from II-VI Semiconductor Quantum Dot-Polymer Composites," *Adv. Mat.*, vol. 12, pp. 1102, 2000.
[33] C. A. Leatherdale, W. K. Woo, F. V. Mikulec, and M. G. Bawendi, "On the absorption cross section of CdSe nanocrystal quantum dots," *J. Phys. Chem. B*, vol. 106, pp. 7619, 2002.
[34] A. Sacra, D. J. Norris, C. B. Murray, and M. G. Bawendi, "Stark spectroscopy of CdSe nanocrystallites: The significance of transition linewidths," *J. Chem. Phys.*, vol. 103, pp. 5236, 1995.
[35] B. O. Dabbousi, J. Rodriguez, F. V. Mikulec, J. R. Heine, H. Mattoussi, R. Ober, K. F. Jensen, and M.G. Bawendi, "(CdSe)ZnS Core-Shell Quantum Dots: Synthesis and Characterization of a Size Series of Highly Luminescent Nanocrystallites," *J. Phys. Chem. B*, vol. 101, pp. 9463, 1997.
[36] B. Krummheuer, V. M. Axt, and T. Kuhn, "Theory of pure dephasing and the resulting absorption line shape in semiconductor quantum dots," *Phys. Rev. B*, vol. 65, pp. 195313, 2002.
[37] G. D. Mahan, *Many-Particle Physics*, 3rd ed. New York: Kluwer Academic/Plenum Publishers, 2000.
[38] S. V. Goupalov, R. A. Suris, P. Lavallard, and D. S. Citrin, "Homogeneous broadening of the zero-optical-phonon spectral line in semiconductor quantum dots," *Nanotechnology*, vol. 12, pp. 518, 2001.
[39] R. A. Stradling and R. A. Wood, "The temperature dependence of the band-edge effective masses of InSb, InAs and GaAs as deduced from magnetophonon magnetoresistance measurements," *J. Phys. C*, vol. 3, pp. L94, 1970.
[40] H. Preier, "Recent advances in lead-chalcogenide diode laser," *Appl. Phys.*, vol. 20, pp. 189, 1979.
[41] B. L. Wehrenberg, C. Wang, and P. Guyot-Sionnest, "Interband and Intraband Optical Studies of PbSe Colloidal Quantum Dots," *J. Phys. Chem. B*, vol. 106, pp. 10634, 2002.
[42] O. Labeau, P. Tamarat, and B. Lounis, "Temperature Dependence of the Luminescence Lifetime of Single CdSe/ZnS Quantum Dots," *Phys. Rev. Lett.*, vol. 90, pp. 257404, 2003.
[43] S. A. Crooker, T. Barrick, J. A. Hollingsworth, and V. I. Klimov, "Multiple temperature regimes of radiative decay in CdSe nanocrystal quantum dots: intrinsic limits to the dark-exciton lifetime," *App. Phys. Lett.*, vol. 82, pp. 2793, 2003.
[44] C. d. M. Donegá, M. Bode, and A. Meijerink, "Size- and temperature-dependence of exciton lifetimes in CdSe quantum dots," *Phys Rev B*, vol. 74, pp. 085320, 2006.
[45] P. Palinginis, H. Wang, S. V. Goupalov, D. S. Citrin, M. Dobrowolska, and J. K. Furdyna, "Exciton dephasing in self-assembled CdSe quantum dots," *Phys. Rev. B*, vol. 70, pp. 073302, 2004.
[46] L. Besombes, K. Kheng, L. Marsal, and H. Mariette, "Acoustic phonon broadening mechanism in single quantum dot emission," *Phys. Rev. B*, vol. 63, pp. 155307, 2001.
[47] M. Kuno, J. K. Lee, B. O. Dabbousi, F. V. Mikulec, and M. G. Bawendi, "The band edge luminescence of surface modified CdSe nanocrystallites: Probing the luminescing state," *J. Chem.*

Phys., vol. 106, pp. 9869, 1997.

[48] W. W. Yu, L. Qu, W. Guo, and X. Peng, "Experimental Determination of the Extinction Coefficient of CdTe, CdSe, and CdS Nanocrystals," *Chem. Mater.*, vol. 15, pp. 2854, 2003.

[49] R. Rodriguez-Suarez, E. Menendez-Proupin, C. Trallero-Giner, and M. Cardona, "Multiphonon resonant Raman scattering in nanocrystals," *Phys. Rev. B*, vol. 62, pp. 11006, 2000.

[50] S. Schmidt-Rink, D. A. B. Miller, and D. S. Chemla, "Theory of the linear and nonlinear optical properties of semiconductor microcrystallites," *Phys. Rev. B*, vol. 35, pp. 8113, 1987.

[51] X. Fan, T. Takagahara, J. E. Cunningham, and H. Wang, "PURE DEPHASING INDUCED BY EXCITON–PHONON INTERACTIONS IN NARROW GaAs QUANTUM WELLS," *Solid State Commun.*, vol. 108, pp. 857, 1998.

[52] M. I. Vasilevskiy, E. V. Anda, and S. S. Makler, "Electron-phonon interaction effects in semiconductor quantum dots: A nonperturbative approach," *Phys. Rev. B*, vol. 70, pp. 035318, 2004.

[53] S. Rudin, T. L. Reinecke, and B. Segall, "Temperature-dependent exciton linewidths in semiconductors," *Phys. Rev. B*, vol. 42, pp. 11218, 1990.

[54] J. Voigt, F. Spiegelberg, and M. Senoner, "Band Parameters of CdS and CdSe Single Crystals Determined from Optical Exciton Spectra," *Phys. Stat. Sol. B*, vol. 91, pp. 189, 1979.

[55] S. Logothetidis, M. Cardona, P. Lautenschlager, and M. Garriga, "Temperature Dependence of the dielectric function and the interband critical points of CdSe," *Phys. Rev. B*, vol. 34, pp. 2458, 1986.

[56] F. Gindele, K. Hild, W. Langbein, and U. Woggon, "Temperature-dependent line widths of single excitons and biexcitons," *J. Lumin.*, vol. 87-89, pp. 381, 2000.

[57] H. Zhao, S. Wachter, and H. Kalt, "Effect of quantum confinement on exciton-phonon interactions," *Phys. Rev. B*, vol. 66, pp. 085337, 2002.

[58] D. Valerini, A. Cretí, M. Lomascolo, L. Manna, R. Cingolani, and M. Anni, "Temperature dependence of the photoluminescence properties of colloidal CdSe/ZnS core/shell quantum dots embedded in a polystyrene matrix," *Phys. Rev. B*, vol. 71, pp. 235409, 2005.

[59] S. A. Empedocles and M. G. Bawendi, "Influence of Spectral Diffusion on the Line Shapes of Single CdSe Nanocrystallite Quantum Dots," *J. Phys. Chem. B*, vol. 103, pp. 1826, 1999.

[60] M. Shim and P. Guyot-Sionnest, "Permanent dipole moment and charges in colloidal semiconductor quantum dots," *J. Chem. Phys.*, vol. 111, pp. 6955, 1999.

[61] S. A. Empedocles and M. G. Bawendi, "Quantum-Confined Stark Effect in Single CdSe Nanocrystallite Quantum Dots," *Science*, vol. 278, pp. 2114, 1997.

[62] J. Muller, J. M. Lupton, A. L. Rogach, J. Feldmann, D. V. Talapin, and H. Weller, "Monitoring Surface Charge Movement in Single Elongated Semiconductor Nanocrystals," *Phys. Rev. Lett.*, vol. 93, pp. 167402, 2004.

[63] I. Bentwich, A. Avniel, Y. Karov, R. Aharonov, S. Gilad, O. Barad, A. Barzilai, P. Einat, U. Einav, E. Meiri, E. Sharon, Y. Spector, and Z. Bentwich, "Identification of hundreds of conserved and nonconserved human microRNAs," *Nature Genetics*, vol. 37, pp. 766, 2005.

[64] G. Battail, "Should Genetics Get an Information-Theoretic Education?" *IEEE ENGINEERING IN MEDICINE AND BIOLOGY MAGAZINE*, vol. 25, pp. 34, 2006.

[65] M. K. Gupta, "The Quest for Error Correction in Biology," *IEEE ENGINEERING IN MEDICINE AND BIOLOGY MAGAZINE*, vol. 25, pp. 46, 2006.

[66] T. D. Schneider, "Claude Shannon: Biologist," *IEEE ENGINEERING IN MEDICINE AND BIOLOGY MAGAZINE*, vol. 25, pp. 30, 2006.

[67] B. DasGupta, K. M. Konwar, I. I. Mndoiu, and A. A. Shvartsman, "DNA-BAR: distinguisher selection for DNA barcoding," *Bioinformatics*, vol. 21, pp. 3424, 2005.

[68] Y.-C. Cao, T.-C. Liu, X.-F. Hua, X.-X. Zhu, H.-Q. Wang, Z.-L. Huang, Y.-D. Zhao, M.-X. Liu, and Q.-M. Luo, "Quantum dot optical encoded polystyrene beads for DNA detection," *Journal of Biomedical Optics*, vol. 11, pp. 054025, 2006.

[69] K. L. Kellar and M. A. Iannone, "Multiplexed microsphere-based flow cytometric assays," *Exp. Hematol.*, vol. 30, pp. 1227, 2002.

[70] H. Xu, M. Y. Sha, E. Y. Wong, J. Uphoff, Y. Xu, J. A. Treadway, A. Truong, E. O'Brien, S. Asquith, M. Stubbins, N. K. Spurr, E. H. Lai, and W. Mahoney, "Multiplexed SNP genotyping using the QbeadTM system: a quantum dot-encoded microsphere-based assay," *Nucleic Acids Research*, vol. 31, pp. e43, 2003.

[71] J. P. Nolan and F. Mandy, "Multiplexed and microparticle-based analyses: Quantitative tools for the large-scale analysis of biological systems," *Cytometry Part A*, vol. 69A, pp. 318, 2006.
[72] www.luminex.com
[73] J. P. Nolan and L. A. Sklar, "Suspension array technology: evolution of the flat-array paradigm," *Trends in Biotechnology*, vol. 20, pp. 9, 2002.
[74] X. Gao and S. Nie, "Quantum Dot-Encoded Mesoporous Beads with High Brightness and Uniformity: Rapid Readout Using Flow Cytometry," *Anal. Chem.*, vol. 76, pp. 2406, 2004.
[75] X. Gao and S. Nie, "Doping Mesophorous Materials with Multicolor Quantum Dots," *J. Phys. Chem. B*, vol. 107, pp. 11575, 2003.
[76] O. Madelung, "Semiconductors - Basic Data," 2nd revised ed. New York: Springer, 1996.
[77] X. Zhou, J. He, L. Liao, M. Lu, X. Ding, X. Hou, X. Zhang, X. He, and S. Lee, "Real-Time Observation of Temperature Rise and Thermal Breakdown Processes in Organic LEDs Using an IR Imaging and Analysis System," *Adv. Mater.*, vol. 12, pp. 265, 2000.
[78] H. Htoon, P. J. Cox, and V. I. Klimov, "Structure of Excited-State Transitions of Individual Semiconductor Nanocrystals Probed by Photoluminescence Excitation Spectroscopy," *Phys. Rev. Lett.*, vol. 93, pp. 187402, 2004.
[79] A. V. Baranov, Y. P. Rakovich, J. F. Donegan, T. S. Perova, R. A. Moore, D. V. Talapin, A. L. Rogach, Y. Masumoto, and I. Nabiev, "Effect of ZnS shell thickness on the phonon spectra in CdSe quantum dots," *Phys. Rev. B*, vol. 68, pp. 165306, 2003.
[80] F. Reif, *Fundamentals of Statistical and Thermal Physics*. New York: McGraw-Hill, 1965.
[81] T. C. P. Chui, D. R. Swanson, M. J. Adriaans, J. A. Nissen, and J. A. Lipa, "Temperature Fluctuations in the Canonical Ensemble," *Phys. Rev. Lett.*, vol. 69, pp. 3005, 1992.
[82] R. Bhargava, "Properties of wide bandgap II-VI semiconductors." London: Institute of Electrical Engineers, 1997.